

‘IMPLICATIONS OF A NEWLY DISCOVERED ACTIVE FAULT IN THE BASIN OF MEXICO’

*A thesis submitted in partial fulfilment of the requirements of Liverpool John Moores
University for the degree of Master of Philosophy*

*This research programme was carried out in collaboration with the Centro Nacional de
Prevención de Desastres (CENAPRED), Mexico City, Mexico.*

KURT SIMPSON

May 2021

Acknowledgements

I would firstly like to thank the Centro Nacional de Prevención de Desastres (CENAPRED) for integrating me into their team, providing access to their seismological database and for the opportunity to create new friendships. A special mention is to be made to the seismology department, namely Alberto Galaviz for his supervision in Mexico, generous hospitality, repeated assistance in the field and guidance with GMT software. I would like to extend my gratitude to Professor Silvia Gonzalez for the opportunity to work with CENAPRED, the unparalleled support during the COVID-19 pandemic and for the comments that have helped improve this study. Thanks are also to be shared with Jon Dick for his encouragement, support, and useful comments. Finally, I would like thank Liverpool John Moores University for the postgraduate Global Scholar Award which helped in financing the international research.

Abstract

Seismic-source detection of local earthquakes inside the Basin of Mexico has recently become more precise and the inferred faults and fractures from which the seismic events originate are well documented. Mooser (2018) provided a new theory on faulting which revisits the evolution of the Basin as a high-altitude volcano-tectonic depression. Using stereographic modelling, a series of shallow inferred faults have been identified, which strike along the elliptical orientation of the basement high-altitude volcanic axis. Following Mooser's (2018) 2D stereographic model illustrating the eastern region of the Trans-Mexican Volcanic Belt (TMVB), this study attempts to quantify the existence of a shallow crustal fault, a new type of fault with formation processes attributed to the unique geological conditions in the Basin of Mexico and evaluate the effects of a projected fault displacement on the population and infrastructure of the neighbouring municipalities. Probabilistic and deterministic methodologies were used to complete a geophysical survey in the western region of the basement, and calculate the fault schematics, while visual observations of structural damage in Mexico City from the M_w 7.1 19/09/2017 Puebla/Morelos earthquake were used as a proxy for understanding the building performance and demographic risk of a fault displacement within the Basin of Mexico.

The results of this study substantiate the possible existence of an active 23.5km shallow crustal fault in an area of critical stress between Xitle volcano and Iztacalco in the Basin of Mexico. It is likely that Structurally Controlled Differential Subsidence (SCDS) associated with the rapid 20th century increase in anthropogenic activity in Mexico City, and strong-ground motion from major national earthquakes, has accelerated a subsurface fracture formation sequence by exceeding the basement's maximum stress capacity. The projected maximum M_s 6.7 output from a full-length rupture of the shallow crustal fault originating from within the Basin, forecasts a potential scenario that is likely to have more severe socio-economic implications to those experienced during the 2017 M_w 7.1 Puebla-Morelos earthquake, with insufficient ground-motion warning time from the Seismic Alert System for the population in Mexico City and its neighbouring municipalities.

Table of Contents

Acknowledgements.....	1
Abstract.....	2
List of Abbreviations	5
1 Introduction.....	6
1.1 Mexico Tectonic Setting.....	6
1.2 Geology of the Basin of Mexico	8
1.3 Seismic Setting.....	10
1.4 Related Studies.....	14
1.5 Purpose of the Study	15
2 Data Sources	18
2.1 Networks and Records in Mexico.....	18
2.1.1 Republic of Mexico.....	18
2.1.2 Basin of Mexico.....	19
3 Methodology.....	22
3.1 Seismic Sources	22
3.2 Fault Digitation	22
3.3 Numerical Analysis.....	23
3.3.1 Shallow Crustal Fault Schematics.....	23
3.3.2 Fault Displacement	27
3.3.3 Amplification Factor	28
3.4 Visual Observations	29
3.5 Demographic Analysis.....	31
4 Results.....	32
4.1 Fault Schematics	32
4.2 Fault Displacement	37
4.3 1D Amplification Factor Model.....	38
4.4 Visual Observations of structural damage	42
4.5 Demographic Analysis.....	60
5 Discussion.....	69
5.1 Quantification of the shallow crustal fault.....	69
5.2 Implications from a projected displacement	72
5.3 Limitations and future actions.....	74
6 Conclusions.....	76

7	References.....	77
7.1	Appendix.....	85
7.1.1	Introduction.....	85
7.1.2	Data.....	91
7.1.3	Methodology.....	92
7.1.4	Results.....	93

List of Abbreviations

CEM	Continuous Elevation Model
CENAPRED	The National Centre for Disaster Prevention
CFE	Federal Electricity Commission
CIRES	The Centre of Instrumental and Seismic Records
CMT	Centroid Moment Tensor
DEM	Digital Elevation Model
DSHA	Deterministic Seismic Hazard Analysis
GMT	Generic Mapping Tools
INEGI	National Institute for Geography and Statistics
IRIS	Incorporated Research Institutions for Seismology
MARS	Mapping the Rivera Subduction Zone
MASE	Meso-America Subduction Experiment
MAT	Meso-America Trench
MCE	Maximum Credible Earthquake
MMS	Modified Mercalli Scale
MNAR	Mexican National Atlas of Risk
MOC	Manual of Civil Structures
NOAA	National Oceanic and Atmospheric Administration
NGS	National Geodetic Survey
SASMEX	Seismic Alert System Mexico
SC	Shallow Crustal
SCDS	Structurally Controlled Differential Subsidence
SSN	National Seismological Service
TMVB	Trans Mexican Volcanic Belt
USGS	U.S. Geological Survey
VEOX	Veracruz-Oaxaca seismic line

1 Introduction

This study was completed in a collaboration between Liverpool John Moores University and the Centro Nacional de Prevención de Desastres (CENAPRED) Mexico. Created in 1988 in response to the 1985 M8.1 Michoacán earthquake, CENAPRED acts as a technical body with the aim of mitigating the socio-economic effects of natural disasters in Mexico. Research took place during a three-month internship at CENAPRED under the supervision of Geophysicist Alberto Galaviz.

1.1 Mexico Tectonic Setting

The interaction of tectonic plates in Mexico is extensively researched due to its associated active volcanism and frequent strong motion seismic events (Pérez-Campos *et al*, 2008). The Meso-America Subduction Zone (MAT) comprises a submarine trench which runs parallel to the western coast of Mexico and the Gulf of California, formed through the subduction of the northern edge of the oceanic Cocos plate and Rivera microplate, beneath the southern edge of the continental North American plate (Ferrari *et al*, 2012). The Trans-Mexican Volcanic Belt (TMVB) is a 160,000km² Neogene volcanic arc, extending 1000km west from the Pacific coast to the Gulf of Mexico, oblique to the MAT (Figure 1) (García-Palomo *et al*, 2018). Predominantly composed of andesites and dacites, the continental arc is characterised by a convergence of morphological segments (Western-Central-Eastern), originating from magmatic assimilation of the lower crust at the fracture zones in the early Oligocene (30Ma) (Garcia-Palomo *et al*, 2002). The western segment is distinguished by alkaline and calc-alkaline volcanic deposits from the Colima-Chapala-Tepic volcanic trio. N-S trending andesitic-dacitic stratovolcanoes and calc-alkaline monogenetic fields (e.g. Chichinautzin volcanic field) dominate the central Trans-Mexican Volcanic Belt, with Eastern morphology defined by dispersed calc-alkaline products of andesitic-dacitic stratovolcanoes (Mooser *et al*. 1974).

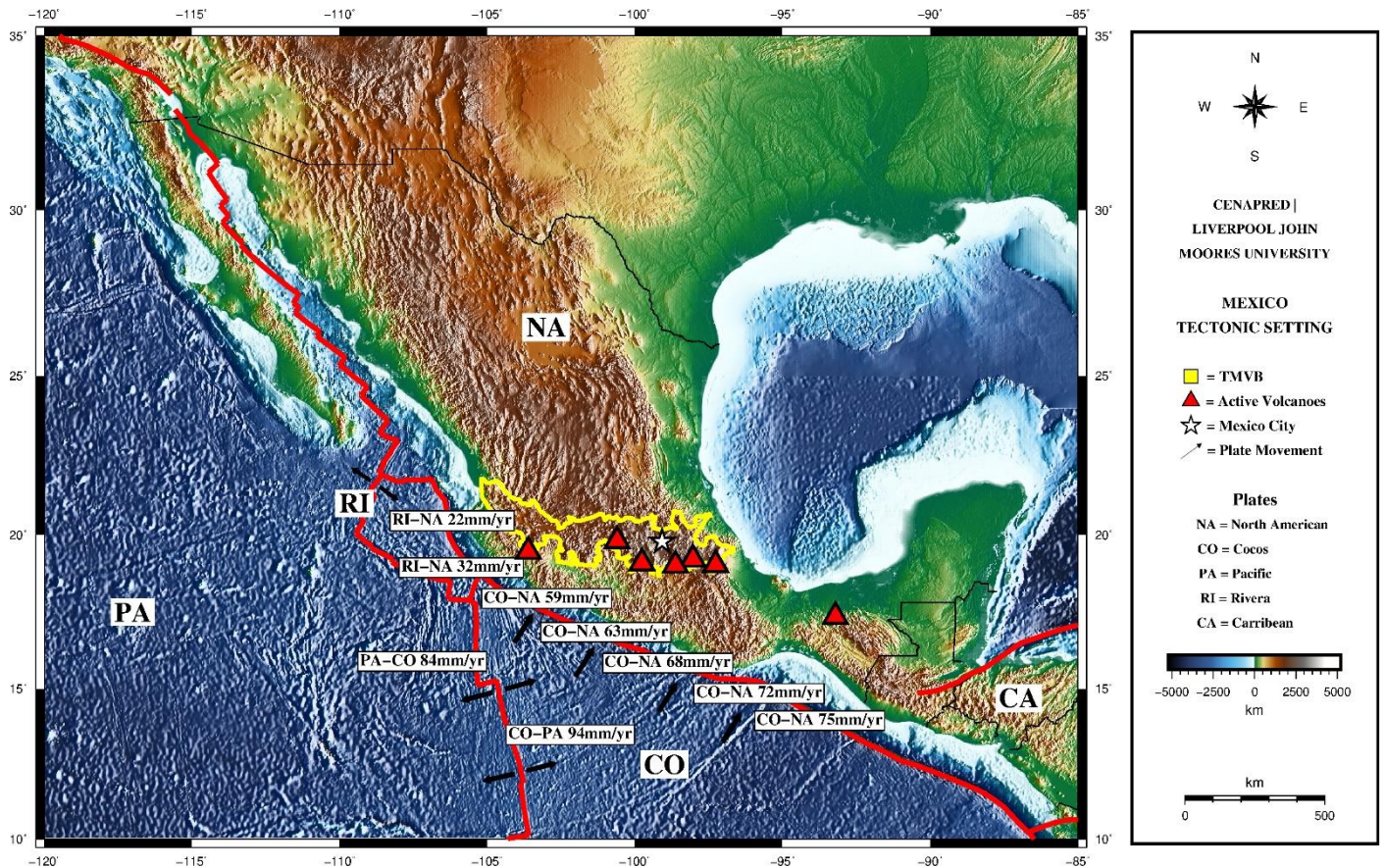


Figure 1. Regional tectonic setting for Mexico, showing the active subduction at the Middle-America Trench of the Cocos and Rivera plates beneath the North American plate. The red triangles indicate the position of active volcanoes; plate boundaries are highlighted by the red lines; the Trans-Mexican volcanic belt is delineated in yellow, and the white star locates Mexico City in the Basin of Mexico. Plate movement in mm per year, is highlighted accordingly with direction indicated by the black arrows. Created using GMT 5.3 for Linux.

1.2 Geology of the Basin of Mexico

The Basin of Mexico is a high-altitude endorheic, volcano-tectonic depression located at the Central - Eastern intersection of the TMVB (Figure 1) (García-Palomo *et al.*, 2018). It orientates NE-SW, measuring 90km in length and 80 km wide, restricting to 50km further south (De Cserna, 1987). Encompassing an area of 9,600km² with an average elevation of 2,240m (above sea level), it is limited by andesitic and dacitic volcanic ranges: The Apan-Tezontepec volcanic field to the North, the N-S aligned Sierra Nevada to the East (comprised of Popocatepetl, Iztaccíhuatl, Telapón, and Tláloc stratovolcanoes), the Chichinautzin Monogenetic Field aligning E-W to the South and the NW-SE aligned Sierra de las Cruces to the West (Arce *et al.*, 2019).

Geotechnical studies which integrate stratigraphic soil classification with isotopic and radiocarbon dating (Pérez-Cruz, 1988; Siebe *et al.*, 2004; Arce *et al.*, 2013) indicate that the formation of the volcano-tectonic depression originated from the displacement of a Cretaceous limestone basement by the NNE Cañón de Lobos trending reverse fault (Fitz-Diaz *et al.*, 2011). The basin then evolved through sequences of complex tectonic activity and volcanism (Arce *et al.*, 2019). Successions of volcanoclastic sediments during the Oligocene (30.0±0.05 – 23.5±0.05 Ma) - Miocene (22.8-5.0±0.1 Ma), which overlaid the limestones (Pérez-Cruz, 1988), were uplifted by the (NW-SE) Mixhuca normal fault, producing several NW-SE horst and grabens (Garcia-Palomo *et al.*, 2008). The emplacement of the Sierra de las Cruces and the Apan-Tezontepec volcanic field is associated with a third tectonic event relating to the (NW-SE) Tenochtitlan fault system (Arce *et al.*, 2013), with the construction of the Chichinautzin monogenetic field affiliated with the latter E-W trending normal fault system during the Plio-Pleistocene (5-0.4 Ma). This morphology blocked drainage in the south, forming the Texcoco and Chalco lakes, represented by a stratigraphy of paleosols, volcanic ashes and lacustrine sediments (Mooser, 1963). According to geotechnical wells drilled in the Basin (González-Torres *et al.*, 2005) the interbedded soils vary in thickness from 70m to 300m in the lake zones (Lozano-Garcia *et al.*, 2017; Siebe *et al.*, 2004; Garcia-Palomo *et al.*, 2000) (Figure 2).

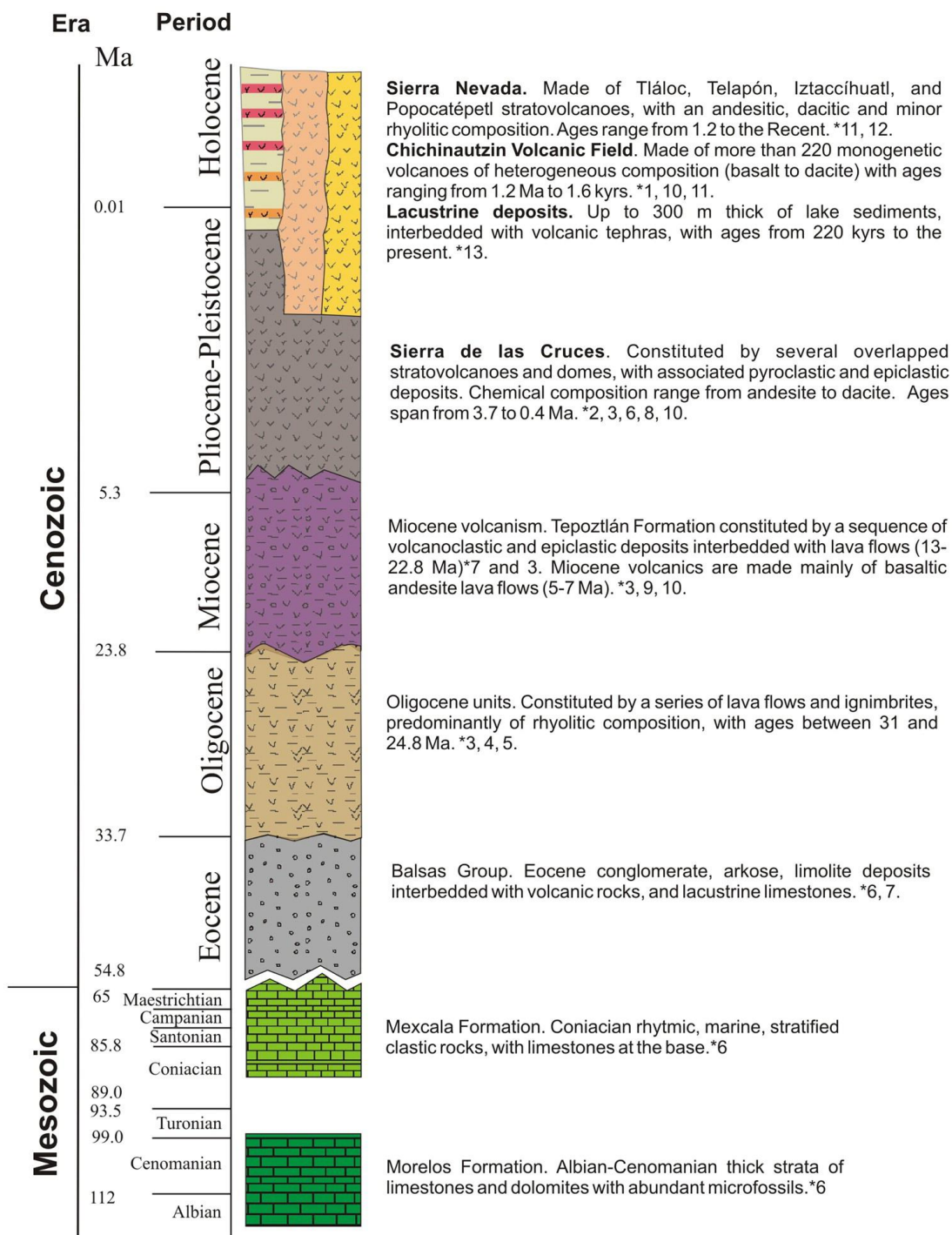


Figure 2. General stratigraphic column of the Basin of Mexico and the adjacent volcanic ranges (After Arce *et al*, 2019)

The basin divides between the States of Mexico, Hidalgo and the 16 municipalities of the Mexico City metropolitan area, populated by >20 million people (INEGI, 2010). Systematic deforestation and the erosion of soft water-saturated clays, associated with widespread urbanisation in the lake zone, has increased the city's susceptibility to seismic related hazards (Santoyo et al., 2005). Modelling the geometry of the basin and the seismic – soil response during strong ground motion can identify the predominant periods of vibration of the soil necessary for categorising structural design codes (Singh *et al.* 1988; Galvis *et al.*, 2017).

1.3 Seismic Setting

The Central-Eastern location of the Basin place it inside Zone C of the macro-seismic zonation of the Republic of Mexico in accordance with The Manual of Civil Structures (MOC) 2008 (Tena-Colunga *et al.*, 2009) (Figure 3), experiencing peak ground accelerations $\leq 687\text{cm/s}^2$. This means that the Basin of Mexico is susceptible to several types of seismic sources (figure 4), which can be categorized into four groups (Rosenblueth *et al.*, 1987):

Interplate or subduction zone earthquakes occur due to friction between the North American plate and Cocos plate. These earthquakes concentrate at depths $\geq 5\text{km}$ - $\leq 35\text{km}$ along the margin between the Meso-America Trench (MAT) and the Pacific coast of Mexico (Rosenblueth et al, 1987). On the 19th of September 1985, a M8.1 (Maximum Intensity – Modified Mercalli Scale) interplate earthquake ruptured a segment ($\approx 100\text{-}200\text{km}$) of subduction zone between Colima and Guerrero, known as the Michoacán Seismic Gap (Singh *et al.*, 1980). Seismic waves propagated through the Mexican Basin, 400km from the epicentre, leaving unprecedented structural damage and killing over 10,000 people (Sánchez-Sesma *et al.*, 1988). This strong motion event, which remains Mexico's worst natural disaster to date, led to the establishment of Mexico City's Seismic Alert System (SAS) in 1991, providing early warning of strong motion from interplate earthquakes (Suárez *et al.*, 2009).

Inslab earthquakes occur on the subducting Cocos plate. Hypocentre distribution is defined by the complex plate limits concentrating ≥ 40 km depth (Pérez-Campos *et al*, 2008). The depth is dependent on the subducting angle of the Cocos plate, which varies in relation to crust thickness at the region of subduction, ascertained by the Meso-America Subduction Experiment (MASE) (2006). On the 19th of September 2017, a $M_w 7.1$ normal faulting inslab earthquake struck the state intersection between Puebla and Morelos, 120km SSE of Mexico City. The Centre of Instrumental and Seismic Records (CIRES) indicated that the early warning SAS alerted citizens 19s before the S-wave reached the Mexican Basin, however the accuracy is disputed as local reports suggest the SAS was ineffective, with the alert signal sounding as ground motion commenced. The shaking lasted 30 seconds, damaging 5500 buildings with ≈ 400 casualties in Mexico City (Alberto *et al*, 2018).

Intraplate or Cortical earthquakes occur on the North American plate. The lithospheric thickness of the continental plate concentrates hypocentres to depths ≤ 50 km (Ferrari *et al*, 2012). Intraplate earthquakes therefore have a greater probability of striking nearer to the surface (Kostoglodov, 1999). Following the first implementation of instrumental seismic recording in Mexico in 1910 (García Acosta and Suárez Reynoso, 1996), a $M 6.9$ (MMS) (Rodríguez-Pascua *et al*, 2017) reverse fault earthquake struck Acambay on the 19th of November 1912. Paleo-seismic analysis by Langridge (2000) place the hypocentre in the western segment of the E-W trending Morelia-Acambay Fault System at ≈ 15 km deep, 120km NNW of Mexico City. The socio-economic repercussions in Mexico City were poorly documented, however Urbina (1913) compared the ground motion and associated damage to the destructive $M 7.9$ (MMS) 1906 San Francisco earthquake.

The scope of this study is on the fourth seismic source, local earthquakes within the Basin. These seismic events are typically $\leq M_w 5.0$ and shallow, ≤ 20 km deep, associated with active fault systems present inside or encircling the Basin of Mexico (Rosenblueth *et al*, 1987; Arce *et al*, 2019). Since the introduction of digital recording equipment by the National Seismological Service to the Mexico Valley Seismic Network in 2007, seismometers record seismic waves in a wider frequency band, increasing the sensitivity to local earthquake detection (SSN, 2021).

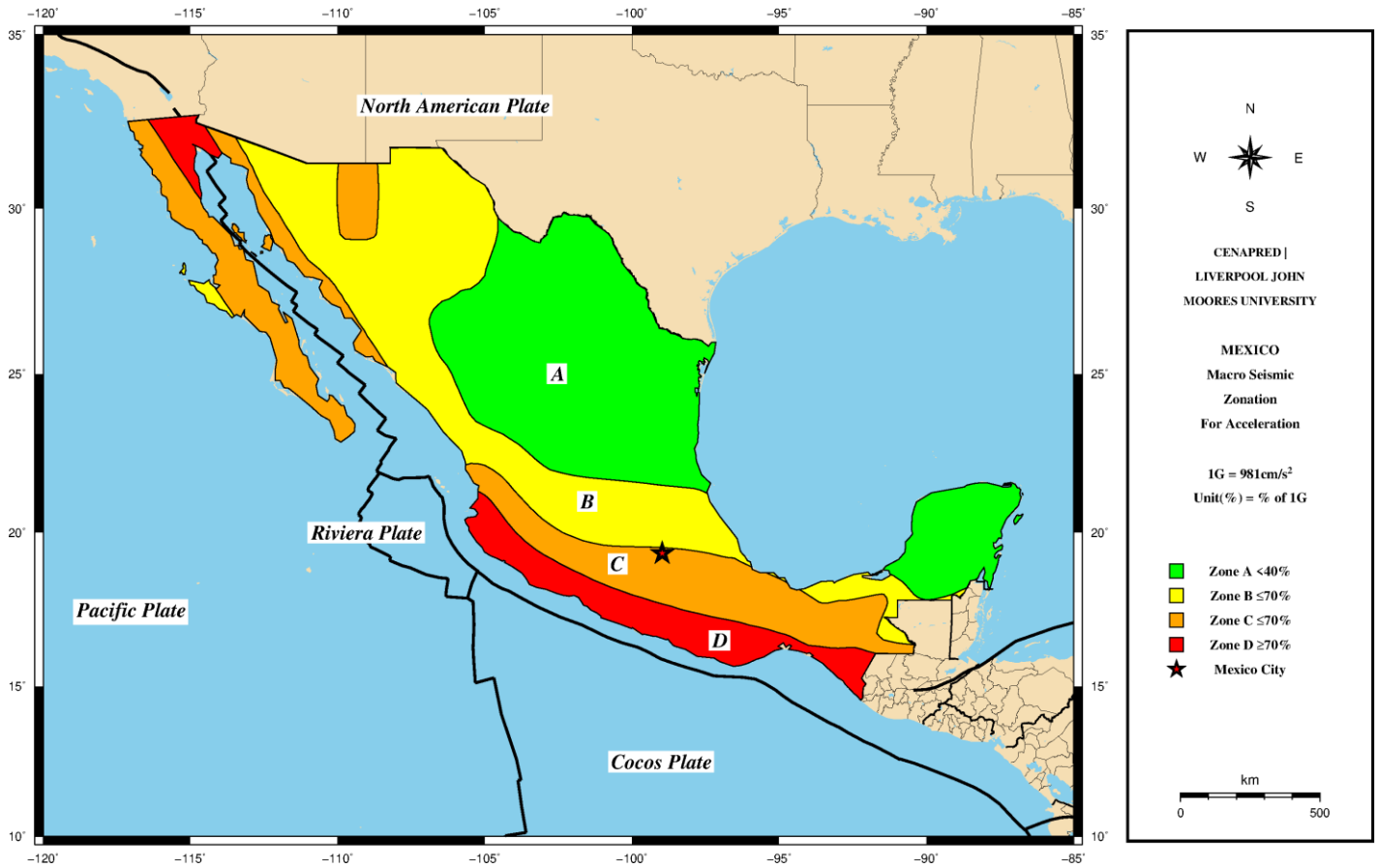


Figure 3. Macro-zonation for seismic risk in Mexico based on peak ground acceleration (cm/s^2). Acceleration is represented as a % of Gravity ($1G=981\text{cm/s}^2$). Data digitised from the Mexican National Atlas of Risk (MNAR) and the Manual of Civil Structures (MOC) 2008 (Tena-Colunga *et al*, 2009). Created using GMT 5.3 for Linux.

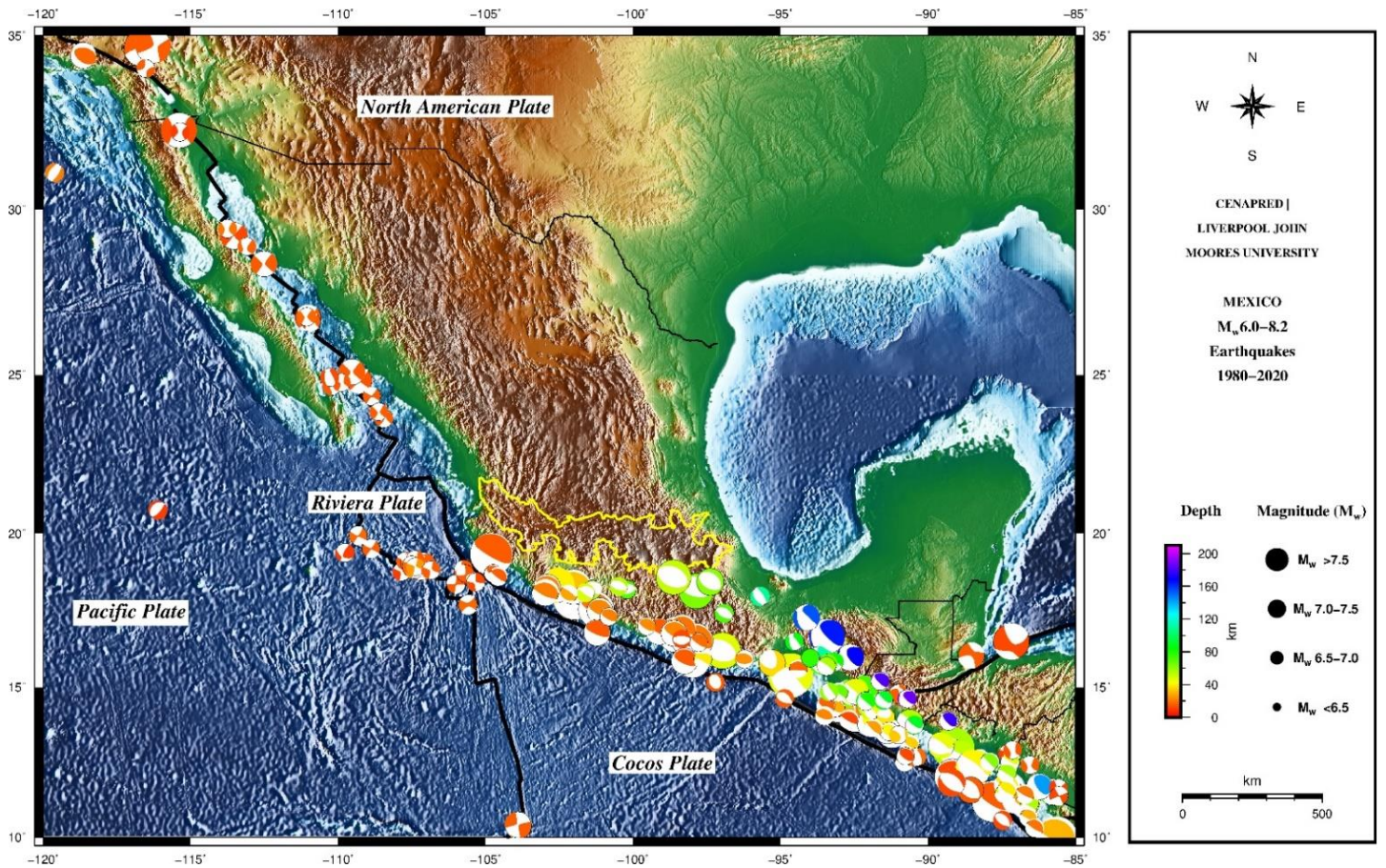


Figure 4. Distribution of Focal Mechanisms from seismic events M_w 6.0-8.2 between 1980-2020 in Mexico. The 'Beach Ball' displays the type of earthquake using the; (1) Strike, (2) Dip and (3) Rake, from the seismic event. 'Beach ball' size refers to the Moment Magnitude (M_w), with the colour representing the hypocentre depth. Data from the Global CMT Project (See appendix Table 13). Created using GMT 5.3 for Linux.

1.4 Related Studies

The seismic response from the complex soil stratigraphy and geometry in the Basin of Mexico to external seismic sources is a recognised phenomenon and an ongoing paradigmatic investigation. Early studies by Faccioli (1976), Singh *et al* (1988) and later, Shapiro *et al* (1997) evaluated seismic amplification between the different geotechnical properties from the bedrock hills and lakebed zones in the Basin. Evidence suggested that a maximum relative amplification of 500 times is possible at certain sites in the lakebed zone, which precedes any known amplification worldwide. Recent high-performance modelling by Cruz-Atienza (2016) addresses the long-standing inability to successfully model the deeper basin structures (largely due to the former absence of adequate technology). The study simulated the propagation regime of ground motion in the Basin following from the research of Sánchez-Sesma *et al* (1988), Singh (1993) and Chávez-García (2002), concluding that the topographic irregularity of the deep basin structure is the fundamental variable responsible for the extreme amplification of seismic waves in the lake-bed zone.

Seismic-source detection of local earthquakes inside the Basin has recently become more precise and the inferred faults and fractures from which the seismic events originate are well documented. Studies conducted to date have focused on fault systems evolved from the formation of the Mexican Basin. The most comprehensive study is by Arce *et al* (2019). Findings from previous publications on the geology of the Basin (1978 to 2018) were compiled with new deep well data from the Mexico City Water System (SACMEX), recognising four main tectonic fault systems (previously mentioned); The NNE orientated Cañón de Lobos thrust fault; the NW-SE Mixhuca normal fault, which formed the 1500m 'Fossa Roma' volcanic depression; NE-SW trending dextral and normal faults; and a series of young E-W orientated normal faults, namely Tenango, Xochimilco and the Santa Catarina Graben (See appendix Figure 26). Lately, low magnitude (1.1-4.0 M_c) seismic swarms in the south of the Basin, a sign of magmatic movement, have been associated with the E-W lateral extension of the Xochimilco normal fault (Campos-Enríquez *et al*, 2015), previously recognised by Bravo *et al* (1988) to be one of the most active regions of seismology in the Basin.

The focus of these studies is necessary to fully substantiate the irregular geotechnical structure of the Valley of Mexico and its susceptibility to frequent strong ground motion. Using stereographic 2D modelling, a prevalent technique for displaying line geometry (Davis and Reynolds, 1996), Mooser (2018) provides a new theory on faulting in the Basin of Mexico, which revisits the evolution of the Basin as a high-altitude volcano-tectonic depression. The 2D model projects the tectonic setting and fault stratigraphy in the east of the Trans-Mexican Volcanic Belt between Nevado de Toluca and Malinche Volcano, identifying a series of shallow inferred faults, which strike along the elliptical orientation of the high-altitude volcanic axis (the basin structure). Mooser (2018) proposes that the fault system is the product of a sinking Basin, resulting from density contrasts between the volcanic ranges and the internal sedimentary basin structure, and an exponential increase in anthropogenic activity in the last 100 years. This theory is supported by both aeromagnetic (Figure 5) and deep Bouguer gravity anomaly (Figure 6) lows of -150 to -250 nanoTeslas (nT) and -100 to -250 mGals respectively, in the Valley of Mexico, which indicate the existence of a low-density structure beneath the lower crust, most likely an intrusive mantle layer (Urrutia-Fucugauchi, 1996). This may also be supported by the findings of Ovando-Shelley *et al* (2007) which imply that water extraction from the Basins deep aquifers, to be the main cause of ongoing regional subsidence, with future intensification anticipated considering the rate of urban expansion. Considering the potential atypical or partial non-tectonic origins of the proposed shallow inferred faults by Mooser (2018), this study uses the term ‘Shallow Crustal (SC) Fault’ to differentiate from traditional tectonic faults, with the intention of future adoption upon quantification.

1.5 Purpose of the Study

Given the current understanding of seismic-soil interaction and the associated socio-economic implications of past strong ground motion in Mexico City, Mooser’s (2018) theory proposing the existence of active faults with origins uncharacteristic of conventional tectonic formation processes in the Basin of Mexico, requires further research. This study aims to quantify a potential shallow crustal fault in the Basin of Mexico using Mooser’s (2018) 2D stereographic model and evaluate the effects of

a projected fault displacement on the population and infrastructure using probabilistic and deterministic methodology.

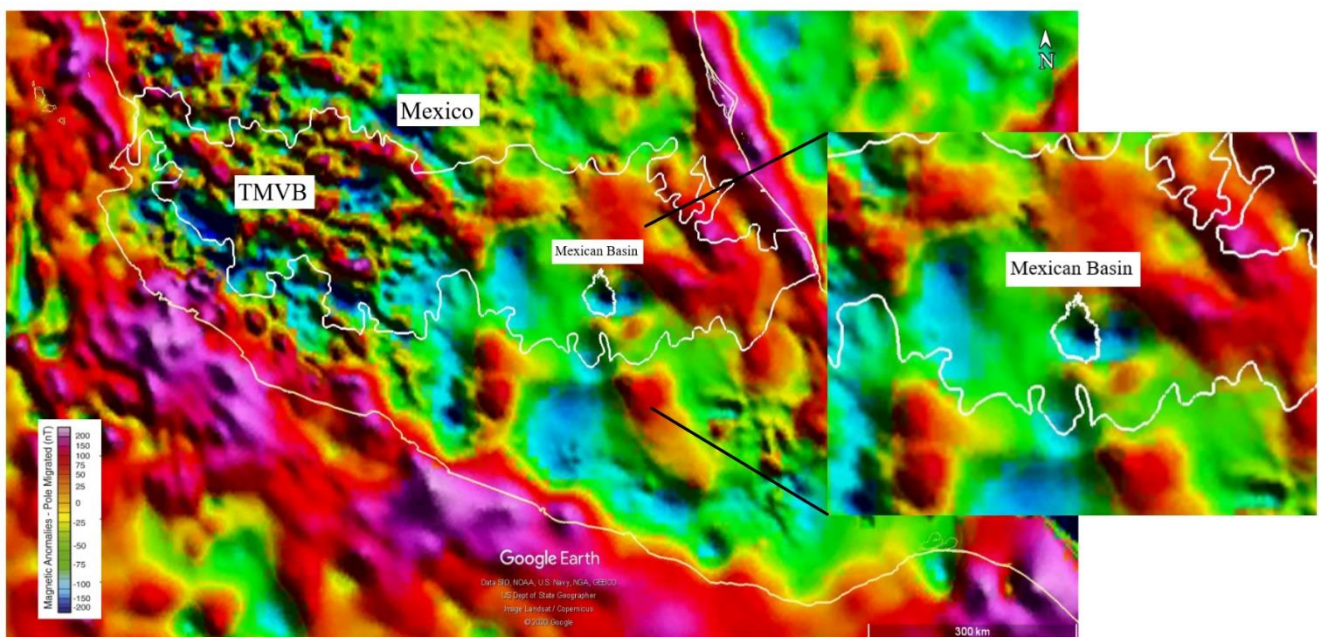


Figure 5. Earth Magnetic Anomaly Grid (2-arc-minute resolution) (EMAG2) for the Republic of Mexico. The Basin of Mexico experiences aeromagnetic anomalies in the range of -150 to -250 nanoTeslas (nT). Data from the National Oceanic and Atmospheric Administration (NOAA). Created using Google Earth Pro. (Maus, S. 2009: EMAG2: Earth Magnetic Anomaly Grid (2-arc-minute resolution). Version 2. NOAA National Centres for Environmental Information. <https://doi.org/10.7289/V5MW2F2P>).

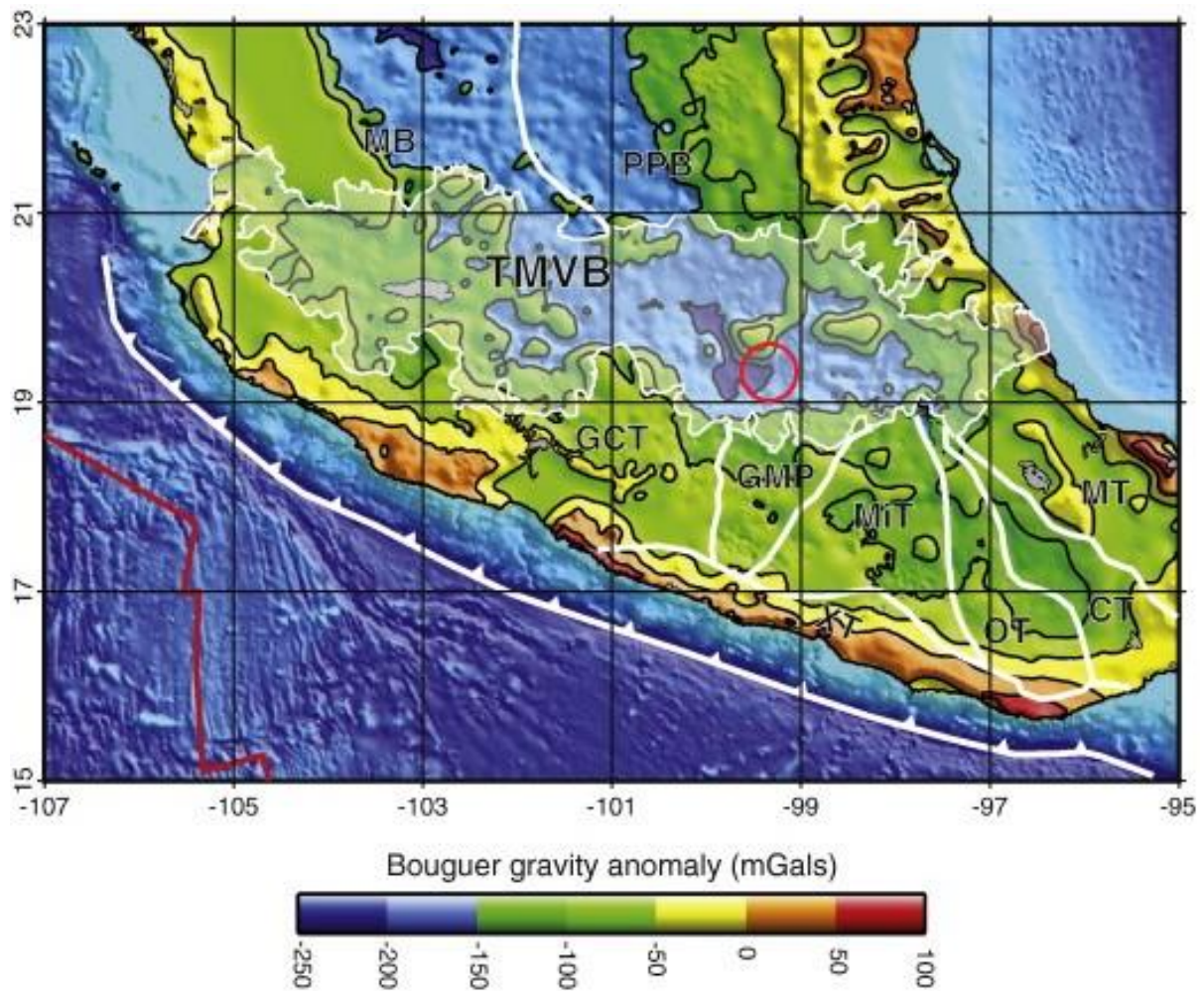


Figure 6. Bouguer Gravity anomaly map of central Mexico. The red circle indicates the Basin of Mexico. The Bouguer gravity anomaly in the Basin ranges from -100 to -250 mGals. Data from NOAA (Modified from Ferrari *et al*, 2012).

2 Data Sources

2.1 Networks and Records in Mexico

2.1.1 Republic of Mexico

The Global CMT project curates and maintains a catalogue of seismic moment tensors from the Incorporated Research Institutions for Seismology (IRIS) and U.S. Geological Survey (USGS) Global Seismographic Network of (~178) seismic stations (Ekström, 1997). In the scope of earthquake representation, the methodology of the CMT project accounts for the linear relationship between the independent components of a zeroth-order moment-tensor and the sequential generation of ground motion. The algorithm uses a strategy that filters events depending on the wave type and event magnitude. The systematic application of the algorithm and rapid dissemination of events $>M_w$ 6.0 make the Global CMT Project an important source for large magnitude earthquakes in Mexico (Ekström, 2012). This study uses seismic moment tensor records from the Global Centroid-Moment-Tensor (CMT) network for seismic events M_w 6.0-8.2 between 1980-2020 in the Republic of Mexico.

The Manual of Civil Structures (MOC) 2008 (Tena-Colunga *et al*, 2009) divides Mexico into four zones of seismic risk based on peak ground acceleration (cm/s^2), accounting for earthquake sources and the maximum credible earthquake (MCE) scenario for each region. This study uses the latest peak ground acceleration (cm/s^2) records for the Republic of Mexico, updated in 2015 by the Federal Electricity Commission (CFE) and National Seismological Service (SSN) based on recent seismic activity.

The Mexican Elevation Continuum (v3.0) at the Mexican National Institute for Geography and Statistics (INEGI) provides continuous representation of homogenous continental relief data for Mexico. This study uses a 60m resolution national Continuous Elevation Model (CEM) from INEGI with GMT (v5.3).

Gravity anomalies reveal variations in rock density, with the anomaly amplitude proportional to the bodies thickness and density contrast (Mooney, 2015). The National Oceanic and Atmospheric Administration (NOAA) records satellite altimeter-derived gravity anomalies (Sandwell, 1997) and terrestrial gravity measurements with the National Geodetic Survey (NGS). Geological features can also cause magnetic anomalies by enhancing or depressing the local magnetic field through variations in rock chemistry or magnetism (Blakely *et al*, 2005). NOAA compiles satellite, marine and airborne magnetic measurements to create global anomaly grids. The Earth Magnetic Anomaly Grid (2-arc minutes) uses precompiled data on local geology to interpolate anomalies into non-existent data regions like the Mexican Basin. This study uses Bouguer gravitational anomaly data, modified by Ferrari *et al* (2012) and EMAG2 magnetic anomaly records for the Republic of Mexico, from the NOAA database.

2.1.2 Basin of Mexico

The National Seismological Service (SSN) has a broadband network of 61 observatories, each with triaxial seismometers and accelerometers distributed throughout Mexico. The strategic placement of seismic stations in each city allows for the uniform determination of low magnitude $<M_w 5.0$ earthquakes without instrument saturation (SSN, 2021). There are 2 broadband network stations in the Basin of Mexico: The El Pozo (PZIG) station situated in the Institute of Geophysics at the Mexican National Autonomous University (UNAM), and the Popocatépetl (PPIG) station located on the North facing slopes of Popocatépetl Volcano. The Basin of Mexico has an additional seismological network composed of two smaller networks: the Mexico Valley Network, with 14 stations dispersed between the State of Mexico and Mexico City, and the Delegation Network, with 1 station in each of the cities' 16 municipalities. (Figure 7). This study has used seismic records from the SSN network between 1974-2020 for the Basin of Mexico.

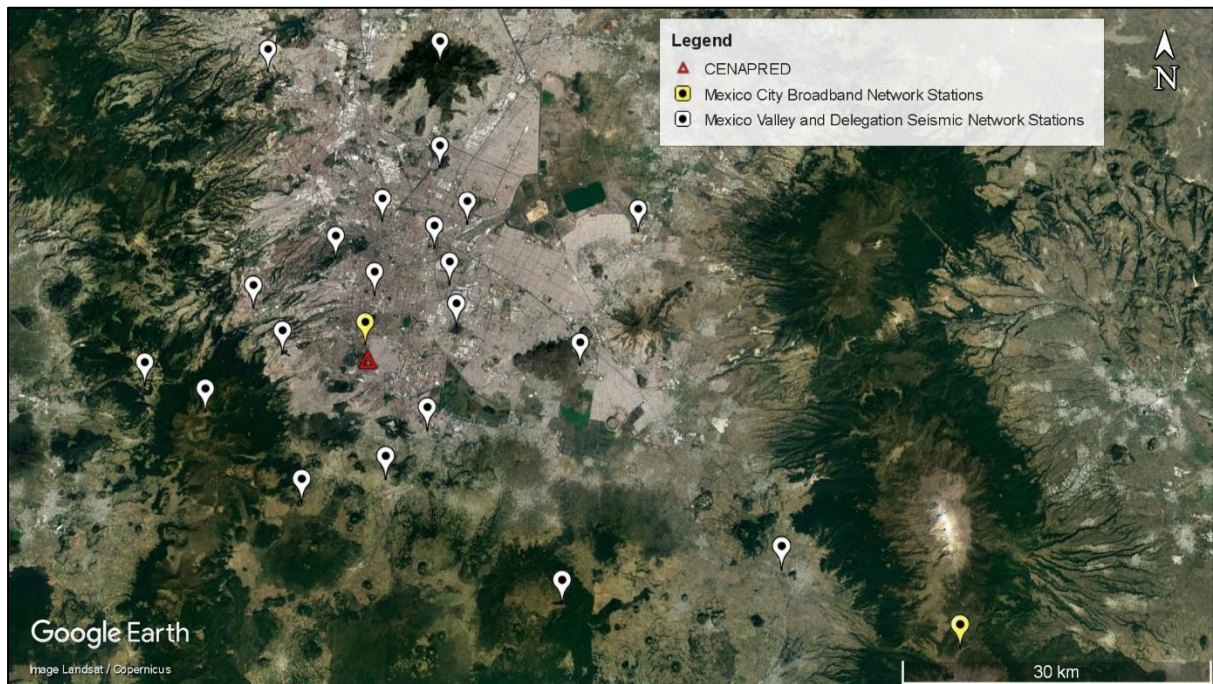


Figure 7. Seismic stations (27 of 32) from the National Seismological Service (SSN) Broadband, Mexico Valley and Delegation seismic networks in the Basin of Mexico. Five seismic stations in the State of Mexico from the Mexico Valley network are excluded from view (see appendix Table 14). CENAPRED is highlighted by the red triangle. Data from the SSN.

First proposed by Marsal and Mazari (1959), the Basin of Mexico can be divided into three zones of soil composition and thickness: (I) Rock – firm soils and rock sites, (II) Transition – uncemented sands and silts/compact alluvial deposits, and (III) Soft - interbedded lake sediments (mixed clays with lenses of sand and silt). The microzonation represents the local reception of seismic amplification in accordance with the basin geometry. The soil microzonation was updated by Tena-Colunga *et al* in 1999 and again in 2009 in the Manual of Civil Structures (MOC) (Tena-Colunga *et al*, 2009). The National Centre for Prevention of Disasters (CENAPRED) integrates data from the Mexican National Autonomous University (UNAM), the National Seismological Service (SSN), the Earth Observation Laboratory (LANOT) and the National Oceanic and Atmospheric Administration (NOAA) with the latest published sources like Tena-Colunga (2009), to create an interactive database called the Mexican National Atlas of Risk (MNAR). This study uses the latest (2015) soil micro-zonation data for the Basin of Mexico from MNAR (Figure 9).

Esri compiles advanced demographic datasets sourced globally by Michael Bauer Research. For Mexico, the data is based on the latest statistical records (National Survey of Demographic Dynamics 2018) from INEGI. This study uses demographic records for the Basin of Mexico from the Esri Global Demographics database.

3 Methodology

Data processing in this study was completed using ArcGIS Pro (v2.5), Generic Mapping Tools (GMT) (v5.3.2) and Google Earth Pro software.

3.1 Seismic Sources

GMT (v5.3.2) for Linux was used to process peak ground acceleration (cm/s^2) records from the CFE and seismic moment tensor data from the Global CMT Project to analyse the spatial distribution and effect of seismic sources on the Basin of Mexico.

3.2 Fault Digitation

Location of active fault extensions and fault line networks in the Basin of Mexico are ongoing areas of research. To accurately regionalise the SC fault and analyse the relevance of proximal seismic activity, it is important to understand the relationship between recognised tectonic fault systems and historic hypocentre distribution of low magnitude ($<M 3.0$) seismic events in the Basin. This study integrates the fault line data published from seven sources (Perez-Cruz, 1988, Arce *et al*, 2015 and 2019, Garcia-Palomo *et al*, 2008a & 2008b, Campos-Enriquez *et al*, 2015, Gonzales Torres *et al*, 2015) to incorporate fault systems from; (1) the Sierra de las Cruces and the Chichinautzin Monogenetic Field with; (2) linear networks distributed throughout the ancient lakes of Chalco, Xochimilco and Texcoco. Fault lines were digitised with Google Earth Pro using image overlays from stratigraphy maps published in the eight sources referenced above. Using the WGS-1984-UTM-Zone-14Q coordinate system the scaled images were used as point references to obtain an accurate regionalisation. The faults were then digitised using the polygon tool.

3.3 Numerical Analysis

3.3.1 Shallow Crustal Fault Schematics

Figure 8 is a modified version of the original illustration by Mooser (2018), translated from Spanish. The 2D illustration uses a disproportional scale which limits the accuracy when interpreting the exact location of the inferred fault systems. To account for this, when identifying the location of the proposed SC fault, the illustration from Mooser (2018) was compared with the Digital Elevation Model on the tectonic systems in the Basin of Mexico by Arce *et al* (2019) (See appendix Figure 26). This helped generate georeferences for the location labels and the geological features from Mooser's (2018) illustration, using Google Earth Pro. Using the WGS-1984-UTM-Zone-14Q coordinate system for the geological features in the Basin and the adaptive Google Earth grid tool, the initial location of the proposed SC fault is believed to align between the Chichinautzin Monogenetic Field and the Santa Catarina Graben, trending NE-SW from Cerro del Ajusco (19.211006°, -99.257384°) to Cerro Yuhualixqui (19.318569°, -99.029898°) (Figure 8).

Seismicity along the Mexican subduction zone is irregular, occurring at a maximum depth of 100km. The absence of a well-defined 'Benioff Zone' (typically extending 500km) makes it difficult to identify the crustal limits. The Meso-America Subduction Experiment (MASE) analysed the crustal structure with a 600km linear array (100) of Güralp 3T broadband seismometers using Receiver Function Analysis as a method to detect the interface of seismic waves between crust and mantle. Perez Campos (2008) initially proposed that the thickness of the lower continental plate beneath the Basin of Mexico was ≤ 55 km. Ferrari *et al* (2012) later supported these findings by compiling results from the MASE, Mapping the Rivera Subduction Zone (MARS) and the Veracruz-Oaxaca seismic line (VEOX) receiver function analysis with Urrutia-Fucugauchi and Flores-Ruiz's (1996) gravimetric model to determine the thickness of the upper plate (Figure 9).

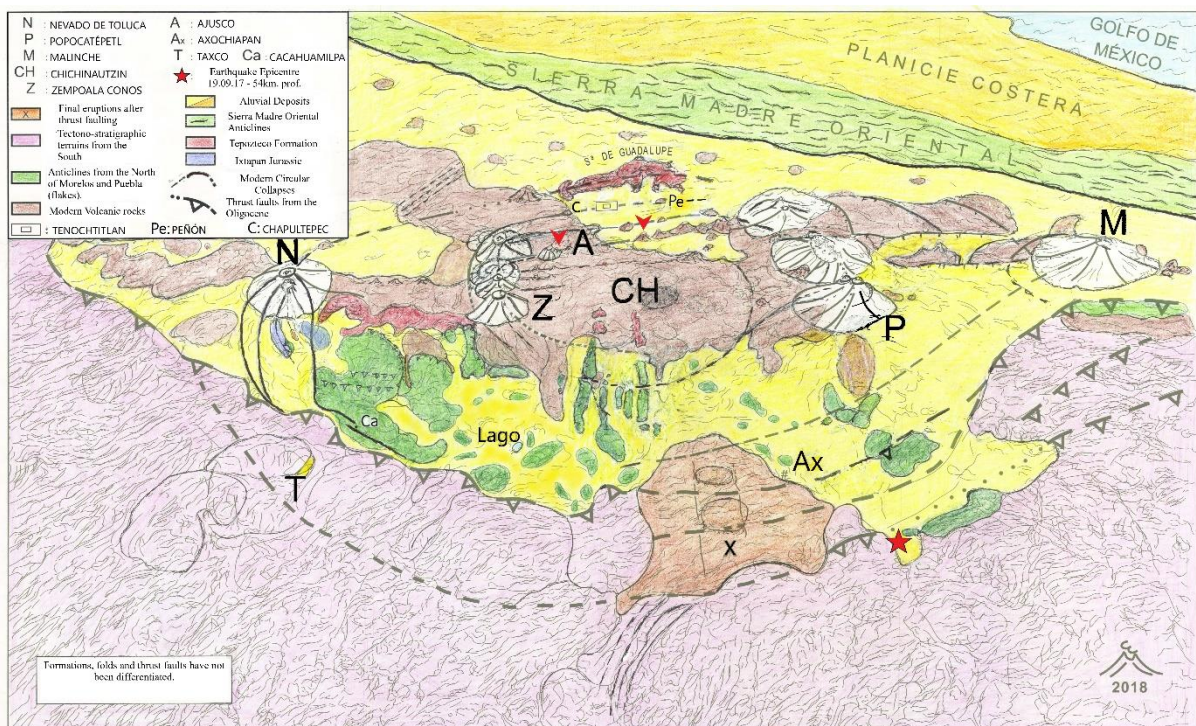


Figure 8. Tectonic setting and fault stratigraphy in the east of the Trans-Mexican Volcanic Belt between Nevado de Toluca and Malinche Volcanoes. The dashed lines represent modern circular collapses believed by Mooser to be sequences of SC faults. The inverted red arrows identify the location of the proposed alignment of the SC fault between Cerro del Ajusco (19.211006° , -99.257384°) and the southern tip of the Santa Catarina Range (19.318569° , -99.029898°). Modified from Mooser (2018).

This study integrates results from the lower North American plate limits from Ferrari *et al* (2012) with data from the National Seismological Service (SSN) on the hypocentre distribution of seismic events in the Mexican Basin between 1974 (Beginning of SSN seismic records for the Mexican Basin) and 2020. GMT (v5.3.2) and ArcGIS Pro (v2.5) are used to analyse the distribution of hypocentres within 40km of the SC fault extension (Figure 10). Spatial correlations in the data were identified using the following format to account for location errors in the seismographs; (1) maximum distance of 2.5km between hypocentres, (2) maximum variance of 0.5km from centre in a linear distribution and, (3) maximum deviance of 10km from the SC extension. The depth of the SC fault was estimated using the average hypocentre depth from the optimal spatial correlation.

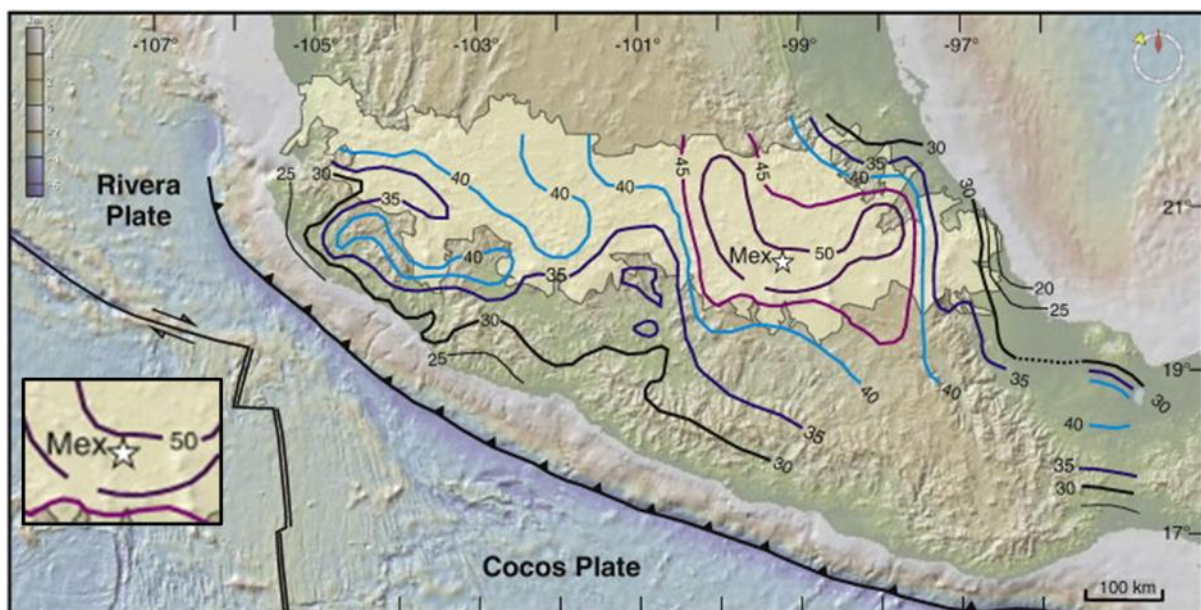


Figure 9. Crust thickness beneath the south of the TMVB. Contours correspond to the depth of the North American plate (km). The Basin of Mexico is identified by the white star. Modified from Ferrari *et al* (2012).

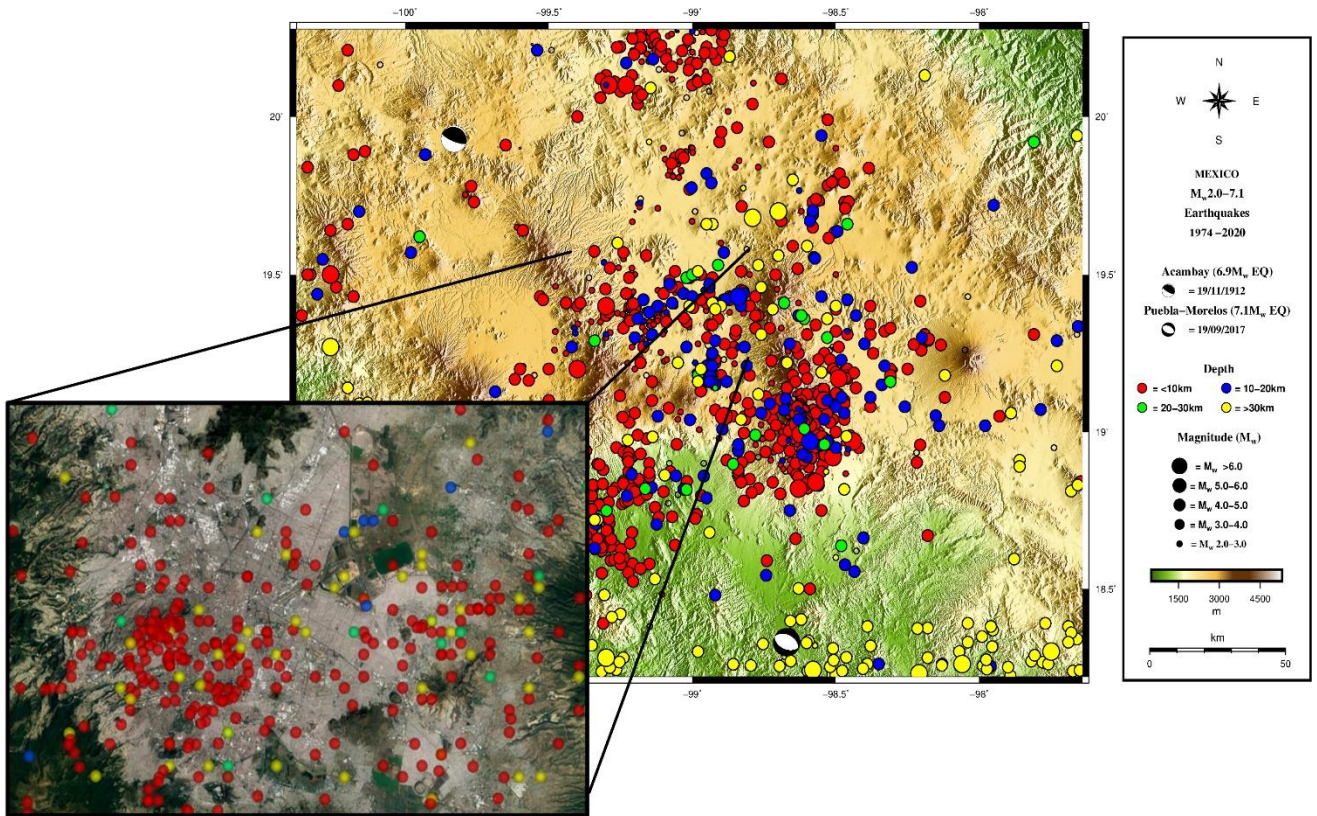


Figure 10. Depth distribution of seismic events in the Basin of Mexico and adjacent volcanic ranges from 1974-2020, including focal mechanisms of the 19/11/1912 Acambay (19.93° , -99.83°) and 19/09/2017 Puebla/Morelos (18.3297° , -98.6712°) earthquakes. Data from the Global CMT Project and the SSN. Created using GMT 5.3 for Linux and Google Earth Pro.

3.3.2 Fault Displacement

The moment magnitude (M_w) scale, developed by Hanks and Kanamori (1979), is the contemporary method of calculating the size of an earthquake based on its seismic moment (M_o). It replaced the (Gutenberg-Richter) local magnitude (M_L) and surface wave magnitude (M_s) scales, which were also logarithmic, but only accounted for certain frequencies and distance ranges for body and surface waves. For the purpose of this study however, considering there is currently no strike, dip and rake information from a known SC fault related seismic event in the Basin nor data on the fault slippage, Slemmons (1982) original magnitude scaling equation is used, which utilizes fault length to project a hypothetical maximum surface wave magnitude output (M_s), in this case the estimated fault length (L) from the inferred shallow crustal fault (Equation 1).

(1) Maximum Magnitude (M_s) output

$$\text{Normal Fault: } M_s = 0.809 + 1.341 \log(L)$$

3.3.3 Amplification Factor

Seismic wave amplification has been successfully simulated using one-dimensional (1D) topographic models to display the velocity contrast between soil layers (Sánchez-Sesma *et al*, 1988; Semblat, 2011). This study creates a 1D amplification factor model for a 11km cross-section between San Pedro Martir (19.268424°, -99.164202°) to Camino Cerro de la Estrella (19.342232°, -99.090000°). Surface elevation values were recorded at 100m intervals to model the topographic variation typical of the transition from hard rock outcrops to interbedded soft lake deposits, using the Google Earth Pro elevation tool. Micro-zoned basin geometry (MNAR) is integrated with the basin soil-velocity structure by Cruz *et al* (2016) (Table 1) to calculate the general soil layer schematics for the intersected transition and lake zones.

To calculate the propagation time of seismic waves between soil layers, equations (4) and (5) can be used where $T = \text{Time period (s)}$, $H = \text{Thickness (m)}$, and $V = \text{Velocity (m/s)}$.

(2) Single Soil layer

$$T = \frac{4 \sum H_i}{V_s}$$

(3) Multiple Soil layers

$$T = \frac{4 \sum H_i}{\sum_{i=1}^n V_i H_i}$$

Seismic Micro Zone	H (m)	V_p (m/s)	V_s (m/s)
A	30	800	50
B	20	1200	100
C	250	2000	400
D*	250	2500	800
E*	1420	2700	1560

Table 1. General velocity structure of the soil microzones in the Basin of Mexico (Cruz et al, 2016). V_p and V_s correspond to P-wave and S-wave velocity. The stars indicate the deepest points of the Basin.

3.4 Visual Observations

To understand the effect of strong ground motion from a large seismic event on the infrastructure in the Basin of Mexico, visual observations were taken on 19th February 2020 of buildings that experienced damage from the M_w 7.1 Puebla/Morelos earthquake on 19/09/2017. Observations were taken in each soil zone (Figure 11) to account for variation in seismic – soil interaction. To confirm the observed structural damage resulted from ground motion in 2017 and not from an alternative peril like local subsidence, locations were selected with the help of Alberto Galaviz, a Mexico City resident and geophysicist from CENAPRED, and supported with eye-witness accounts from residents interviewed at each dedicated observation site. The Structural Damage Index and Ground Failure Index (Franke et al, 2019) were used to categorise damage and identify seismically deficient structures.

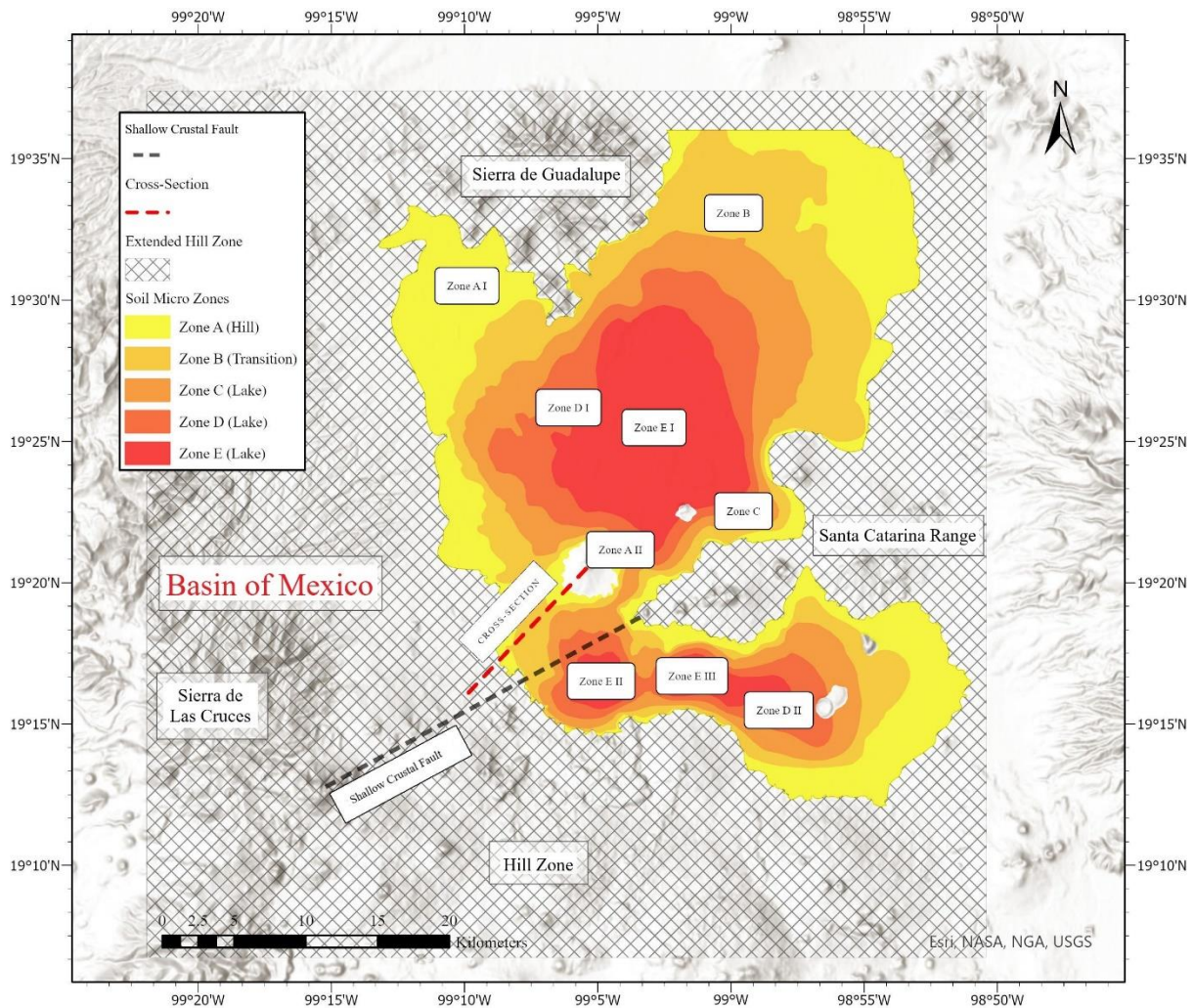


Figure 11. The Basin of Mexico subdivided into seismic micro-zones based on soil composition. Zones A and B represent the Hill and Transition soil zones. Zones C, D and E represent the lake zone. Seismic zones ‘D’ and ‘E’ are divided into I, II, and III respectively, in accordance with variation in bed rock depth and the period of lake deposits (Alberto et al, 2018). Beyond Zone A, the Hill zone extends to the Basin limits between the Sierra de Las Cruces and the Sierra Nevada (W-E). The proposed SC fault is represented by the black dashed line. The red dashed line corresponds to the cross-section used for the 1D amplification model. Created using ArcGIS Pro (v2.5).

3.5 Demographic Analysis

The possible existence of an active fault in the Basin of Mexico poses a potential high risk to the inhabitants and socio-economic stability of Mexico City and its adjacent suburban areas. This study explores the general demographic of the Basin of Mexico using data from Esri Global Demographics with ArcGIS Pro. Population and household density in the Basin of Mexico is analysed using infographics, in line with the soil microzonation, to identify demographic distribution per soil zone. Wu and Kanamori (2008) analysed the accuracy of earthquake early warning (EEW) system methods, providing advanced warning time to pre-programmed emergency responses of imminent ground motion. A fundamental concept of the EEW system is the use of an earthquakes preceding P-wave characteristics to determine source-site distance and ground motion associated with the S-wave. To understand the potential for early warning from a displacement in the Basin of Mexico, the distance between the proposed SC fault and the most densely populated municipalities in the Basin is calculated using Google Earth Pro and compared with the reception of the P to S-wave time interval from the 2017 Puebla-Morelos Earthquake.

4 Results

4.1 Fault Schematics

A digital elevation model (DEM) of normal, reverse and thrust faults in the Basin of Mexico can be seen in Figure 12. The initial georeferenced SC fault orientates 23.9km NE-SW in the south of the basin, striking in a similar direction to the Contreras and Satellite normal faults (Garcia-Palomo *et al*, 2008a), the Santa Catarina Graben (Gonzales Torres *et al*, 2015) and a second graben structure in the lacustrine zone, 5km SSE of the Sierra de Guadalupe (Arce *et al*, 2019). The north-west margin of the shallow crustal fault is located ~1.1km from the southern edge of the Santa Catarina Graben footwall. In the south-west, the SC fault trends parallel to the Contreras fault for ~6.8km, from Cerro del Ajusco to Tlalpuente. Historic seismic surveys and geological studies indicate no prior existence of a fault between Cerro del Ajusco and Cerro Yuhualixqui, however, in accordance with the regionalisation, the SC fault intersects a western section (19.230967° , -99.217834°) of the Xochimilco fault, 1.6km SW of Xitle monogenetic volcano, and a southern section (19.301530° , -99.079458°) of the Mixhuca fault, ~0.3km from Valle de San Lorenzo.

The estimated mean depth of the SC fault is based on the depth distribution of seismic events in the south-west region of the Mexican Basin. Figure 13 displays epicentres from 106 seismic events, between 1974 and 2020 (See appendix Table 15-18), categorised into 2.5km radius intervals from the SC fault to a maximum radius of 10km. A total of 31 (29.2%) seismic events occurred within 60 days of a major national seismic event ($M_w \geq 5$) (See appendix Table 18). In conjunction with the temporal relativity to national earthquakes ($M_w \geq 5$), a linear trend was identified using spatial classification that limits the distance between hypocentres to $\leq 2.5km$ and the variance from the centre of an alignment to $\leq 0.5km$. The trend includes 19 (61.3%) (Table 2) of the 31 seismic events in a 23.5km linear alignment (Figure 13) between Xitle volcano and Iztacalco, ~3.6km north of the projected SC fault with a $+15^\circ$ tilt, orientated NNE-SSW.

Of the 19 seismic events, 14 (74%) occurred within 30 days of a national earthquake of $M_w \geq 5$ and 9 (47%) occurred within 5 days (Table 4). The trend has incremental activity since 1974 and a lateral extension that directly correlates, within 2%, to the length of the SC fault. Considering this relationship, the mean depth of the linear trend at -6.74km (Table 3) was established as the mean depth for the SC fault.

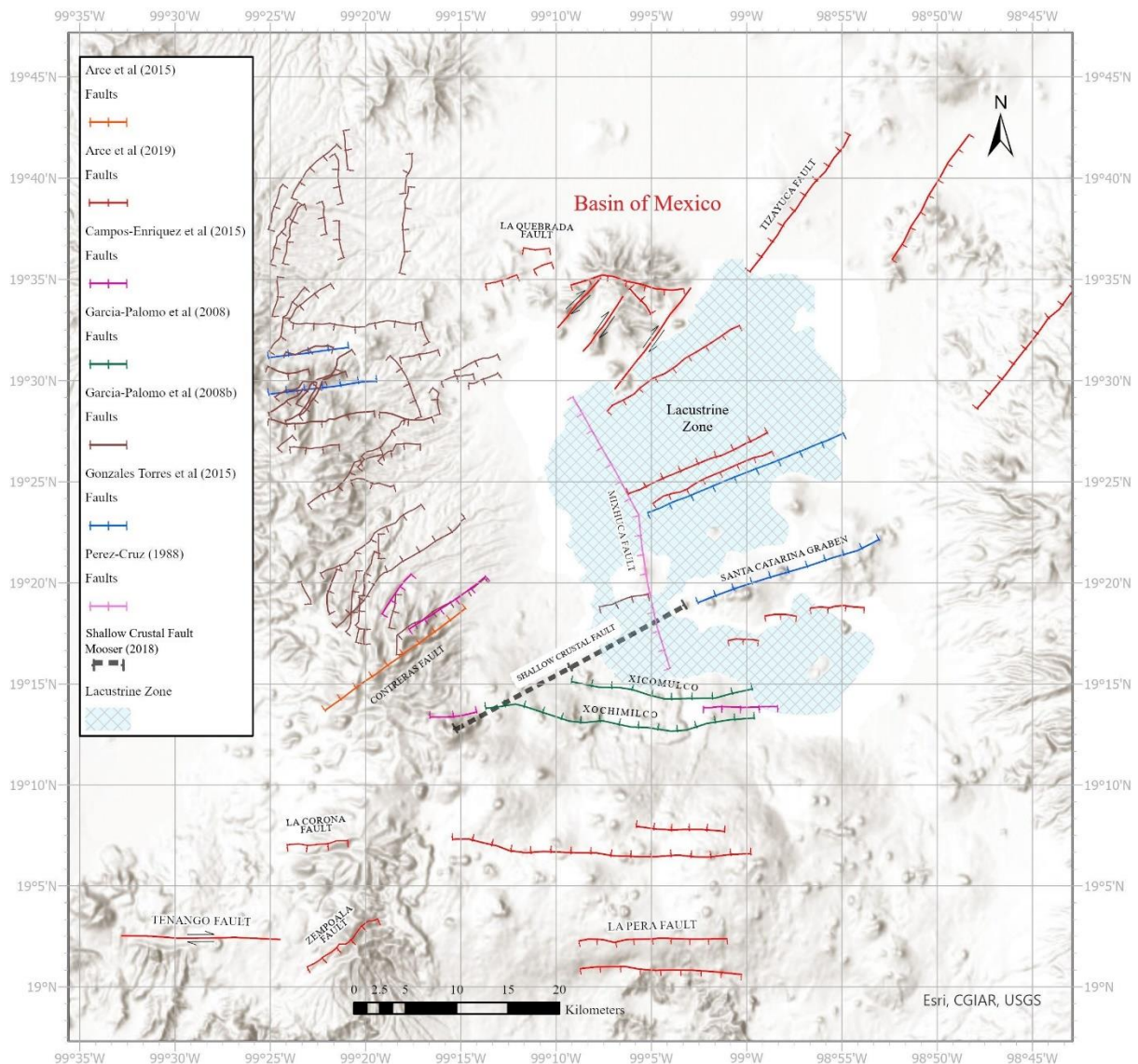


Figure 12. Digital Elevation Model (DEM) showing the distribution of inferred normal and thrust faults in the Mexican Basin compiled from recent geophysical studies, colour-coded by author. Data integrated from; Arce et al (2015 & 2019), Campos-Enriquez et al (2015), García-Palomo et al (2008a & 2008b), Gonzales Torres et al (2008a & 2008b) and Pérez-Cruz (1988). The black dashed line represents the proposed SC fault (Mooser, 2018). Created using ArcGIS Pro (v2.5).

Event	Date	Hour	Magnitude (M)	Latitude	Longitude	Depth (km)
1	13/07/1974	21:09:59	non calculable	19.34	-99.14	-5
2	26/01/1977	12:10:11	non calculable	19.3	-99.18	-1
3	04/12/1983	12:57:32	non calculable	19.26	-99.22	-4
4	06/04/1999	07:20:04	2.8	19.38	-99.09	-13
5	15/12/1999	22:31:04	2.4	19.27	-99.21	-9
6	15/12/1999	22:25:07	2.6	19.28	-99.2	-20
7	21/04/2002	04:23:16	3.1	19.44	-99.03	-11
8	16/04/2005	18:04:07	3.4	19.41	-99.07	-19
9	16/06/2013	13:15:22	2.7	19.3467	-99.1317	-1
10	25/08/2013	15:35:01	2.1	19.353	-99.1213	-5
11	25/08/2013	15:43:41	2.3	19.3725	-99.0995	-9.5
12	09/04/2015	03:38:16	2.3	19.4022	-99.0728	-7
13	21/06/2015	11:52:12	1.8	19.3293	-99.1553	-4.2
14	01/03/2017	03:57:21	2.4	19.3417	-99.1345	-2.2
15	09/09/2017	21:54:12	2.7	19.2965	-99.1813	-8.5
16	20/09/2017	04:32:55	1.3	19.266	-99.2108	-2.2
17	20/09/2017	00:14:01	1.7	19.276	-99.2058	-4.5
18	27/09/2018	22:56:39	2.1	19.32	-99.163	-1
19	03/07/2020	22:05:16	2.1	19.39	-99.08	-1

Table 2. Hypocentre data for seismic events located along the 23.5km linear trend in the Basin of Mexico (Figure 13). Data from SSN Mexico.

Date Range	Total Number of Seismic Events	Magnitude Range (M)	Mean Depth (km)
1974-2020	19	1.3-3.4	-6.74

Table 3. Seismic event summary for linear trend (Table 2).

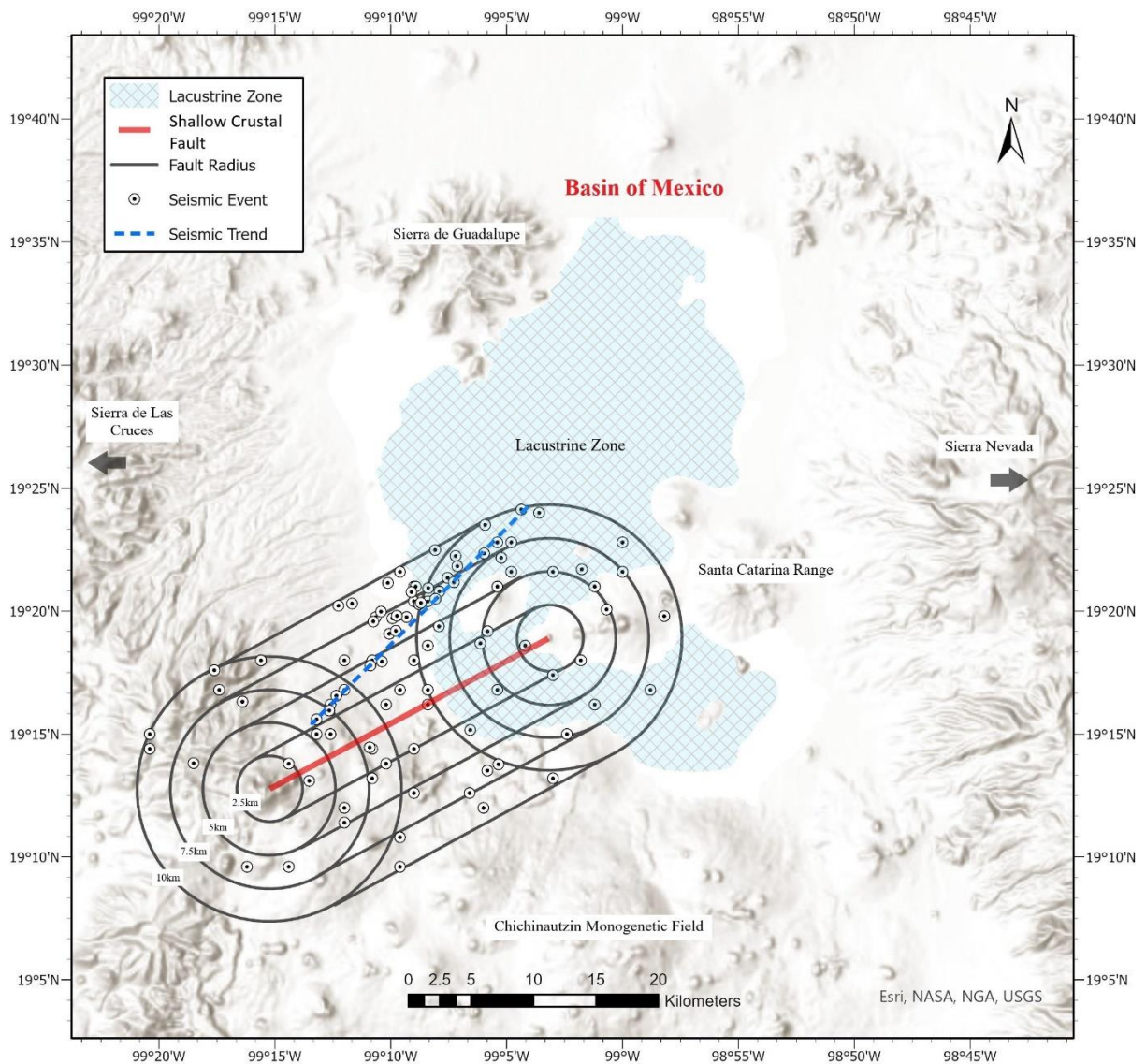


Figure 13. Digital Elevation Model (DEM) of the Mexican Basin displaying seismic events since 1974 (beginning of seismic recording) within 10km of the projected SC fault. Seismic events are categorized into 2.5km radius intervals from the fault. The 23.5km linear trend corresponds to events used to estimate the depth of the SC fault. Created using ArcGIS Pro (ArcGIS Pro | 2D and 3D GIS Mapping Software (esri.com))

Mexican Basin Seismic Event (Linear trend)	Total Annual Seismic Events $M_w > 5$ in the Republic of Mexico	National Seismic Events $M_w > 5$ with corresponding dates to the events in the Basin of Mexico		Days Prior to Basin Event
		Magnitude (M_w)	Date	
13/07/1974	11	6.3	31/05/1974	43
26/01/1977	7	5.2	04/01/1977	22
04/12/1983	17	5.3	25/11/1983	9
06/04/1999	11	n/a		n/a
15/12/1999		5.6	21/11/1999	24
15/12/1999				
21/04/2002	25	6.5; 6.0; 5.5; 5.3	18/04/2002	3
		5.0	21/04/2002	Same day
16/04/2005	12	5.6	27/02/2005.	48
16/06/2013	19	5.8	16/06/2013	Same Day
25/08/2013		5.0; 6.0	21/08/2013	4
25/08/2013				
09/04/2015	20	6.2	22/02/2015.	46
		5.4	20/03/2015.	20
21/06/2015		5.6	28/04/2015.	54
01/03/2017	19	5	13/02/2017	19
09/09/2017		8.2	08/09/2017	1
20/09/2017		7.1	19/09/2017	1
20/09/2017				
27/09/2018	20	5.2; 5.0	24/09/2018	3
03/07/2020	16	6.1	22/05/2020.	42
		5.2	02/07/2020	1

Table 4. National seismic events (1974-2020) of $M_w \geq 5$ that have occurred ≤ 60 days prior to seismic events from the linear alignment in the Basin of Mexico (Table 1). Data from SSN and Global CMT project.

4.2 Fault Displacement

Shown below is Slemmons (1982) normal fault scaling equation to calculate the maximum magnitude (M_s) output from a full-length fault rupture. The length of the linear seismic trend and the regionalised SC fault were averaged at 23.7km (Figure 13).

$$L = \text{Length (m)}$$

$$M_s = \text{Surface Wave Magnitude}$$

(1) Maximum Magnitude Output (M_s)

$$M_s = 0.809 + 1.341 \log(L)$$

$$M_s = 0.809 + 1.341 \log(23,700)$$

$$= M_s 6.7$$

4.3 1D Amplification Factor Model

The following velocity-structure equations have been used to determine seismic (P or S) wave propagation time between soil layers in the Mexican Basin.

$$T = \text{Time period (s)}$$

$$H = \text{Thickness (m)}$$

$$V = \text{Velocity (m/s)}$$

a) Single layer

$$T = \frac{4 \sum H_i}{V_s}$$

b) Multiple layers

$$T = \frac{4 \sum H_i}{\sum_{i=1}^n V_i H_i}$$

(1) Soil Layer One

$$T = \frac{4 \sum 30_1}{50}$$

$$T = \frac{120}{50}$$

$$T = 2.40s$$

(2) Soil Layers One & Two accumulated

$$T = \frac{4(\sum 30_1 + 20_2)}{\frac{\sum_{i=1}^n (50_1 \times 30_1) + (100_2 \times 20_2)}{\sum 50}}$$

$$T = \frac{200}{\frac{3500}{50}}$$

$$T = 2.86s$$

Seismic Micro-Zone	H (m)	Vp (m/s)	Vs (m/s)	Accumulated Time Period (s)
A	30	800	50	2.40
B*	20	1200	100	2.86*

Table 5. Velocity structure summary for the San Pedro Martir - Camino Cerro de la Estrella cross-section. *The time period in microzone B accounts for the combined layer thickness with zone A (edited from Cruz et al, 2016).

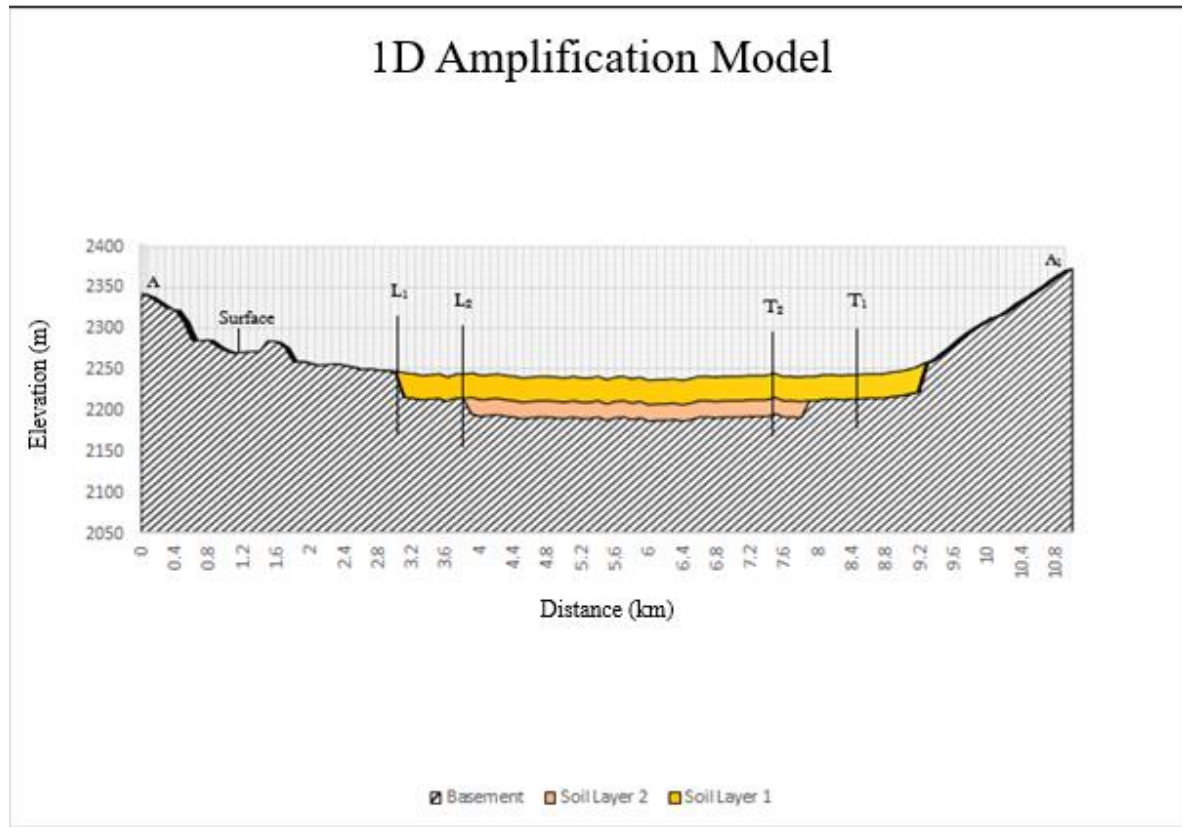


Figure 14. 1D amplification factor model for the 11km cross-section from San Pedro Martir (19.268424°, -99.164202°) to Camino Cerro de la Estrella (19.342232°, -99.090000°) in the Mexican Basin (100m resolution). L_1 and L_2 represent soil layers from zones A and B. T_1 and T_2 correspond to the propagation time of seismic waves through the respective soil layers. Velocity structure and soil layer thickness edited from Cruz et al.

The 11km cross-section (Figure 15) provides an insight into the pronounced subsurface soil transitions in the south-west of the Mexican Basin. The amplification model (Figure 14) illustrates the relationship between the time period of P and S wave propagation (L_1 - 2.40s, L_{1+2} - 2.86s) (Table 5) following a seismic event and the progressive thickness of the soil layers within the basins lacustrine zone (L_1 - 30m, L_{1+2} - 50m). In Figure 15 the SC fault can be seen to intersect four seismic microzones of different

soil composition, between Aldama and Cerro Yuhualixqui, encompassing hard volcanic rock, compact alluvial deposits (sands and gravels) and interbedded soft clays.

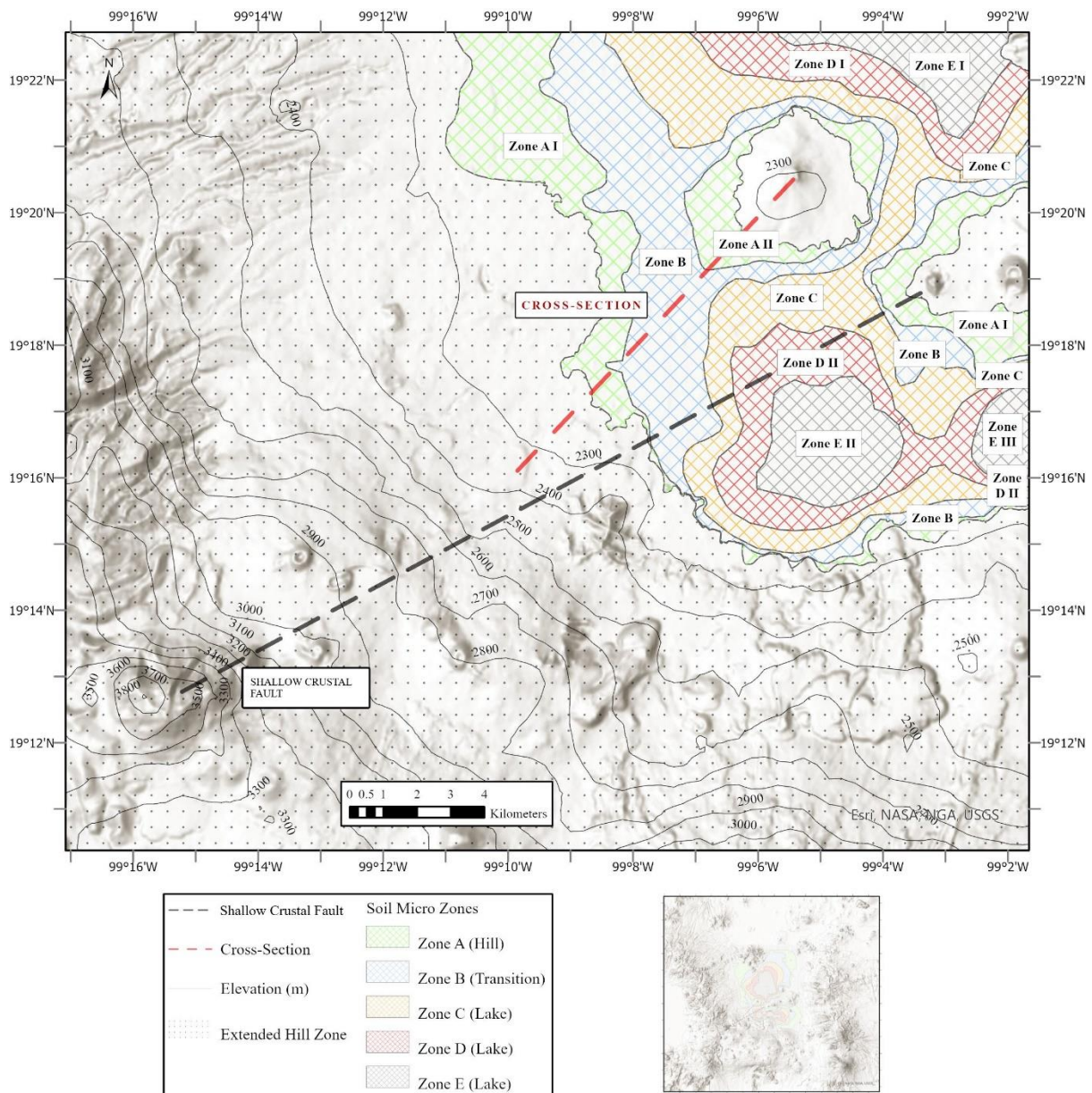


Figure 15. DEM for the south-western region of the Basin of Mexico displaying the 11km cross-section for the 1D amplification model between San Pedro Martir (19.268424°, -99.164202°) and Camino Cerro de la Estrella (19.342232°, -99.090000°), the 23.9km proposed SC fault and the designated soil microzones. Bottom right shares a scaled view of the study area in reference to the wider basement. Created using ArcGIS Pro (v2.5).

4.4 Visual Observations of structural damage

The following photographs display buildings constructed on the three main soil zones in the Basin of Mexico (Figure 15). Visible damage to the infrastructure has resulted from strong ground motion experienced during the M_w 7.1 Puebla/Morelos earthquake in 2017. The photographs were taken between 19/01/20-20/01/20.

Based on the form and construction materials, the buildings shown in Figure 16 are believed to be constructed in line with the (Soil Category: I - Firm; Structural group: Residential <30m height - B2) revised 2004 Mexico City Building Code (MCBC) (Alcocer, 2008). Following the Structural Damage Index proposed by Bray *et al*, 2000 (Table 6), the residential building in El Jasmin (Figure 16a; 16b) has visible D₁ superficial fracturing to the residence walls with newly fitted glass windows replacing cosmetic damage incurred during the 2017 earthquake. The building entrance (Figure 16c) has D₃ damage to the fixed supporting materials above the gateway arch, with D₁ surface fractures in the residence walls. It is possible that the load-bearing structure surrounding the gate was weakened by the interbedded metal bolts (Figure 16c). The main residence (right of figure 16c) displayed similar D₁ cosmetic fracturing to the exterior.

Located in the transition zone by the Santa Cruz Acalpíxca stream, the Archaeological Museum of Xochimilco (Figure 17a; 17b), inaugurated in 1979, was renovated from an old Santa Cruz pump house. In 2017 the museum experienced D₃ fracturing in the roof (Figure 17) and a D₄ internal collapse to several supporting columns, breaching the structural integrity of the building. The initial museum renovations (1973) were built on the dated pump house foundations which would likely be classified as 'seismically deficient' or illegitimate under the (Soil Category: II - Transition; Structural group: Other <30m height - B2) revised 2004 structural design code (Alcocer, 2008). The residential building in Santa Cruz (Figure 17c), located within 1km of the Archaeological Museum of Xochimilco, maintains a construction design consistent with surrounding retrofits, suggesting compliance with the MCBC regulations for transition soil developments. Visible damage is limited to widespread D₁ fracturing on the exterior.

Figure 17d showcases a common construction design in Mexico City whereby the resident extends the building form from the ground floor which initially abides by the MCBC, and develops two additional illegitimate floors using alternative, less costly building materials. Dislodged bricks can be observed from the top floor with D_2 fracturing visible throughout the interbedded cement work.

At the boundary between the Transition (Zone B) and Soft (Zone C) soil strata in San Jerónimo, 3m vertical fractures can be observed traversing the joining section of a wall at the SW entrance to Zacapa Canal (Figure 18). The canal is one of the remaining southern channels of lake Xochimilco. Similar D_2 damage is visible across most wall intersections and load-bearing columns constructed on the lake sediments surrounding the canal (See appendix Figure 29).

Index	Description	Observation/Interpretation
D₀	No damage	No evidence of cosmetic fracturing or superficial interior damage
D₁	Light damage	Superficial fracturing, no damage to key structural elements
D₂	Moderate damage	Fracturing to buildings' load-bearing elements but structure intact
D₃	Heavy damage	Deformation surrounding fractures on buildings' load-bearing elements, requires immediate attention to maintain integrity
D₄	Partial Collapse	A portion of the building experiences structural collapse
D₅	Full Collapse	Complete breach of structural integrity, the key structural elements do not remain

Table 6. Structural damage index (modified from Bray *et al*, 2000).





Figure 16. Residential buildings in El Jazmin, Xochimilco, part of a large neighbourhood constructed on an elevated hard rock outcrop (firm soil zone). Photographs taken 19/01/2020.









Figure 17. The Archaeological Museum of Xochimilco (17a and 17b) and residential buildings (17c and 17d) in Santa Cruz Acalpíxca (transition soil zone). Photographs taken 19/01/2020.





Figure 18. Walls (4m x 0.5m) delineating the SW entrance to the Zacapa Canal in San Jeronimo, Xochimilco (lake soil zone). Photographs taken 19/01/2020.

The Ground Failure Index, modified from Franke *et al* (2019), has been used here to describe ground deformation induced by major seismic motion in 2017 (Table 7). Adjacent ($\approx 100\text{m}$) to the Zacapa Canal, D_2 fracturing can be observed on the load-bearing columns and support foundations of fencing encircling an old pumphouse (Figure 19a & 19c).

Index	Description	Interpretation
G₀	No deformation	No visible changes to ground integrity
G₁	Minor deformation	No lateral movement; deformation <10cm; ground tilt <1 degree
G₂	Moderate deformation	Small lateral movements; deformation $\approx 10\text{-}25\text{cm}$; ground tilt 1-3 degrees
G₃	Significant deformation	Considerable lateral movement >25cm; deformation >25cm; ground tilt >3 degrees

Table 7. Ground Failure Index modified from Franke *et al* (2019).

The damage in Figure 19 is visible throughout the entire fencing support structure. Located between the pumphouse and canal is a cobbled walkway (Figure 19b). Fracturing (E-W trending; 2–2.5m) in the ground surface is visible with uplifted tiles and G_2 lateral deformation. As with Figure 18, the fracturing occurs at an intersection, whereby a change of direction is highlighted by a 2cm gap between separate sections of the walkway. There were three observed repetitions of the G_2 lateral deformation at similar intersections of the walkway.





Figure 19. Short load-bearing columns and foundation walls supporting a metal fence surrounding a pump house adjacent to Zacapa canal (19a and 19c). Cobbled walkway between the pump house and the canal (19b) (lake soil zone). Photographs taken 19/01/2020.

The Enrique Rébsamen Primary School failure (Figure 20) is a well-documented case of illegitimate construction, which left thirty-seven dead following the 2017 earthquake. Located in the transition zone, the original three floor design (Figure 20c) used a reinforced concrete (RC) frame, which was never re-evaluated under the revised retrofit process following the M_w 8.0 1985 Michoacán earthquake and was later subject to illegitimate modification with the addition of a private apartment on top of the original structure (Estêvão, 2020). It is clear from Figure 20 that the buildings were seismically deficient. One of the two buildings can be classified as D_5 after complete collapse, with the remaining structure (Figure 20a and 20b) incurring D_4 collapses in the external walls and D_3 damage around the RC beams.

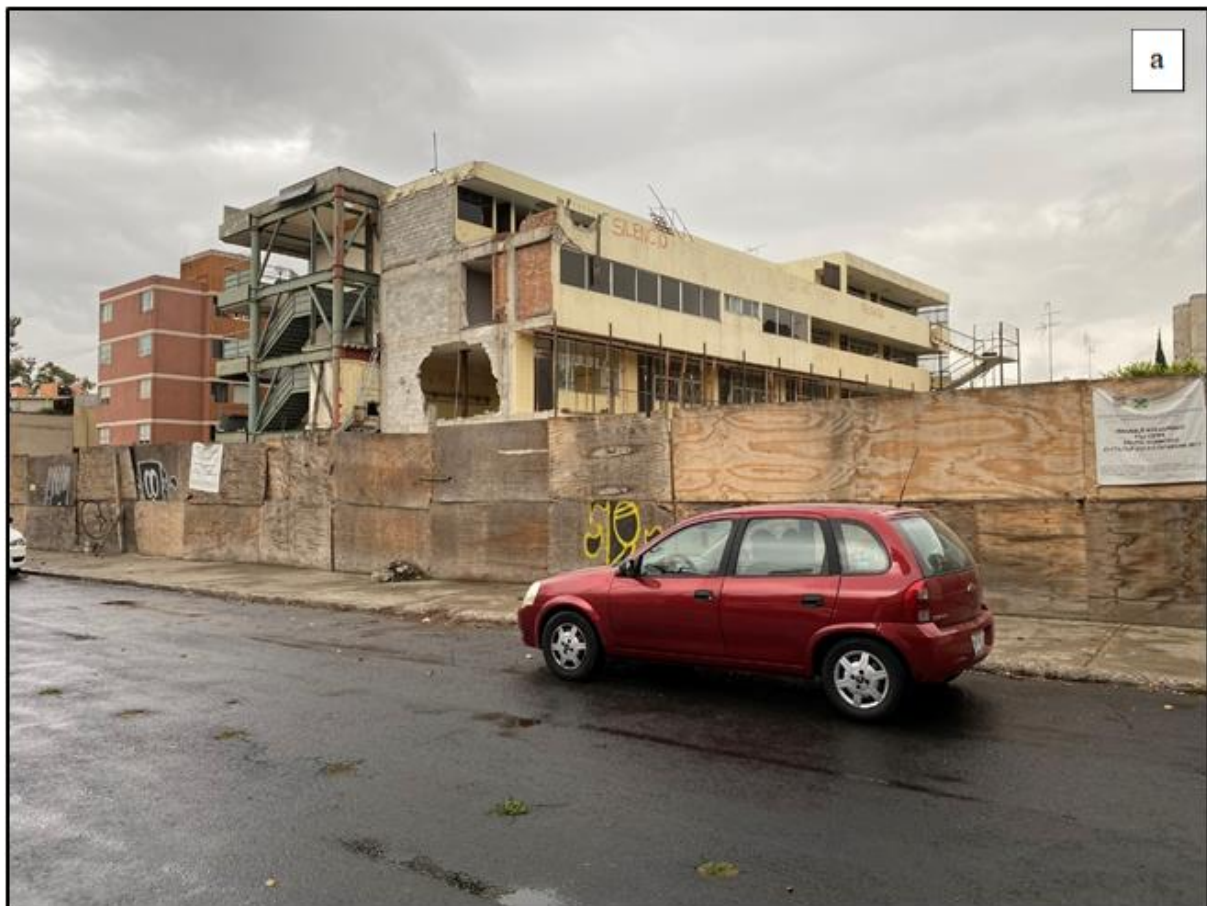






Figure 20. Before and after photos of Enrique Rébsamen primary school, Tlalpan (lacustrine soil zone). 20a & 20b taken 20/01/2020. 20c from Google maps.

From the direct visual observations taken throughout sites in the soil microzones (Figure 21), it is evident that reinforced concrete structures or buildings that fail to comply with the requirements of the revised MCBC (Alcocer, 2008), experienced more damage and/or partial collapse from ground motion during the 2017 Puebla/Morelos earthquake. It can also be said that collapsed buildings and structures with severe damage tended to concentrate in the respective transition (Zone B) and lake (Zone C) zones, with foundations being constructed on lacustrine deposits or interbedded soft clays (Figure 21).

According to SASMEX, ground motion was experienced for ~20 seconds during the M_w 7.1 Puebla/Morelos earthquake. Structural damage records from the Mexican National Atlas of Risk indicate that a total of 173 buildings experienced total collapse (43%), partial collapse (14%), or severe damage (43%) (Table 8). Over 98% of the 173 buildings were located within a seismic microzone, with ~79% of damaged or collapsed buildings constructed on compact alluvial deposits in the transition zone (Figure 21 - Zone B).

Total Building Collapse	Partial Collapse	Severe Damage/Breach in structural integrity	Greatest damage per soil zone	Shake Time (s)	Warning Time (s)
75	24	74	Transition Zone (~79%)	~20	~19

Table 8. Building damage summary for the 2017 Puebla/Morelos earthquake (displayed in Figure 21). Structural damage data from MNAR. Seismic alert data from SASMEX.

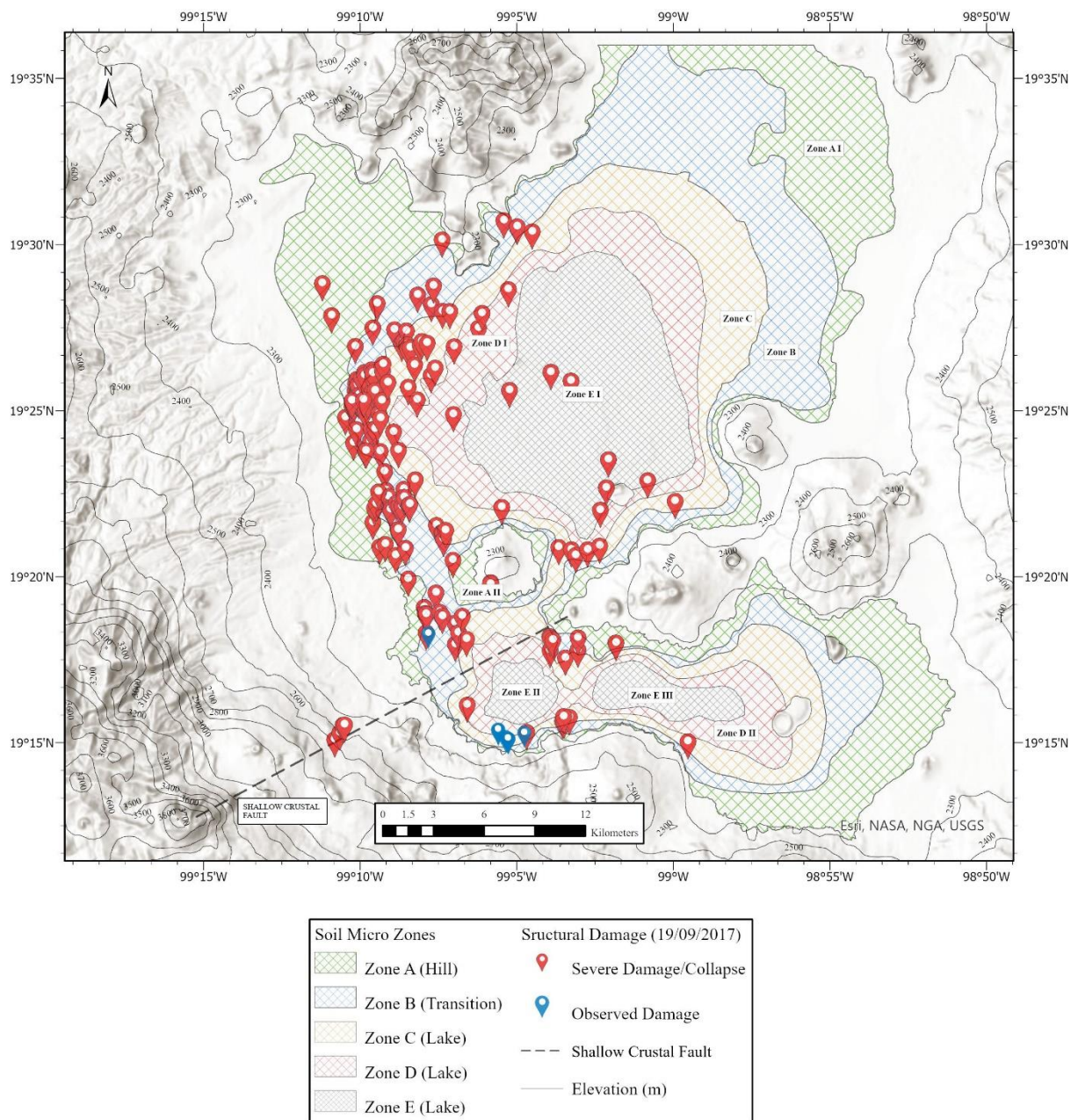


Figure 21. Structural damage reported in the Basin of Mexico, following the 19/09/17 Puebla-Morelos earthquake, in accordance with the geotechnical soil zones. Red pointers represent collapsed buildings or buildings that experienced severe structural damage. Blue pointers correspond to the observed damage sites on the 19/01/20. Severe damage adapted from the Mexican National Atlas of Risk (MNAAR). Created using ArcGIS Pro (v2.5).

4.5 Demographic Analysis

Population density distribution by municipality inside the Basin of Mexico is displayed in Figure 22, including the 16 municipalities in the State of Mexico City and 21 from the neighbouring State of Mexico. The municipalities share an average population density of 7,210 per km² and a range of 17,240 people per km². Residing in the central region of the basin, 6 of the 37 municipalities (~16%) exceed population densities of 16,000 per km² (over 222% above average), aggregating within the transition and lake seismic microzones (Figure 23). Iztacalco (Mexico City State) holds the highest population density with 17,444 per km², closely followed by Nezahualcóyotl (State of Mexico; 17,323 per km²), Cuauhtémoc (Mexico City State; 16,745 per km²), Benito Juárez (Mexico City State; 16,200 per km²), and Iztapalapa (Mexico City State; 16,101 per km²) which also has the largest total population per municipality of 1,835,486 (Figure 22).

In the south-eastern region of the basin, population density decreases to less than 1,500 per km² in 4 municipalities (~11%). Juchitepec holds the lowest population density in the Basin at 204 per km² as well as the lowest total population per municipality at 27,116. Also, in the State of Mexico, Texcoco (645 per km²) and Ixtapaluca (1,437 per km²) closely follow. Milpa Alta has the lowest density in Mexico City State at 511 per km². Following Figure 22, as you radiate from the centre of the basin towards the south and east, there is a general increase in municipality size by area (km²) (Figure 22) and a decline in total population (See Appendix). If you radiate north-west from the centre of the basin, the spatial trend is less pronounced, with municipalities maintaining a smaller average area (km²) and a higher total population.

Comparing Figures 21 and 23, a spatial correlation can be observed between high population density municipalities concentrated in the central basin, namely Gustavo A. Madero, Nezahualcóyotl and Venustiano Carranza, and buildings that experienced structural damage or collapse during the 2017 earthquake, delineating the western intersection between the transition and lake micro zones.

Tables 9 and 10 display the estimated warning time per municipality following a displacement from the SC fault. The trajectory is based on the ~19 second warning from the P to S wave reception interval at seismic stations in the Basin of Mexico and the ~120km distance from the epicentre at the Puebla – Morelos State intersection in 2017. Considering all 37 municipalities reside within 60km of the SC fault, warning time is projected to range from 1.3-8.8 seconds. This is a ‘best case’ scenario prediction, however, as it corresponds to the maximum distance in each municipality from the lateral fault extension. The SC fault intersects the municipalities of Iztapalapa, Tlalpan and Xochimilco, implying immediate ground motion is also likely in adjoining districts in the City.

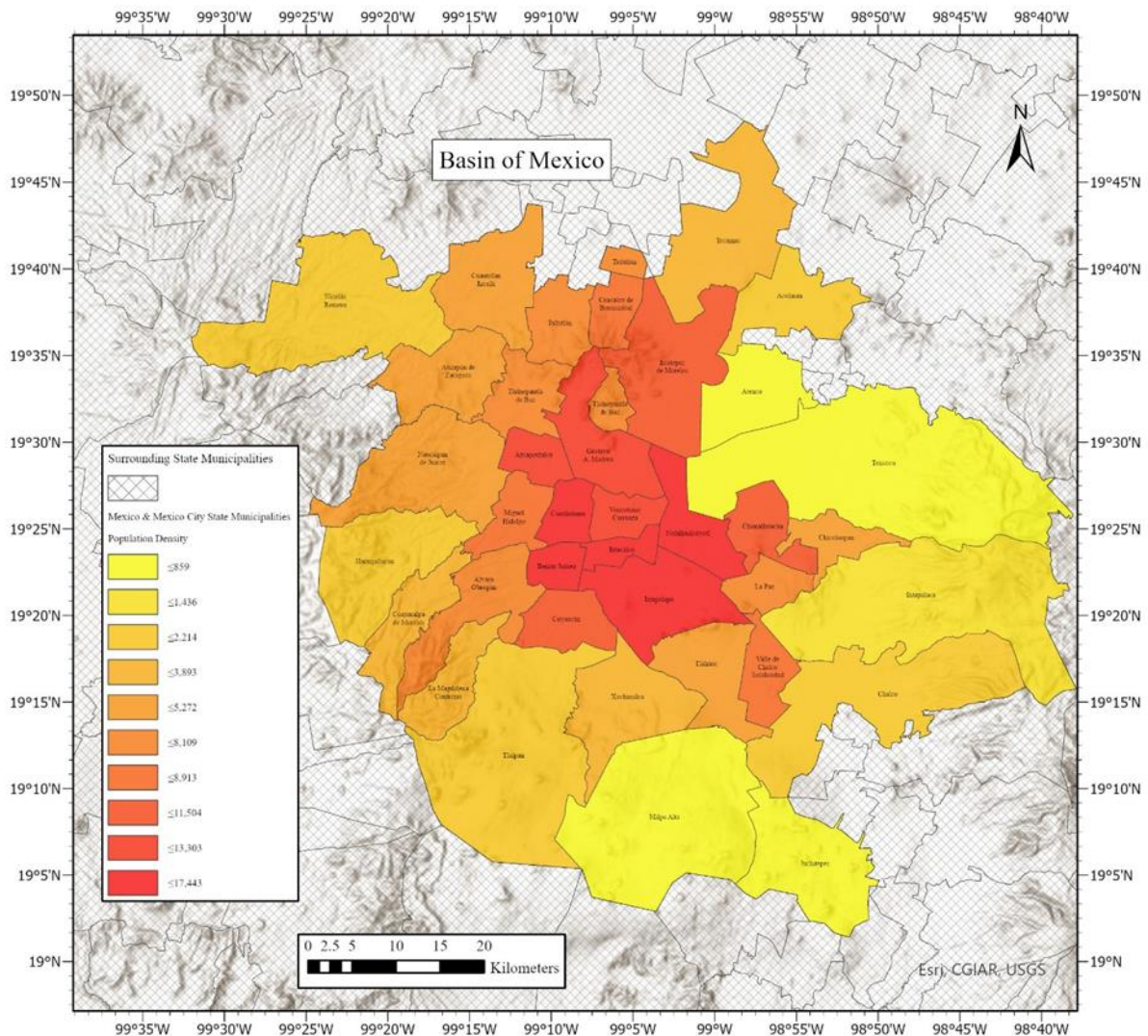


Figure 22. Population Density (/km²) per state municipality in the Basin of Mexico. Created using Arc GIS Pro (v2.5)

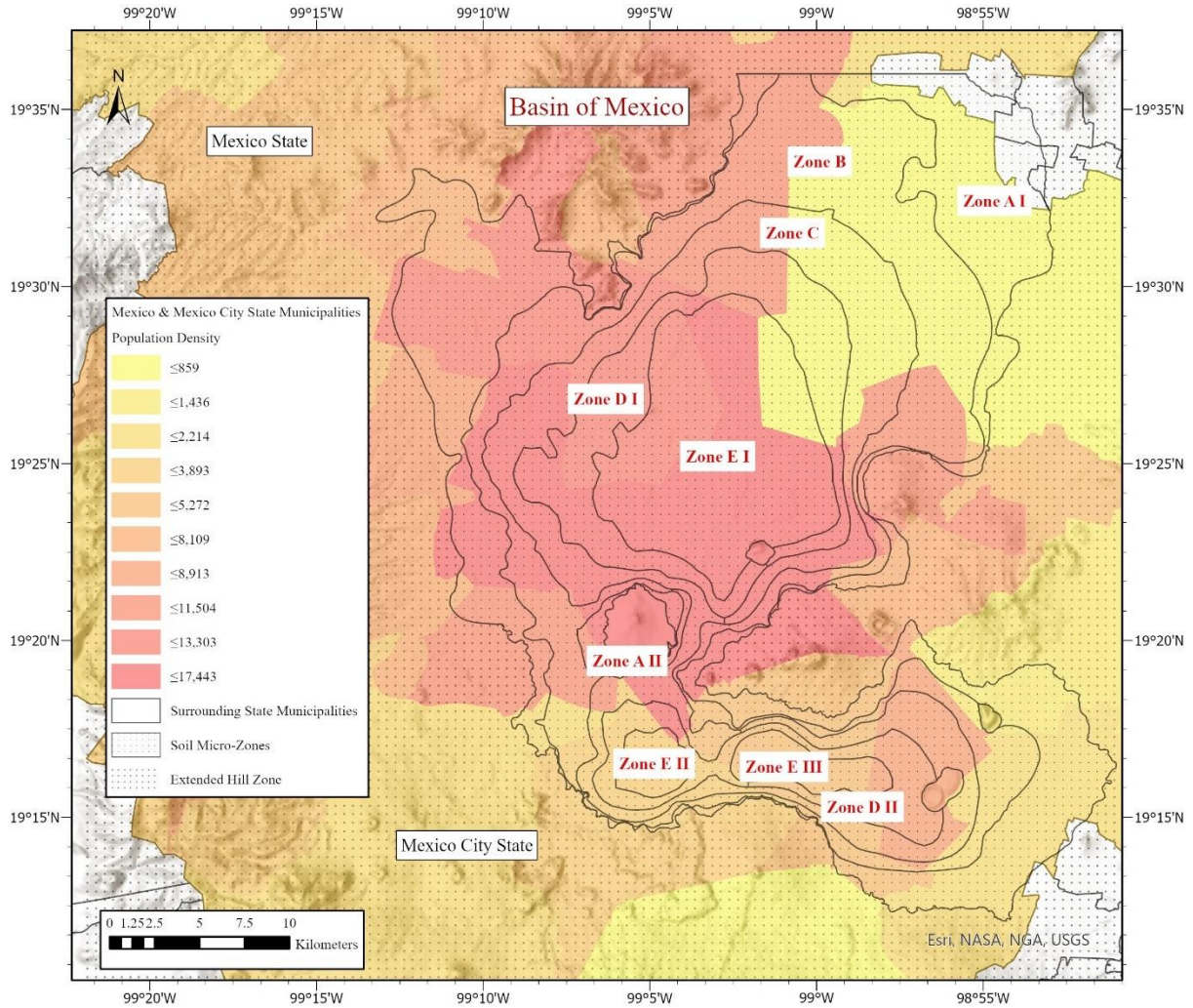


Figure 23. Population Density ($/\text{km}^2$) per state municipality in correspondence with the geotechnical soil microzones (MOC). Created using ArcGIS Pro (v2.5)

Municipality	Maximum distance from the fault extension (km)	Potential Warning Time (s) dependent on location within municipality	State
Álvaro Obregón	≤16.46	≤2.6	Mexico City
Azcapotzalco	≤26.95	≤4.3	Mexico City
Benito Juárez	≤10.10	≤1.6	Mexico City
Coyoacán	≤10.18	≤1.6	Mexico City
Cuajimalpa de Morelos	≤18.81	≤3.0	Mexico City
Cuauhtémoc	≤19.70	≤3.1	Mexico City
Gustavo A. Madero	≤31.60	≤5.0	Mexico City
Iztacalco	≤12.74	≤2.0	Mexico City
Iztapalapa	≤10.96 (Intersected)	≤1.7	Mexico City
La Magdalena Contreras	≤11.03	≤1.8	Mexico City
Miguel Hidalgo	≤22.92	≤3.6	Mexico City
Milpa Alta	≤27.13	≤4.3	Mexico City
Tláhuac	≤16.06	≤2.5	Mexico City
Tlalpan	≤17.67 (Intersected)	≤2.8	Mexico City
Venustiano Carranza	≤17.74	≤2.8	Mexico City
Xochimilco	≤12.13 (Intersected)	≤1.9	Mexico City

Table 9. Potential warning time (s) for Mexico City State municipalities following a displacement, calculated using the maximum distance from the nearest SC fault section (km) with seismic alert records from the 2017 Puebla/Morelos earthquake (SASMEX).

Municipality	Maximum distance from the fault section (km)	Potential Warning Time (s) dependent on location within municipality	State
Acolman	≤43.71	≤6.9	Mexico
Atenco	≤33.23	≤5.3	Mexico
Atizapán de Zaragoza	≤29.5	≤4.7	Mexico
Chalco	≤39.25	≤6.2	Mexico
Chicoloapan	≤28.51	≤4.5	Mexico
Chimalhuacán	≤11.35	≤1.8	Mexico
Coacalco de Berriozábal	≤38.88	≤6.2	Mexico
Cuautitlán Izcalli	≤33.27	≤5.3	Mexico
Ecatepec de Morelos	≤19.02	≤3.0	Mexico
Huixquilucan	≤26.99	≤4.3	Mexico
Ixtapaluca	≤10.55	≤1.7	Mexico
Juchitepec	≤37.86	≤6.0	Mexico
La Paz	≤17.59	≤2.8	Mexico
Naucalpan de Juárez	≤18.76	≤3.0	Mexico
Nezahualcóyotl	≤8.24	≤1.3	Mexico
Nicolás Romero	≤55.89	≤8.8	Mexico
Tecámac	≤55.16	≤8.7	Mexico
Texcoco	≤45.47	≤7.2	Mexico
Tlalnepantla de Baz	≤23.47	≤3.7	Mexico
Tultitlán	≤41.46	≤6.6	Mexico
Valle de Chalco Solidaridad	≤15.60	≤2.5	Mexico

Table 10. Potential warning time (s) for Mexico State municipalities following a displacement, calculated using the maximum distance from the nearest SC fault section (km) with seismic alert records from the 2017 Puebla/Morelos earthquake (SASMEX).

Based on the latest statistical records (National Survey of Demographic Dynamics 2018) from INEGI, Figures 24 and 25 show the demographic breakdown directly corresponding to the soil microzonation thus displaying the spatial relationship between population distribution and potential amplification exposure per soil zone. Following Table 11, the hard rock zone (Zone A) has a population of 2,079,056 in an area of 271km². This gives the lowest population density per zone of 7,672 people per km². The transition zone (Zone B) has 1,999,445 inhabitants, 4% less than the rock zone, however the 231km² area results in a population density almost 12% higher (982 per km²) at 8,656 people per km². The lake zone encompasses seismic zones C, D and E covering a total area of 444km² with 4,735,834 inhabitants. This gives an average population density (Zones C, D and E) of 10,666 people per km², 2,010 per km² higher than the transition zone and 2,994 per km² higher than the rock zone.

Seismic Zone	Population	Seismic Zone Area (km²)	Population Density (per km²)
A	2,079,056	271	7,672
B	1,999,445	231	8,656
C	1,646,337	164	10,039
D	1,041,693	125	8,334
E	2,047,804	155	13,212

Table 11. Seismic zone population density (per km²). Seismic zones colour coded based on different soil compositions. Density (per km²) and Area (km²) have been rounded to whole numbers (Population data from INEGI; Spatial data from Mexican National Atlas of Risk).

Seismic Zone	Households	Seismic Zone Area (km²)	Household Density (per km²)
A	590,001	271	2,177
B	558,156	231	2,416
C	465,285	164	2,837
D	294,574	125	2,357
E	586,434	155	3,783

Table 12. Seismic zone household density (per km²). Density (per km²) and Area (km) have been rounded to whole numbers (data from INEGI and the Mexican National Atlas of Risk).

Population density increases by ~28% as you move from the hard rock zone (7,672 people per km²) to the lake zone (10,666 people per km²) (Table 11). Household density follows a similar trend (Table 12). There is a 10% increase in household density between the rock zone (2,177 households per km²) and the transition zone (2,416 households per km²). Accounting for seismic zones C, D and E, the average household density in the lake zone increases by a further 19% to 2,992 households per km². The range in household density between the rock and lake zone is 815 households per km² (~37%).

Despite the 444km² area being at least 64% larger than the adjoining seismic zones (Figures 25), the extensive ~4.7 million population and compact neighbourhood style residential network in the lake zone has culminated the largest population and household density per km².

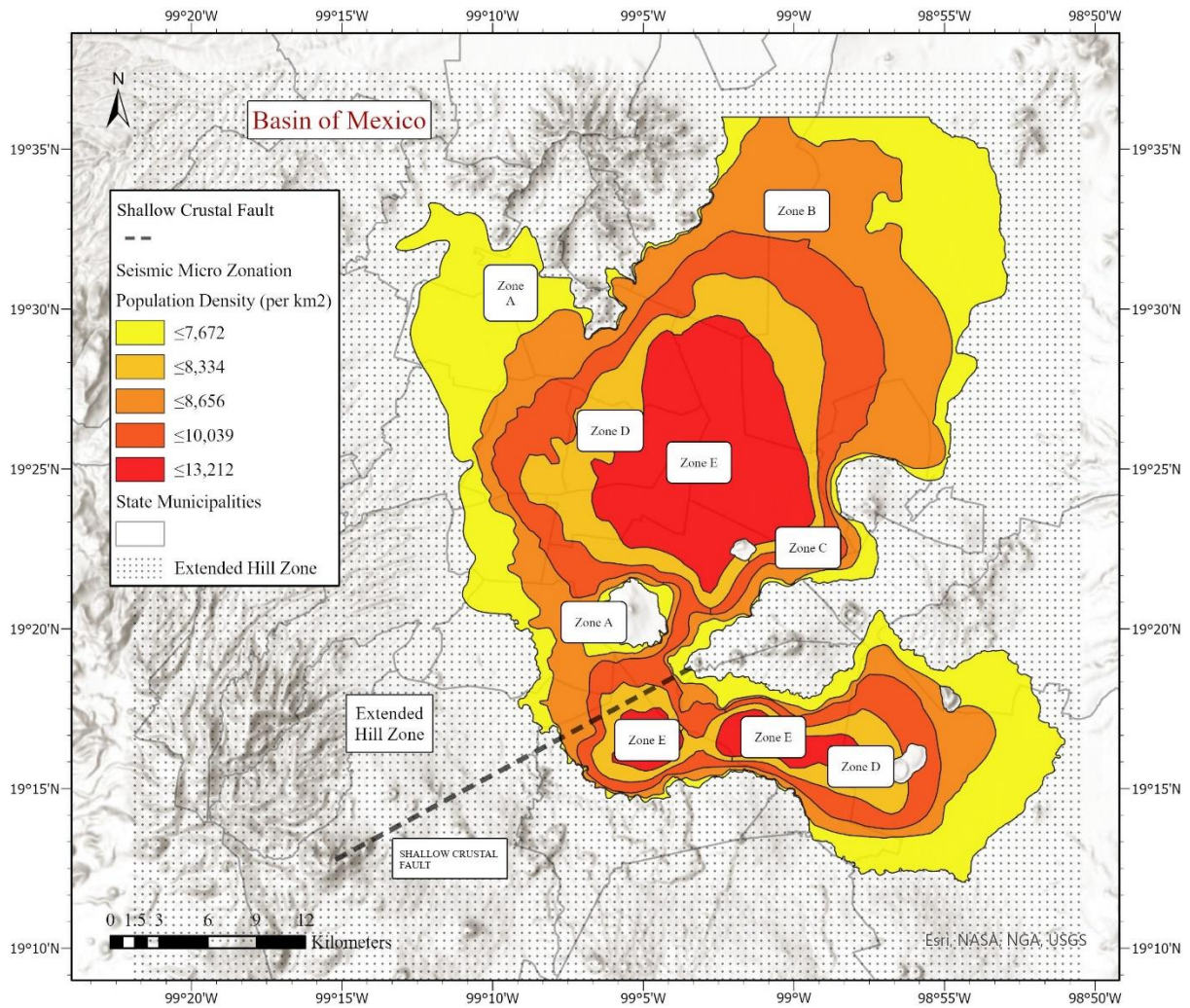


Figure 24. Population density (/km²) per soil microzone (MOC) in the Basin of Mexico. Created using ArcGIS Pro (v2.5).

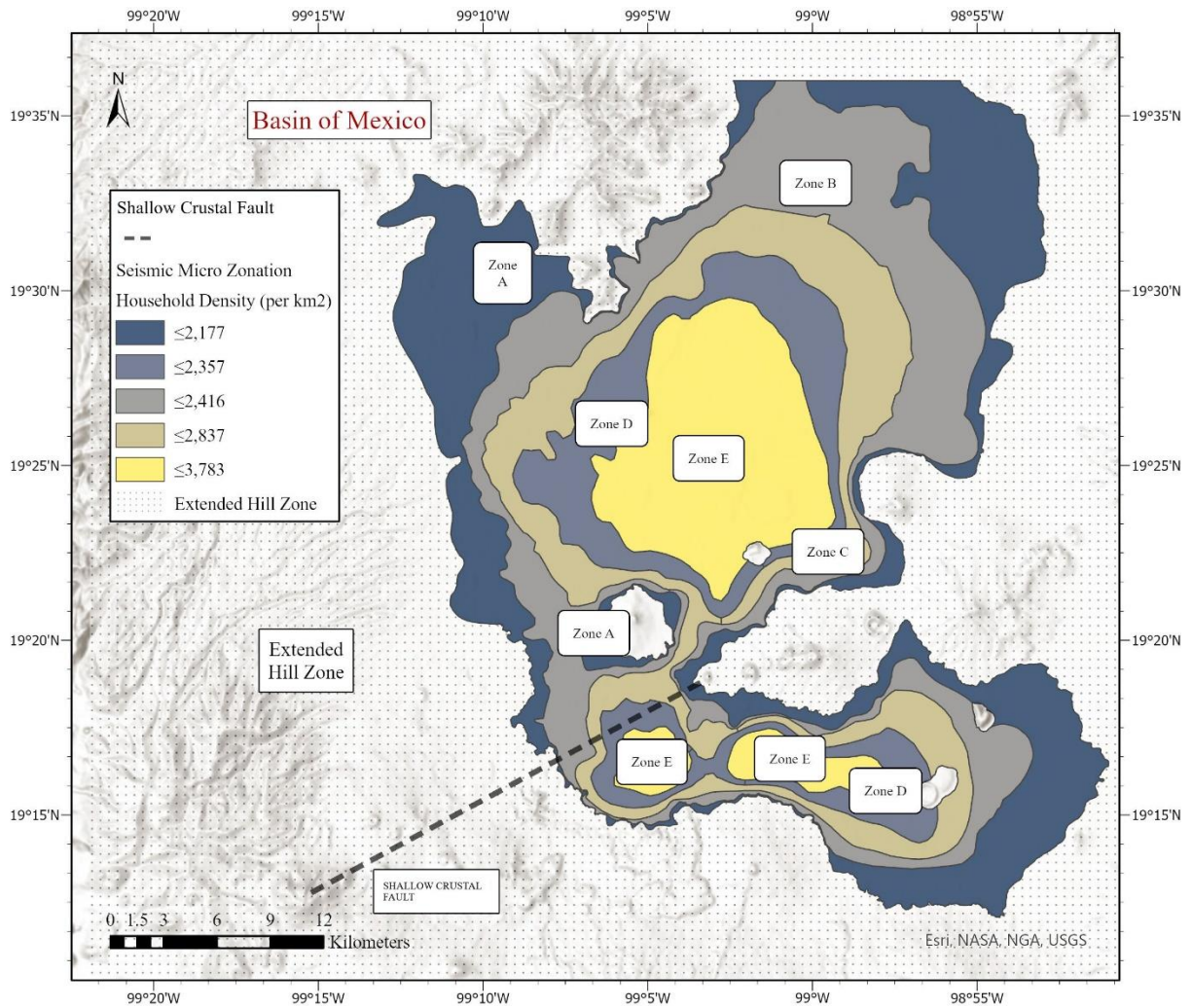


Figure 25. Household Density (/km²) per soil microzone (MOC) in the Basin of Mexico. Created using ArcGIS Pro (v2.5)

5 Discussion

5.1 Quantification of the shallow crustal fault

Recently, patterns of regional subsidence have become prominent in the interpretation of the southern region of the Basin of Mexico (Figuroa-Miranda et al, 2018). Based on comprehensive land subsidence investigations (Gayol, 1925; Cabral-Cano et al, 2008; Osmanoglu et al, 2011; Holzer, 1984), spatial subsidence in Mexico has been classified as either ‘Mexico City Subsidence Type’ (MCST) or ‘Structurally-Controlled Differential Subsidence’ (SCDS). MCST is generally confined to the ancient lake zone (Figure 12) and is the most documented form of subsidence in the Basin, referring to concentric spatial sinking ensuing the consolidation of the highly compressible lacustrine clays embodied in the basins aquifer system (Osmanoglu et al, 2011). Cabral-Cano et al (2008) recognised that recent pressure loss in the lacustrine aquitard system, inducing MCST, was directly linked to the over-exploitation of groundwater beneath Lake Texcoco (water table lowering at a rate of 0.1-1.5m/yr) following the accelerated population growth ($\approx 400\%$) and urban expansion in Mexico City from 1950 to the present day. Concave surface faults are common successive formations associated with MCST, forming along the concentric delineation of the subsiding region (Figuroa-Miranda et al, 2018). In Figure 13 both SC fault orientations can be observed intersecting the lacustrine zone in the central region of the Basin of Mexico. The NE-SW $\approx 23.7\text{km}$ lateral extension away from the point of intersection towards the Sierra de Las Cruces and Sierra Chichinautzin, however, indicates that the SC fault is not a concentric formation nor is it limited by the circumference of previously documented subsidence. It is therefore unlikely that the SC fault is a product of spatial MCST.

SCDS typically relates to graben structures in the basement containing lacustrine sediment. The orientation of the controlling tectonic system dictates the directional alignment of gradual subsidence following groundwater extraction (Pacheco-Martínez et al, 2013; Trujillo-Candelaria, 1985) and can often result in the formation of earth fissures that follow the fault plane direction, evolving into surface faults depending on the bedrock configuration (Avila-Olivera et al, 2008). A good example was presented by Loza-Aguirre et al (2008). Incidents of SCDS were examined in Mesa Central Mexico,

discovering that ground failures in Aguascalientes shared the same NE-SW orientation of the adjacent Aguascalientes Graben. Cabral-Cano et al (2008) further explains that subsidence induced faults generally develop in dated deposits of Quaternary volcanoes and/or in older volcanic structures. Given the principal geological features of SCDS and the matching geological setting of the study area location in the southern region of Basin of Mexico, two direct correlations can be made. (1) The proposed orientations of the SC fault (Georeferenced 23.9km; Linear seismic trend 23.5km) replicate the NNE-SSW directional alignment of the adjacent fault planes from the Santa Catarina Graben (Figure 12); (2) Both orientations from Cerro del Ajusco (19.211006°, -99.257384°) to Cerro Yuhualixqui (19.315987°, -99.052684°), and Xitle volcano (19.256981°, -99.223175°) to Iztacalco (19.404973°, -99.067334°), traverse Quaternary Pliocene-Holocene volcanics ranging from older ~1.9 Ma deposits in the Sierra de Las Cruces (Arce et al, 2013) to ~0.025 Ma deposits in the Sierra Santa Catarina Range (Lugo-Hubp et al, 1994). If the formation of the proposed SC fault was a consequence of and/or influenced by subsidence, it is likely to be attributed to a gradual fault evolution from a pre-existing fault plane associated with SCDS (Figuroa-Miranda et al, 2018). The Santa Catarina Graben has the most credible tectonic structure given the ~1.1km proximity, parallel directional fault alignment (Figure 12) and Quaternary geology.

Following a comprehensive analysis of the damage extent in the Basin of Mexico from the 2017 Puebla-Morelos earthquake, Alberto et al (2018) found that regional subsidence in the south of the Basin, namely in Xochimilco, Tlahuac and Chalco, was worsened by the ground motion. Preceding ground water extraction has consolidated the soft-clay soils in this region (Figuroa-Miranda et al, 2018). This change to the dynamic soil properties increases the effective stresses, and subsequently the fracture vulnerability (Alberto et al, 2018), causing extensive ground failure, witnessed for example, on walkways adjacent to the Zacapa Canal (Figure 19) in Xochimilco. This extensive stress regime adds to an already increasing sinking capacity caused by the accumulation of compressible deposits during basins formation processes (Garcia-Palomo et al, 2000). In the southern region of the Basin of Mexico the increase in effective stress may also give substance to the relationship between the low-magnitude seismic events located along the 23.5km linear trend (Figure 13) and the preceding tectonic earthquakes

observed in Table 4. Pacheco-Martínez et al (2013) explains how active faults generate maximum stress areas capable of triggering low-intensity earthquakes consistent with small-scale seismic movements at shallow depths. High-frequency seismic swarming relating to subsurface magmatic movement is also common in this region of the Basin. The clustering of the events, however, is usually contained within weeks or months not in an incremental time-period like the seismic events from 1974 to 2020, which implies seismic swarming associated with volcanism is highly unlikely (Zobin et al, 2002). In accordance with Pacheco-Martínez et al (2013) and Alberto et al (2018), it is possible that the trending low-magnitude seismic events in the south of the Basin are derivatives of tectonic displacements, triggered by the exacerbation of regional subsidence and the existence of the SC fault in an area of maximum horizontal stress. This rationalises the occurrence of events in a linear arrangement and could explain why they closely follow larger national earthquakes. This also substantiates the 23.5km linear seismic event trend from Xitle volcano to Iztacalco as the more likely orientation of the SC fault.

Suter et al (1992) suggested that the entire TMVB region is tectonically active and in the process of a gravitational collapse because of the isostatically compensated surface loads related to the high average elevation. On a regional scale, this is supported by the negative Bouguer gravity anomalies (-100 to -250 mGals) observed in Figure 6, highlighting a vertical density contrast between the bounded volcanic ranges and an intrusive low-density mantle layer beneath the Basin of Mexico. The main tectonic fault systems in the TMVB align in an E-W orientation parallel to the TMVB axis. Four of these tectonic structures surround the Basin of Mexico: The Sierra Chichinautzin in the south, the Perales semi-graben to the west, the Acambay Graben to the north-west, and the Nopala Graben to the north (Márquez et al, 1999). These structures form a 150km wide zone of N-S extensional forces, as well as forming dynamic N-S conditions for each individual tectonic structure. The Basin of Mexico is central to this region and is therefore subject to the dynamic scheme of N-S extensional forces, vertical density contrasts that are part of a wider gravitational collapse, and an increasing effective stress regime from accelerated changes to its dynamic soil properties (Szyrkaruk et al, 2004). It is possible that in this abnormal state of critical stress, further exacerbation e.g., with ground motion from the 1912 M_w 6.9 Acambay earthquake, has

exceeded the maximum stress capacity of the Basin, creating the vulnerable conditions necessary to initiate the formation process of a SC fault (Suter et al, 2001).

5.2 Implications from a projected displacement

In accordance with the visual observations from this research project in the south of the Basin (Figures 16-20) and Alberto et al (2018) comparative study investigating the building efficiency in 2017 after the comprehensive retrofitting procedure following the 1985 Michoacán earthquake, most of the collapsed or severely damaged buildings during the 2017 Puebla-Morelos earthquake were either pre-1985 designs that failed to receive seismic rehabilitation or of an inadequate structural design with illegitimate modifications that left the structures more vulnerable to prospective ground motion. The structural damage was concentrated in the western region of seismic microzones B and C (Figure 21), similar to 1985, where the transition to dynamic soft soil deposits generates the maximum relative amplification (Cruz-Atienza et al, 2016) and coincides with some of the highest population densities per municipality in the Basin (Figures 22 and 23), namely Iztacalco (17,444 per km²), Nezahualcóyotl (17,323 per km²), Cuauhtémoc (16,745 per km²) and Benito Juárez (16,200 per km²). Despite the damage distribution, retrofitted buildings, which included the majority of commercial, residential and hospitality structures (Galvis, 2017) performed well, remaining structurally sound in line with the revised 2004 structural design code.

The location of a SC fault in the Basin of Mexico and the projected maximum $M_s 6.7$ output from full length fault rupture, forecasts a potential scenario that could have severe repercussions on the socio-economic stability of Mexico City and neighbouring municipalities. A displacement in the Basin of Mexico would place the epicentre ≈ 120 km closer than any previously documented seismic event of equal magnitude (Poursartip et al, 2017). In terms of radiated seismic energy (E_s) (Singh, 1994), a $M_s 6.7$ event wouldn't be as strong as the recent $M_w 7.1$ earthquake experienced in 2017, however, given the epicentral location within the basin, the reciprocated damage will likely be more extreme. Based on the proximity to the fault rupture area, the population and infrastructure in the Basin would likely be exposed to near source MM10+ seismic intensities (MMS) (Dowrick, 1996). As observed during the

Puebla-Morelos earthquake (Alberto et al, 2018), the resonance will be enhanced by the ground conditions in the lacustrine zone which encompasses the Basin's highest population and household densities (Figures 24 and 25). Ortega (2005) studied the Basins local magnitude scale to improve detection sensitivity. The study identified that a revision of the scaling was necessary to prevent the underestimation of the complex attenuation differences across the Basin's geometry, causing a suppression of the magnitude characterisation. This suggests that the perceived magnitude in the Basin may not reflect the intensified reality for the localities in areas of increased amplification.

Given the site conditions and basin characteristics, the construction performance during the period of maximum earthquake intensity will depend on the function of certain parameters, including: the building (retrofitting) mechanisms, the proximity to other buildings, the location in regard to the basin geometry, peak ground acceleration and the amplification factor (Semblat et al, 2008). In this scenario the efficiency of retrofitting may be even more significant in maintaining public safety. With the epicentre located in the Basin, the P- and S-wave inception times would be synchronised with no interval difference, meaning the current Seismic Alert System would be insufficient in providing early warning (Table 9 and 10) and the population would experience strong ground-motion at the sound of the warning sirens, if not before. Considering the potential path propagation of a $M_s 6.7$ earthquake originating from within the Basin, a repetition of the socio-economic impact suffered from the 2017 Puebla-Morelos earthquake would be a best-case scenario. The implementation of stronger mitigation measures will be required if an active SC fault exists in the Basin of Mexico.

5.3 Limitations and future actions

The COVID-19 pandemic has been the foremost limitation to this study. The final three weeks of research in Mexico City were aborted during the prime data collection period. This meant that remote access was required to obtain some secondary data. With CENAPRED being at the forefront of Mexico's disaster mitigation, communication during the pandemic has understandably been difficult, however, limited access to the specific data resources stagnated the progress of the initial Master's proposal and forced a complete restructure of the research. The new direction was therefore significantly time-pressured, restricted to a 9-month timeframe. The future scalability of this study is determined by the availability of funding to access and handle the specific geophysical equipment and exposure to an extended timeframe in Mexico City.

Interpreting the disproportional large scale on Mooser (2018) 2D stereographic illustration for the proposed faulting relied on a limited number of recognisable geographical features which increases the possibility for initial georeferencing errors. This may be of little significance given the spatial accuracy of the GPS on the SSN observatory broadband seismometers and the subsequent influence of the low-magnitude seismic events in substantiating the location of the proposed SC fault, however, additional quantification techniques are required to obtain a conclusive understanding of the fault's existence and, if so, the extent of its emplacement. Singh (1980) identified that defining a fault's aspect ratio (length x width) or surface area, provides a more reliable estimation of a maximum magnitude output or fault rupture area. To improve the accuracy of the maximum magnitude output projection in this study, further examination of the seismic events from the established linear seismic trend in the Basin. An interdisciplinary investigation, similar to Arce et al (2019), would be advantageous, combining geophysical survey data like seismic refraction or more detailed gravimetry data, with a real-time field transect to analyse the proposed fault location for scarps or ground deformation. Conceptual models of the subsurface structure could then be created with GPR and strategic deep wells to better define the stratigraphy.

With a greater understanding of the fault schematics, a numerical source simulation would be a good course of action, using similar probabilistic methodology to the scheme of simulations by Cruz-Arguelles et al (2020) for the M_w 7.1 2017 Puebla-Morelos earthquake, to project the output from a SC fault displacement in the extended Basin, considering both the soil stratification and dynamic site properties. The trajectory of seismic amplification through the seismic microzones will provide an exploratory Deterministic Seismic Hazard Analysis (DSHA) for the population and infrastructure in each locality. It is important to note that seismic sources studied in current simulations are only located at intermediate or extended distances from the target area (Cruz-Arguelles et al, 2020), therefore a new theoretical source model would need to be created simulating the immediate path propagation through the Basin.

6 Conclusions

This study aimed to quantify a potential Shallow Crustal fault in the Basin of Mexico using Moosers (2018) 2D stereographic model and evaluate the effects of a projected fault displacement on the population and infrastructure using probabilistic and deterministic methodology.

The 23.5km directional alignment, between Xitle volcano and Iztacalco, of low-magnitude seismic events from 1974 to 2020 and their incremental occurrence following national earthquakes, substantiates the possible existence of an active SC fault in an area of critical stress experiencing extreme N-S extensional and negative gravitational forces. It is likely that Structurally Controlled Differential Subsidence (SCDS) associated with the rapid 20th century increase in anthropogenic activity in the Basin of Mexico, and strong-ground motion from major national earthquakes, has accelerated its formation sequence by exceeding the basements maximum stress capacity. The unique geotechnical conditions present in the basement justify it as a legitimate formation environment, however, to obtain a conclusive understanding of the fault's emplacement, additional quantification techniques will be required to support the geophysical correlations identified in this study.

The projected maximum $M_s 6.7$ output from a shallow crustal fault displacement originating from within the Basin, forecasts a potential scenario that is likely to produce more severe socio-economic implications to those experienced during the 2017 $M_w 7.1$ Puebla-Morelos earthquake, with insufficient ground-motion warning time for the population in Mexico City and its neighbouring municipalities. The successful performance in 2017 of buildings re-evaluated and retrofitted after the 1985 Michoacán earthquake, reiterates the necessity for the continual adaptation of structural evaluations to the evolution of the basement and prompts the consideration to implement stronger mitigation measures to maintain construction performance during the periods of maximum earthquake intensity.

7 References

- Alberto, Y., Otsubo, M., Kyokawa, H., Kiyota, T. and Towhata, I. (2018). Reconnaissance of the 2017 Puebla, Mexico earthquake. *Soils and foundations*, 58(5), 1073-1092.
- Alcocer, S.M. and Castaño, V.M., (2008). Evolution of codes for structural design in Mexico. *Structural Survey*.
- Aguilar, J., Juarez, H., Ortega, R. and Iglesias, J., (1989). The Mexico Earthquake of September 19, 1985—Statistics of damage and of retrofitting techniques in reinforced concrete buildings affected by the 1985 earthquake. *Earthquake Spectra*, 5(1), pp.145-151.
- Arce, J.L., Layer, P.W., Macías, J.L., Morales-Casique, E., García-Palomo, A., Jiménez-Domínguez, F.J., Benowitz, J. and Vásquez-Serrano, A., (2019). Geology and stratigraphy of the Mexico basin (Mexico City), central Trans-Mexican volcanic Belt. *Journal of Maps*, 15(2), pp.320-332.
- Arce, J.L., Layer, P., Martínez, I., Salinas, J.I., Macías-Romo, M.D.C., Morales-Casique, E., Benowitz, J., Escolero, O. and Lenhardt, N., (2015). Geología y estratigrafía del pozo profundo San Lorenzo Tezonco y de sus alrededores, sur de la Cuenca de México. *Boletín de la Sociedad Geológica Mexicana*, 67(2), pp.123-143.
- Arce, J.L., Layer, P.W., Morales-Casique, E., Benowitz, J.A., Rangel, E. and Escolero, O., (2013). New constraints on the subsurface geology of the Mexico City Basin: The San Lorenzo Tezonco deep well, on the basis of $^{40}\text{Ar}/^{39}\text{Ar}$ geochronology and whole-rock chemistry. *Journal of Volcanology and Geothermal Research*, 266, pp.34-49.
- Avila-Olivera, J.A. and Garduño-Monroy, V.H., (2008). A GPR study of subsidence-creep-fault processes in Morelia, Michoacán, Mexico. *Engineering Geology*, 100(1-2), pp.69-81.
- Blakely, R.J., Brocher, T.M. and Wells, R.E., (2005). Subduction-zone magnetic anomalies and implications for hydrated forearc mantle. *Geology*, 33(6), pp.445-448.
- Bravo, H., Ponce, L., Suárez, G., Zúñiga, R., (1988). El Potencial Sísmico de México, in Estudios sobre Sismicidad en el Valle de México, D.F./UNESCO, 1ª. Parte, Capítulo I.
- Bray, J.D., Stewart, J.P., Baturay, M.B., Durgunoglu, T., Onalp, A., Sancio, R.B., Stewart, J.P., Ural, D., Ansal, A., Bardet, J.B. and Barka, A., (2000). Damage patterns and foundation performance in Adapazari. *Earthquake Spectra*, 16(S1), pp.163-189.

- Cabral-Cano, E., Dixon, T.H., Miralles-Wilhelm, F., Díaz-Molina, O., Sánchez-Zamora, O. and Carande, R.E., (2008). Space geodetic imaging of rapid ground subsidence in Mexico City. *Geological Society of America Bulletin*, 120(11-12), pp.1556-1566.
- Campos-Enríquez, J.O., Lermo-Samaniego, J.F., Antayhua-Vera, Y.T., Chavacán, M. and Ramón-Márquez, V.M., (2015). The Aztlán Fault System: control on the emplacement of the Chichinautzin Range volcanism, southern Mexico Basin, Mexico. Seismic and gravity characterization. *Boletín de la Sociedad Geológica Mexicana*, 67(2), pp.315-335.
- Carreon-Freyre, D., Gutierrez-Calderon, R.I., Cerca, M. and Alcantara-Duran, C.F., (2020). Factors that condition physical vulnerability to ground fracturing in Mexico City. *Proceedings of the International Association of Hydrological Sciences*, 382, pp.571-576.
- Chavez-Garcia, F. J. and Salazar, L. (2002). Strong Motion in Central Mexico: A Model Based on Data.
- Cruz-Arguelles, J.D., Jaimes, M.A. and Arredondo-Vélez, C.A., (2020). Simulation of strong ground motions modified by attenuation effects under specific soil conditions: modelling the 2017 Puebla, Mexico (Mw 7.1) earthquake. *Journal of Seismology*, 24, pp.495-509.
- Cruz-Atienza, V. M., J. Tago, J. D. Sanabria-Gómez, E. Chaljub, V. Etienne, J. Virieux and L. Quintanar. (2016). Long Duration of Ground Motion in the Paradigmatic Valley of Mexico. *Nature - Scientific Reports*, 6, 38807; doi:10.1038/srep38807
- Cruz-Jiménez, H., Chávez-García, F. J., Furumura, T., and Mai, M. . (2011). Attenuation of Ground Motion Perpendicular to the Mexican Subduction Zone. *4th IASPEI/ IAEE International Symposium*.
- Davis, G.H., Reynolds, S.J. and Kluth, C.F., (2011). *Structural geology of rocks and regions*. John Wiley & Sons.
- De Cserna, Z. (1987). Geological structure, gravimetry, seismicity and regional neotectonic relationships of the Mexico Basin . *National Autonomous University of Mexico, Institute of Geology*, 104.
- Dowrick, D.J., (1996). The Modified Mercalli earthquake intensity scale. *Bulletin of the New Zealand Society for Earthquake Engineering*, 29(2), pp.92-106.
- Ekström, G., and M. Nettles, (1997). Calibration of the HGLP seismograph network and centroid-moment tensor analysis of significant earthquakes of 1976, *Phys. Earth Planet. Inter.*, 101, 219-243, doi:10.1016/S0031-9201(97)00002-2
- Ekström, M. Nettles, A.M. Dziewoński. (2012). The global CMT project 2004–2010: Centroid-moment tensors for 13,017 earthquakes, *Physics of the Earth and Planetary Interiors*, Volumes 200–201, Pages 1-9.

- Estêvão, J. and Esteves, C., (2020). Nonlinear Seismic Analysis of Existing RC School Buildings: The “P3” School Typology. *Buildings*, 10(11), p.210.
- Faccioli, E. and Resendiz, D., (1976). Soil dynamics: behaviour including liquefaction. In *Developments in geotechnical engineering* (Vol. 15, pp. 71-139). Elsevier.
- Ferrari, L., Orozco-Esquivel, T., Manea, V. and Manea, M., (2012). The dynamic history of the Trans-Mexican Volcanic Belt and the Mexico subduction zone. *Tectonophysics*, 522, pp.122-149.
- Figueroa-Miranda, S., Tuxpan-Vargas, J., Ramos-Leal, J.A., Hernández-Madrigal, V.M. and Villaseñor-Reyes, C.I., (2018). Land subsidence by groundwater over-exploitation from aquifers in tectonic valleys of Central Mexico: A review. *Engineering Geology*, 246, pp.91-106.
- Fitz-Diaz, E., Hudleston, P., Siebenaller, L., Kirschner, D., Camprubí, A., Tolson, G. and Puig, T.P. (2011). Insights into fluid flow and water-rock interaction during deformation of carbonate sequences in the Mexican fold-thrust belt. *Journal of Structural Geology*, 33(8), 1237-1253.
- Franke, K.W., Candia, G., Mayoral, J.M., Wood, C.M., Montgomery, J., Hutchinson, T. and Morales-Velez, A.C., (2019). Observed building damage patterns and foundation performance in Mexico City following the 2017 M7. 1 Puebla-Mexico City earthquake. *Soil Dynamics and Earthquake Engineering*, 125, p.105708.
- Galvis, F., Miranda, E., Heresi, P., Dávalos, H. and Silos, J.R., (2017). Preliminary statistics of collapsed buildings in Mexico City in the September 19, 2017 Puebla-Morelos Earthquake. *John A. Blume Earthquake Engineering Centre and Department of Civil and Environmental Engineering Stanford University*, <http://learningfromearthquakes.org>.
- García Acosta, V. and Suárez Reynoso, G., (1996). Los sismos en la historia de México. *Universidad Nacional Autónoma de México*.
- García-Palomo, A., Macías, J.L., Arce, J.L., Capra, L., Garduño, V.H. and Espíndola, J.M. (2002). Geology of the Nevado de Toluca volcano and surrounding areas. *Geological Society of America*.
- García-Palomo, A., Macías, J.L. and Garduño, V.H. (2000). Miocene to recent structural evolution of the Nevado de Toluca volcano region, Central Mexico. *Tectonophysics*, 318(1-4), 281-302.
- García-Palomo, A., Luis Macías, J., Jiménez, A., Tolson, G., Mena, M., Sánchez-Núñez, J.M., Luis Arce, J., Layer, P.W., Ángel Santoyo, M., Lermo-Samaniego, J. (2018). NW-SE Pliocene-Quaternary extension in the Apan-Acocolco region, eastern Trans-Mexican Volcanic Belt. *Journal of Volcanology and Geothermal Research*, 349, 240-255.

- García-Palomo, A., Zamorano, J.J., López-Miguel, C., Galván-García, A., Carlos-Valerio, V., Ortega, R. and Macías, J.L. (2008). El arreglo morfoestructural de la Sierra de Las Cruces, México central. *Revista mexicana de ciencias geológicas*, 25(1), 158-178.
- Gayol, R., (1925). *Study of the disturbances that at the bottom of the valley of Mexico has produced the drainage of subsoil waters by the works of the Drain, and rectification of the errors that have resulted in an incorrect interpretation of the observed facts.* Publishing company of Engineering and Architecture.
- Gilbert, F., (1971). Excitation of the normal modes of the Earth by earthquake sources. *Geophysical Journal International*, 22(2), pp.223-226.
- González-Torres, E.A., Morán-Zenteno, D. J., Mori, L., and Martiny, B. M., (2005). Revisión de los últimos eventos magmáticos del Cenozoico del sector norte-central de la Sierra Madre del Sur y su posible conexión con el subsuelo profundo de la Cuenca de Mexico. *Boletín de la Sociedad Geológica Mexicana*, 67(2), 285-297.
- González Torres, E.A., Morán Zenteno, D.J., Mori, L. and Martiny, B.M., (2015). Review of the latest magmatic events of the Cenozoic of the north-central sector of the Sierra Madre del Sur and their possible connection with the deep subsoil of the Basin of Mexico. *Bulletin of the Mexican Geological Society*, 67(2), pp.285-297.
- Hanks, T.C. and Kanamori, H., (1979). A moment magnitude scale. *Journal of Geophysical Research: Solid Earth*, 84(B5), pp.2348-2350..
- Holzer, T.L., (1984). Ground failure induced by ground-water withdrawal from unconsolidated sediment. *Reviews in engineering geology*, 6, pp.67-105.
- Juárez-Camarena, M., Auvinet-Guichard, G. and Méndez-Sánchez, E., (2016). Geotechnical zoning of the México Valley subsoil. *Ingeniería, Investigación y Tecnología*, 17(3), pp.297-308.
- Kostoglodov, V. and Pacheco, J.F., (1999). One hundred years of seismicity in Mexico. *Inst. de Geofísica., Universidad Nacional Autonoma de Mexico (UNAM), Mexico City.*
- Langridge, R.M., Weldon, R.J., Moya, J.C. and Suárez, G. (2000). Paleoseismology of the 1912 Acambay earthquake and the Acambay-Tixmadejé fault, Trans-Mexican volcanic belt. *Journal of Geophysical Research: Solid Earth*, 105, 3019-3037.
- Loza-Aguirre, I., Nieto-Samaniego, A.F., Alaniz-Alvarez, S.A. and Iriondo, A., (2008). Stratigraphic-structural relations at the intersection of the San Luis-Tepehuanes fault system and the graben of Aguascalientes, central Mexico. *Mexican Journal of Geological Sciences*, 25(3), pp.533-548.

- Lozano-García, S., Brown, ET, Ortega, B., Caballero, M., Werne, J., Fawcett, PJ, Schwalb, A., Valero-Garcés, BL, Schnurrenberger, D., Stockhecke, M. and Steinman, B. (2017). Deep drilling in Lake Chalco: technical report. *Bulletin of the Mexican Geological Society*, 69(2), 299-311.
- Lugo-Hubp, J., Mooser, F., Pérez-Vega, A. and Zamorano-Orozco, J., (1994). Geomorphology of the Sierra de Santa Catarina, DF, Mexico. *Mexican Journal of Geological Sciences*, 11(1), pp.43-52.
- MASE (2007): Meso America Subduction Experiment. Caltech. Dataset. doi:10.7909/C3RN35SP.
- Marsal, R., Mazari, M., (1959). *The Subsoil of Mexico City*. (I. of Engineering, ed.) National Autonomous University of Mexico.
- Márquez, A., Verma, S.P., Anguita, F., Oyarzun, R. and Brandle, J.L., (1999). Tectonics and volcanism of Sierra Chichinautzin: extension at the front of the Central Trans-Mexican Volcanic belt. *Journal of Volcanology and Geothermal Research*, 93(1-2), pp.125-150.
- Mooney, W.D. (2015). 1.11 - Crust and Lithospheric Structure - Global Crustal Structure, *Treatise on Geophysics* (Second Edition), Elsevier, Pages 339-390.
- Mooser, F. (1963). Historia tectónica de la Cuenca de México. *Boletín de la Asociación Mexicana de Geólogos Petroleros*, 15(11-12), 239-245.
- Mooser, F., (2018), “Geología del valle de México y otras regiones del país”, Colegio de Ingenieros Civiles de México, CDMX, México.
- Ortega, R. and Quintanar, L., (2005). A Study of the Local Magnitude Scale in the Basin of Mexico: Mutually Consistent Estimates of log A 0 and Ground-Motion Scaling. *Bulletin of the Seismological Society of America*, 95(2), pp.605-613.
- Osmanoğlu, B., Dixon, T.H., Wdowinski, S., Cabral-Cano, E. and Jiang, Y., (2011). Mexico City subsidence observed with persistent scatterer InSAR. *International Journal of Applied Earth Observation and Geoinformation*, 13(1), pp.1-12.
- Ovando-Shelley, E., Ossa, A. and Romo, M.P., (2007). The sinking of Mexico City: Its effects on soil properties and seismic response. *Soil Dynamics and Earthquake Engineering*, 27(4), pp.333-343.
- Pacheco-Martínez, J., Hernandez-Marín, M., Burbey, T.J., González-Cervantes, N., Ortíz-Lozano, J.Á., Zermeño-De-Leon, M.E. and Solís-Pinto, A., (2013). Land subsidence and ground failure associated to groundwater exploitation in the Aguascalientes Valley, México. *Engineering Geology*, 164, pp.172-186.

- Pérez-Campos, X., Kim, Y., Husker, A., Davis, P.M., Clayton, R.W., Iglesias, A., Pacheco, J.F., Singh, S.K., Manea, V.C. and Gurnis, M., (2008). Horizontal subduction and truncation of the Cocos Plate beneath central Mexico. *Geophysical research letters*, 35(18).
- Perez-Cruz, G.A., (1988). Seismological study of reflection of the subsoil of Mexico City. *Seismic reflection study of the Mexico City subsoil*. M in Eng Thesis. DEPFI, UNAM.
- Poursartip, B., Fathi, A., Loukas, F.K. (2017). Seismic wave amplification by topographic features: A parametric study. *Soil Dynamics and Earthquake Engineering*, 92, 503-527
- Rodríguez-Pascua, M.A., Pérez-López, R., Garduño-Monroy, V.H., Perucha, M.A. and Israde-Alcántara, I., (2017). Estimation of the epicentral area of the 1912 Acambay earthquake (M 6.9, Mexico) determined from the earthquake archaeological effects (EAE) and the ESI07 macro seismic scale. *Quaternary International*, 451, pp.74-86.
- Rosenblueth, E., Sánchez-Sesma, F.J., Ordaz, M., and Singh, S. K.,. (1987). Espectros de diseño en el reglamento para construcciones del Distrito Federal. *VII Congreso Nacional de Ingeniería Sísmica, Querétaro, México, 1-17*.
- Sánchez-Sesma, F., Chávez-Pérez, S., Suarez, M., Bravo, M.A. and Pérez-Rocha, L.E. (1988). The Mexico earthquake of September 19, 1985—On the seismic response of the Valley of Mexico. *Earthquake spectra*, 4(3), 569-589.
- Santoyo-Villa, E., Ovando-Shelley, E., Mooser, F., León-Plata, E. (2005). Síntesis geotécnica de la cuenca del Valle de México: México, D.F. *TGC Geotécnica*, 171.
- Semblat, J.F., (2011). Modeling seismic wave propagation and amplification in 1D/2D/3D linear and nonlinear unbounded media. *International Journal of Geomechanics*, 11(6), pp.440-448.
- Semblat, J.F., Kham, M. and Bard, P.Y., (2008). Seismic-wave propagation in alluvial basins and influence of site-city interaction. *Bulletin of the Seismological Society of America*, 98(6), pp.2665-2678.
- Shapiro, N.M., Campillo, M., Paul, A., Singh, S.K., Jongmans, D. and Sanchez-Sesma, F.J., (1997). Surface-wave propagation across the Mexican Volcanic Belt and the origin of the long-period seismic-wave amplification in the Valley of Mexico. *Geophysical Journal International*, 128(1), pp.151-166.
- Siebe, C., Rodríguez-Lara, V., Schaaf, P. and Abrams, M. (2004). Radiocarbon ages of Holocene Pelado, Guespalapa, and Chichinautzin scoria cones, south of Mexico City: implications for archaeology and future hazards. *Bulletin of Volcanology*, 66(3), 203-225.

- Singh, S.K., Bazan, E. and Esteva, L., 1980. Expected earthquake magnitude from a fault. *Bulletin of the Seismological Society of America*, 70(3), pp.903-914.
- Singh, S. K., Mena, E., and Castro, R. (1988). Some Aspects of Source Characteristics of the 19 September 1985 Michoacan Earthquake and Ground Motion Amplification in and Near Mexico City from Strong Motion Data. *Bulletin of the Seismological Society of America*, 78 (2), 451-477.
- Singh, S.K., Yamamoto, J., Havskov, J., Guzman, M., Novelo, D. and Castro, R. (1980). Seismic gap of Michoacan, Mexico. *Geophysical Research Letters*, 7(1), 69-72.
- Singh, S.K. and Ordaz, M., (1993). On the origin of long coda observed in the lake-bed strong-motion records of Mexico City. *Bulletin of the Seismological Society of America*, 83(4), pp.1298-1306.
- Singh, S.K. and Ordaz, M., (1994). Seismic energy release in Mexican subduction zone earthquakes. *Bulletin of the Seismological Society of America*, 84(5), pp.1533-1550.
- Slemmons, D.B. (1982). Determination of design earthquake magnitudes for microzonation. Proceedings of Third International Earthquake Microzonation Conference, v. 1, p, 119—130
- SSN (2021): National Seismological Service, Institute of Geophysics, National Autonomous University of Mexico, Mexico. URL: <http://www.ssn.unam.mx>. DOI: <https://doi.org/10.21766/SSNMX/SN/MX>
- Suárez, G., Novelo, D. and Mansilla, E. (2009). Performance evaluation of the seismic alert system (SAS) in Mexico City: A seismological and a social perspective. *Seismological Research Letters*, 80(5), 707-716.
- Suter, M., Martínez, M.L., Legorreta, O.Q. and Martínez, M.C., (2001). Quaternary intra-arc extension in the central Trans-Mexican volcanic belt. *Geological Society of America Bulletin*, 113(6), pp.693-703.
- Suter, M., Quintero, O. and Johnson, C.A., (1992). Active faults and state of stress in the central part of the Trans-Mexican Volcanic Belt, Mexico 1. The Venta de Bravo Fault. *Journal of Geophysical Research: Solid Earth*, 97(B8), pp.11983-11993.
- Szynkaruk, E., Graduño-Monroy, V.H. and Bocco, G. (2004). Active fault systems and tectono-topographic configuration of the central Trans-Mexican Volcanic Belt. *Geomorphology*, 61(1-2), 111-126.
- Tena-Colunga, A., (1999). International Seismic Zone Tabulation Proposed by the 1997 UBC Code: Observations for Mexico. *Earthquake Spectra*, 15(2), pp.331-360.

- Tena-Colunga, A., Mena-Hernández, U., Pérez-Rocha, L., Avilés, J., Ordaz, M. and Vilar, J., (2009). Updated seismic design guidelines for model building code of Mexico. *Earthquake Spectra*, 25(4), pp.869-898.
- Trujillo-Candelaria, J.A., (1985). Subsidence of land in the city of Celaya, Gto. *Meeting on Regional Settlements: Mexico, DF, Mexican Soil Society, Mexican Geohydrologic Association*, pp.1-2.
- Urbina, F. and Camacho, H. (1913). The Acambay-Tixmadeje mega-seismic zone, state of Mexico.
- Urrutia-Fucugauchi, J. and Flores-Ruiz, J.H., (1996). Bouguer gravity anomalies and regional crustal structure in central Mexico. *International Geology Review*, 38(2), pp.176-194.
- Vázquez-Sánchez, E. and Jaimes-Palomera, R., (1989). Geología de la Cuenca de México. *Geofísica Internacional*, 28(2), pp.133-190.
- Wu, Y.M. and Kanamori, H., (2008). Development of an earthquake early warning system using real-time strong motion signals. *Sensors*, 8(1), pp.1-9.
- Zobin, V.M., Amezcua, M.G., Davila, G.R., Domínguez, T., Chacón, J.C. and Alvarez, J.C., (2002). Comparative characteristics of the 1997–1998 seismic swarms preceding the November 1998 eruption of Volcan de Colima, Mexico. *Journal of volcanology and geothermal research*, 117(1-2), pp.47-60.

7.1 Appendix

7.1.1 Introduction

Data records from the Global CMT Project for focal mechanisms plotted in the introductory maps using GMT software.

Regional Name (with Date after 2005)	Long	Lat	Depth	Mag	Moment Tensor Components						
					mrr	mtt	mpp	mrt	mrp	mtp	iexp
060980A	-115.36	32.26	10	6.3	-0.52	-3.51	4.03	0.00	0.00	0.98	25
080980A	-88.27	16.25	11	6.5	0.55	-2.60	2.05	4.14	-2.35	4.83	25
102480B	-97.86	18.14	63	7.1	-4.96	3.59	1.37	-4.36	0.46	-1.89	26
110180E	-107.57	18.85	15	6.3	-0.57	-2.03	2.60	0.31	-1.12	-3.06	25
060181B	-107.84	18.77	10	6.2	-0.15	-1.40	1.54	0.00	0.00	-2.04	25
102581A	-102	18.28	32	7.2	4.76	-3.81	-0.94	4.76	-2.43	1.24	26
011282B	-87.3	12.80	10	6.2	0.08	-1.25	1.16	-0.15	0.37	-1.32	25
040682A	-91.95	13.79	43	6.7	1.23	-0.87	-0.37	0.60	-0.65	0.35	26
060782A	-98.22	16.50	11	6.9	0.73	-0.74	0.01	2.11	-1.82	0.27	26
060782B	-98.32	16.93	19	6.9	1.01	-0.88	-0.13	2.10	-1.28	0.41	26
061982A	-88.97	12.65	52	7.3	-7.45	7.15	0.30	5.77	-3.72	-3.20	26
103182B	-90.46	13.74	90	6.2	0.10	0.59	-0.69	2.00	-1.37	-0.06	25
012483A	-95.28	15.79	36	6.8	-1.09	0.16	0.93	-0.87	-0.93	-1.29	26
050983C	-109.77	19.38	10	6.3	0.67	-2.90	2.23	-0.90	-2.54	-1.86	25
071883A	-87.22	12.51	47	6.4	-1.33	2.84	-1.51	3.96	-2.95	-0.81	25
091583A	-93.44	15.88	122	6.3	-0.85	-0.01	0.87	1.37	-2.98	-0.77	25
120283A	-92.2	13.86	31	7.0	2.25	-1.74	-0.51	2.58	-1.37	0.85	26
121083A	-92.18	13.74	56	6.0	0.63	-1.16	0.52	0.42	-0.40	0.44	25
021084A	-112.11	28.01	10	6.0	0.35	-1.31	0.95	-0.02	0.20	-0.55	25
021784C	-108.72	20.59	10	6.0	0.21	-1.30	1.10	0.03	0.51	0.42	25
070284B	-97.63	15.92	39	6.2	0.95	-1.65	0.69	0.97	-0.95	0.44	25
082384A	-86.55	11.13	55	6.2	1.09	-1.81	0.72	0.69	-0.75	0.67	25
083184C	-93.33	15.75	108	6.2	-0.60	-1.00	1.60	1.64	-1.77	-0.59	25
120284A	-116.21	20.75	10	6.4	-3.24	1.53	1.71	-1.90	-2.19	1.75	25
041985A	-87.42	11.46	50	6.2	1.23	-1.24	0.01	0.52	-0.61	1.07	25
060385A	-90.79	12.52	20	6.2	1.92	-1.82	-0.09	1.78	-0.72	0.67	25
091585C	-96.85	17.70	71	6.0	-1.02	1.10	-0.07	-0.22	0.08	-0.50	25
091985B	-101.99	17.91	21	8.0	6.58	-4.95	-1.63	8.81	-2.11	1.97	27
092185A	-101.42	17.57	21	7.5	1.47	-1.05	-0.42	1.77	-1.08	0.45	27
121685A	-85.58	11.65	10	6.2	-0.16	-1.38	1.53	-0.04	0.04	0.69	25
043086A	-102.92	18.25	21	6.9	1.90	-1.52	-0.38	2.27	-1.00	0.52	26
092586A	-108.17	22.90	15	6.0	-0.14	-1.07	1.21	0.01	0.18	-0.27	25
120786D	-107.72	19.12	15	6.2	-0.24	-0.78	1.03	0.57	-0.02	-1.40	25
031287C	-94.39	15.61	17	6.2	0.80	-1.01	0.21	1.20	-0.04	0.12	25

Regional Name (with Date after 2005)	Long	Lat	Depth	Mag	Moment Tensor Components						
					mrr	mtt	mpp	mrt	mrp	mtp	iexp
040887B	-86.7	11.44	20	6.4	2.32	-1.70	-0.61	3.95	-2.01	1.13	25
071587B	-96.91	17.42	72	6.2	-2.44	1.92	0.52	-0.48	0.28	-1.10	25
100487B	-86.58	10.66	29	6.2	0.94	-0.69	-0.25	1.54	-0.74	0.60	25
111487D	-108.88	19.51	15	6.2	0.06	-2.01	1.95	0.00	0.00	-1.07	25
111787A	-87.32	12.17	56	6.4	2.30	-2.82	0.52	4.16	-2.95	1.20	25
112487A	-115.69	33.02	15	6.0	-0.07	-1.31	1.38	0.00	0.00	-0.48	25
112487G	-116	33.02	15	6.5	0.54	-7.28	6.74	-0.94	-1.10	-0.38	25
050688C	-85.8	11.52	76	6.6	-1.72	-3.24	4.96	4.00	-8.21	-1.45	25
061888C	-111.02	26.75	15	6.6	0.09	-1.04	0.95	-0.33	-0.01	-0.22	26
110388B	-90.61	13.84	54	6.6	-2.48	2.24	0.25	6.26	-6.04	-1.12	25
042589F	-99.12	16.83	15	6.9	0.73	-0.66	-0.06	1.94	-1.19	0.22	26
082989A	-105.65	17.88	15	6.5	0.51	-2.85	2.34	0.79	-1.85	-6.02	25
091689C	-93.7	16.05	112	6.2	-0.20	0.02	0.17	0.57	-1.16	-1.21	25
031690A	-108.86	24.34	15	6.2	0.05	-1.68	1.63	0.00	0.00	-0.70	25
040390C	-86.64	11.24	32	6.8	1.00	-0.76	-0.23	1.32	-0.56	0.53	26
010191A	-106.01	18.36	15	6.2	0.11	-0.49	0.38	0.00	0.00	-2.72	25
062291A	-108.45	23.64	15	6.2	0.01	-1.85	1.85	-0.13	0.45	-0.59	25
091891A	-91.01	14.79	15	6.2	0.22	-0.29	0.07	-0.10	1.63	-1.43	25
042392A	-116.52	34.07	15	6.2	-0.31	-0.47	0.77	-0.03	0.09	2.01	25
053092G	-93.13	14.32	29	6.3	2.62	-2.42	-0.19	1.86	-1.29	0.80	25
062892C	-116.65	34.65	15	7.3	-0.88	-6.22	7.00	3.81	0.10	7.34	26
062892H	-117.24	34.27	15	6.5	0.14	-6.81	6.67	0.04	0.36	0.62	25
090292A	-87.81	11.20	15	7.6	1.45	-0.93	-0.53	2.65	-1.66	0.44	27
090292V	-87.11	11.11	15	6.0	-0.10	-0.13	0.23	1.27	0.06	0.31	25
090592C	-87.71	11.39	22	6.0	1.02	-0.95	-0.07	-0.12	-0.30	0.41	25
092892A	-90.99	13.24	15	6.0	-1.09	0.94	0.15	-0.44	0.58	-0.18	25
051593E	-97.92	16.45	38	6.0	0.61	-1.17	0.56	0.79	-0.60	0.26	25
090393C	-93.14	14.40	27	6.7	1.11	-0.82	-0.30	0.88	-0.58	0.35	26
091093E	-92.54	13.91	16	6.0	0.53	-0.63	0.10	0.67	-1.00	-0.02	25
091093F	-92.99	14.41	29	7.2	6.39	-4.86	-1.53	4.48	-3.52	2.01	26
091993F	-93.47	14.39	16	6.4	2.81	-2.10	-0.71	3.58	-2.14	0.84	25
093093C	-94.83	15.08	15	6.5	4.28	-2.97	-1.30	4.38	-1.29	1.05	25
102493C	-98.61	16.77	22	6.6	5.53	-4.95	-0.57	7.20	-4.60	1.47	25
011794B	-118.64	34.44	17	6.6	1.08	-0.94	-0.14	0.05	-0.40	0.44	26
031494C	-92.64	15.98	168	6.8	0.51	-1.31	0.80	0.99	-1.71	0.07	26
031594A	-88.44	10.96	15	6.0	-1.35	0.98	0.37	-0.15	-0.30	-0.66	25
052394A	-100.2	18.19	70	6.2	-2.64	2.66	-0.02	-0.54	-0.51	0.31	25
070494D	-97.2	15.16	15	6.4	-5.89	1.76	4.13	-0.95	-0.64	-1.34	25
121094G	-101.39	18.18	54	6.4	-1.67	1.94	-0.26	-3.88	2.99	0.12	25
053195C	-107.57	19.05	18	6.3	0.08	-2.12	2.04	-1.63	0.42	-2.19	25
061495B	-88.81	11.82	15	6.5	-7.84	4.22	3.62	1.47	-2.62	-2.08	25

Regional Name (with Date after 2005)	Long	Lat	Depth	Mag	Moment Tensor Components						
					mrr	mtt	mpp	mrt	mrp	mtp	iexp
063095C	-110.21	24.65	15	6.2	-1.63	-0.20	1.83	-0.42	1.26	-1.16	25
082895A	-110.27	26.23	15	6.5	0.03	-5.90	5.87	0.27	1.44	-0.68	25
091495C	-98.54	16.73	22	7.3	0.67	-0.54	-0.13	1.03	-0.49	0.20	27
100995C	-104.8	19.34	15	8.0	3.62	-2.53	-1.09	9.44	-5.49	1.40	27
102195C	-93.42	16.67	164	7.2	0.38	-1.87	1.49	4.76	-4.95	-0.78	26
120195A	-103.88	10.38	15	6.6	-0.24	-3.26	3.50	2.48	-0.61	7.62	25
121195C	-105.75	18.84	15	6.3	-0.04	0.68	-0.64	0.70	-0.95	-3.13	25
121195G	-105.68	18.71	15	6.2	0.02	0.36	-0.38	-0.08	-0.35	-1.43	25
022596A	-97.98	15.88	15	7.1	3.08	-2.56	-0.51	4.11	-2.25	0.66	26
030396B	-87.13	11.55	36	6.6	6.83	-4.61	-2.21	5.08	-2.21	3.71	25
030396D	-87.31	11.76	39	6.7	1.02	-0.73	-0.29	0.65	-0.34	0.49	26
032796E	-88.61	11.73	15	6.0	-1.27	0.70	0.57	-0.36	0.07	-0.66	25
071596D	-101.12	17.50	22	6.6	6.73	-5.30	-1.43	6.90	-2.88	2.36	25
123196C	-93.18	15.83	82	6.3	-2.46	1.26	1.21	2.17	-1.96	-1.76	25
011197D	-102.58	18.34	40	7.1	-1.44	0.50	0.94	5.17	-2.05	-2.14	26
050197D	-107.15	18.96	15	6.9	-0.17	-1.58	1.75	-0.16	0.76	-2.09	26
052297B	-101.73	18.76	56	6.5	-5.29	5.39	-0.10	3.69	0.38	-0.53	25
071997D	-98.26	15.86	15	6.7	5.93	-4.92	-1.01	9.39	-4.63	1.38	25
110997C	-89.3	13.88	178	6.3	2.07	-1.09	-0.98	2.38	-2.38	0.74	25
011098D	-91.93	14.37	55	6.6	-2.15	-1.19	3.34	6.02	-5.43	-2.95	25
020398A	-96.22	15.92	24	6.3	3.61	-3.56	-0.05	0.61	0.54	0.56	25
030398A	-91.91	14.23	44	6.2	-0.60	-0.05	0.65	1.03	-0.82	-0.40	25
051098B	-91.35	13.59	25	6.3	2.40	-2.15	-0.24	2.28	-1.50	0.90	25
060798C	-93.99	15.96	76	6.2	0.00	0.04	-0.04	1.57	-2.17	0.13	25
082398C	-88.55	11.58	15	6.7	-1.19	0.68	0.51	-0.12	-0.22	-0.62	26
050599E	-94.86	14.63	15	6.2	-1.79	1.34	0.45	-0.33	-0.22	-0.91	25
050899H	-92.38	14.19	32	6.0	1.08	-0.96	-0.12	0.61	-0.45	0.45	25
060699C	-91.43	14.01	38	6.2	-0.60	-0.51	1.10	-2.31	-0.26	-1.26	25
061599F	-97.38	18.44	61	6.9	-3.11	2.08	1.03	-0.64	0.11	-1.30	26
062199E	-101.62	18.09	48	6.3	-1.55	2.04	-0.49	-1.75	1.71	-0.55	25
071199B	-88.53	16.04	15	6.7	0.06	-0.58	0.52	0.32	-0.18	1.03	26
093099E	-96.96	16.20	47	7.4	-1.75	1.42	0.32	0.08	-0.36	-0.50	27
101699C	-116.27	34.71	15	7.1	-0.09	-4.27	4.35	0.69	0.98	3.98	26
112199D	-107.39	19.16	15	6.2	-0.09	-1.20	1.29	-0.01	0.47	-1.36	25
031200D	-93.02	14.84	67	6.3	1.02	-1.42	0.40	1.95	-2.03	0.52	25
080900C	-102.39	18.13	33	6.5	7.00	-6.33	-0.67	0.49	-0.12	2.42	25
011301C	-89.13	12.97	56	7.7	-4.24	2.92	1.32	1.20	-1.12	-2.01	27
021301B	-88.97	13.98	15	6.5	-0.39	-1.61	2.00	-0.63	2.41	-7.50	25
042901B	-104.74	18.71	15	6.2	1.15	-0.88	-0.28	1.25	-0.96	0.47	25
052001A	-104.57	18.62	15	6.3	1.91	-1.50	-0.40	2.39	-1.93	0.87	25
111301B	-107.06	22.44	15	6.0	-0.05	-1.27	1.32	0.40	-0.01	0.24	25

Regional Name (with Date after 2005)	Long	Lat	Depth	Mag	Moment Tensor Components						
					mrr	mtt	mpp	mrt	mrp	mtp	iexp
112801C	-93.4	15.78	65	6.4	-2.21	1.66	0.55	3.32	-1.97	-1.40	25
011602G	-93.44	15.69	56	6.4	-1.06	0.80	0.26	3.55	-2.60	-0.43	25
041802B	-101.22	16.79	15	6.7	0.53	-0.41	-0.12	1.33	-0.55	0.14	26
100302C	-108.27	23.22	15	6.5	-0.31	-5.67	5.97	0.85	0.80	-1.84	25
012103B	-91.31	13.53	41	6.4	4.83	-3.91	-0.92	1.76	-1.47	1.93	25
012203A	-103.9	18.86	26	7.5	0.79	-0.62	-0.18	1.81	-0.54	0.34	27
031203C	-110.91	26.63	15	6.3	-0.07	-3.72	3.79	0.89	0.09	-0.57	25
051903D	-105.57	17.72	15	6.2	0.03	-1.56	1.53	0.20	-0.13	-0.28	25
071703B	-107.37	18.92	15	6.0	-0.05	-0.72	0.78	-0.04	0.06	-0.93	25
010104K	-101.4	17.45	15	6.0	0.63	-0.52	-0.11	1.16	-0.59	0.30	25
030204A	-87.25	11.45	26	6.2	1.15	-0.83	-0.32	1.66	-0.99	0.63	25
042904B	-86.38	10.32	19	6.2	1.14	-0.79	-0.35	1.79	-1.05	0.57	25
062904B	-87.47	10.57	12	6.3	-3.16	1.85	1.30	-0.78	0.19	-1.70	25
100904E	-87.02	11.25	39	6.9	2.32	-1.51	-0.81	1.65	-0.94	1.15	26
112004F	-90.61	13.13	34	6.3	2.52	-2.18	-0.34	1.57	-1.40	1.19	25
200503171337A	-91.63	15.20	181	6.2	0.82	-0.79	-0.03	1.30	-1.42	0.35	25
200506271135A	-107.38	18.89	16	6.2	-0.23	-1.18	1.41	-0.27	0.51	-1.57	25
200507020216A	-86.7	11.06	28	6.6	0.65	-0.44	-0.21	0.61	-0.41	0.42	26
200508031103A	-85.56	11.38	12	6.3	0.04	-2.36	2.32	0.12	0.08	1.89	25
200601040832A	-112.51	28.38	15	6.6	-0.03	-0.92	0.95	0.00	-0.04	-0.20	26
200604040230A	-107.1	18.75	26	6.0	-0.07	-0.62	0.68	-0.14	0.16	-0.91	25
200608111430A	-101.06	18.50	58	6.0	-1.06	1.18	-0.12	0.51	-0.14	-0.24	25
200612032052A	-91.77	13.90	47	6.0	-0.58	0.26	0.32	0.69	-0.66	-0.40	25
200704130542A	-100.14	17.37	43	6.0	0.57	-0.60	0.03	-0.86	0.22	0.13	25
200706131929A	-91.22	13.43	32	6.7	1.07	-0.92	-0.15	0.48	-0.43	0.46	26
200707060109A	-93.89	16.48	114	6.0	-0.65	0.02	0.62	0.90	-0.85	-0.61	25
200709011914A	-109.89	24.76	15	6.2	-0.25	-1.38	1.63	-0.28	0.07	-1.13	25
200802121250A	-94.51	16.35	87	6.5	-4.47	-0.22	4.69	2.73	-1.81	-2.84	25
200804150303A	-91	13.42	33	6.2	0.45	-1.51	1.06	-0.89	1.32	-0.47	25
200809240233A	-105.6	17.69	17	6.4	0.59	-5.01	4.42	0.35	0.22	-1.35	25
200810161941A	-92.9	14.28	30	6.6	0.87	-0.71	-0.16	0.57	-0.51	0.43	26
200905031621A	-91.5	14.56	90	6.3	-1.10	1.34	-0.24	1.99	-1.90	-1.31	25
200905280824A	-87.17	16.50	12	7.3	-0.03	-0.81	0.84	-0.46	0.51	0.72	27
200908031800A	-113.53	29.22	12	6.9	-0.03	-2.50	2.54	-0.04	-0.16	-0.33	26
200908031840A	-113.75	29.43	19	6.2	-0.40	-2.66	3.06	-0.26	-0.45	-0.34	25
200909240716A	-107.5	18.90	14	6.4	0.50	-3.06	2.56	-0.12	0.25	-3.50	25
201004042240A	-115.39	32.31	13	7.2	-0.23	-0.64	0.87	0.04	-0.06	-0.05	27
201006300722A	-97.77	16.47	18	6.3	1.22	-1.02	-0.20	2.30	-1.60	0.48	25
201008240212A	-107.42	18.84	24	6.2	-0.01	-1.44	1.45	-0.21	0.27	-1.81	25
201010211753A	-109.29	24.83	14	6.7	0.04	-1.32	1.27	-0.11	0.05	-0.20	26
201102251307A	-95.2	17.98	128	6.0	-1.06	0.14	0.91	0.32	-0.05	-0.57	25

Regional Name (with Date after 2005)	Long	Lat	Depth	Mag	Moment Tensor Components						
					mrr	mtt	mpp	mrt	mrp	mtp	iexp
201104071311A	-94.12	17.28	154	6.7	-0.56	-0.29	0.86	0.91	-0.62	-0.57	26
201107261744A	-109.63	25.06	17	6.0	-0.07	-1.36	1.43	-0.35	0.01	-0.12	25
201111011232A	-109.32	19.93	17	6.2	0.04	-2.34	2.30	-0.15	-0.14	-1.41	25
201111072235A	-85.98	11.60	173	6.0	0.96	-0.54	-0.42	0.48	-0.88	0.35	25
201112110147A	-99.84	17.89	55	6.5	-5.61	5.37	0.24	-2.35	0.07	-1.02	25
201201211847A	-93.35	14.85	60	6.2	-1.77	0.11	1.66	0.90	-0.79	-1.35	25
201203201802A	-98.39	16.60	15	7.5	0.68	-0.56	-0.12	1.74	-0.66	0.24	27
201203261812A	-104.19	10.29	12	6.0	-0.04	-0.47	0.51	-0.04	0.02	1.18	25
201204021736A	-98.35	16.58	12	6.2	-1.31	1.40	-0.09	0.68	-0.06	0.01	25
201204112255A	-102.97	18.10	21	6.7	0.86	-0.82	-0.04	0.70	-0.39	0.31	26
201204120706A	-113.09	28.90	16	6.2	-0.28	-1.30	1.58	-0.47	-0.66	-0.04	25
201204120715A	-112.76	28.57	16	7.0	-0.21	-4.22	4.43	-0.93	-0.84	-0.64	26
201205012243A	-93.35	14.38	13	6.0	1.06	-0.90	-0.16	0.67	-0.60	0.42	25
201208270437A	-89.17	12.02	12	7.3	0.62	-0.53	-0.09	0.98	-0.52	0.18	27
201209051442A	-85.64	10.00	30	7.6	1.85	-1.37	-0.48	2.61	-1.16	0.86	27
201209252345A	-110.29	24.92	12	6.3	-2.47	-0.63	3.10	1.01	-0.41	-0.88	25
201210080626A	-109.73	25.17	20	6.0	-0.04	-1.14	1.18	-0.22	-0.08	-0.22	25
201211071635A	-92.43	14.11	21	7.4	1.11	-0.88	-0.23	0.79	-0.53	0.41	27
201211112215A	-92.68	13.94	12	6.4	3.30	-3.04	-0.25	3.66	-2.21	1.24	25
201211150920A	-100.48	18.30	53	6.2	-1.52	1.39	0.12	-0.40	-0.04	-0.54	25
201212141036A	-119.61	31.08	21	6.4	-4.03	0.90	3.13	-0.53	-0.76	2.59	25
201303252302A	-90.71	14.62	186	6.2	0.73	-1.46	0.73	1.54	-1.78	-0.03	25
201304220116A	-102.19	18.05	27	6.2	1.28	-1.01	-0.26	-0.69	0.64	0.73	25
201306151734A	-87.3	11.62	39	6.4	4.87	-3.63	-1.25	1.88	-1.34	2.63	25
201308211238A	-99.54	17.00	23	6.2	1.48	-1.30	-0.18	1.38	-0.96	0.49	25
201309070013A	-92.11	14.54	80	6.4	0.12	-1.46	1.34	4.13	-3.58	-0.21	25
201310191754A	-110.53	26.29	16	6.6	0.00	-0.88	0.88	-0.01	-0.11	-0.09	26
201403020937A	-87.91	12.52	62	6.2	0.84	-0.55	-0.28	1.91	-1.98	0.61	25
201403022217A	-93.25	14.35	16	6.0	0.71	-0.60	-0.11	0.81	-0.58	0.21	25
201404102327A	-86.54	12.42	15	6.2	-0.38	-1.63	2.01	-0.34	-0.30	-0.60	25
201404112029A	-86.22	11.70	142	6.6	0.49	-0.25	-0.24	0.53	-0.79	0.08	26
201404181427A	-101.25	17.55	19	7.3	0.61	-0.44	-0.17	0.74	-0.33	0.23	27
201405081700A	-100.74	17.36	21	6.5	4.24	-3.51	-0.73	3.87	-2.40	1.61	25
201405100736A	-100.82	17.31	21	6.2	1.11	-0.95	-0.16	1.02	-0.62	0.37	25
201405311153A	-107.5	18.99	17	6.2	-0.16	-1.45	1.61	-0.08	0.05	-1.84	25
201407071123A	-92.7	14.80	63	6.9	-2.11	0.77	1.34	1.21	-1.19	-1.36	26
201407291046A	-95.69	17.97	109	6.4	-3.95	1.04	2.91	0.79	-1.37	-2.45	25
201409061923A	-107.38	18.93	25	6.2	-0.07	-1.22	1.29	0.06	0.07	-1.49	25
201410080240A	-108.62	23.85	15	6.2	-0.12	-1.61	1.74	-0.19	-0.04	-0.47	25
201410140351A	-88.45	12.33	41	7.3	-0.73	0.48	0.24	0.57	-0.47	-0.41	27
201412072116A	-91.84	13.65	26	6.2	1.04	-0.67	-0.37	0.75	-0.77	0.55	25

Regional Name (with Date after 2005)	Long	Lat	Depth	Mag	Moment Tensor Components						
					mrr	mtt	mpp	mrt	mrp	mtp	iexp
201502221423A	-106.85	18.82	15	6.2	-0.21	-1.44	1.65	0.01	0.05	-2.42	25
201509130814A	-109.53	25.09	15	6.6	-0.03	-0.96	0.99	-0.01	-0.02	-0.16	26
201512171949A	-93.6	15.84	73	6.6	-3.29	0.48	2.81	5.79	-5.22	-2.38	25
201601211806A	-107.17	18.91	16	6.6	-0.57	-4.88	5.45	0.20	-0.33	-6.75	25
201604151411A	-92.67	13.49	12	6.0	-1.29	0.81	0.48	-0.14	0.17	-0.70	25
201604250707A	-93.38	14.45	17	6.0	0.75	-0.57	-0.18	0.64	-0.60	0.29	25
201604271251A	-93.39	14.55	22	6.0	0.95	-0.70	-0.25	0.57	-0.50	0.34	25
201604290133A	-103.9	10.42	15	6.6	-0.03	-0.42	0.44	-0.01	-0.03	0.95	26
201606071051A	-105.33	18.43	12	6.3	-0.16	-0.19	0.34	0.35	-0.23	-3.16	25
201606100325A	-87.13	12.92	14	6.2	-0.57	-1.30	1.87	-0.40	-0.17	-0.81	25
201611241843A	-89.2	11.83	12	6.9	-3.01	2.02	0.99	-0.39	0.32	-1.64	26
201705121041A	-90.38	12.69	18	6.2	-2.22	-0.47	2.69	0.85	-0.05	-0.35	25
201706140729A	-92.17	14.92	73	6.9	-1.48	0.84	0.63	2.25	-1.83	-1.10	26
201706221231A	-91.38	13.57	38	6.8	1.66	-1.28	-0.38	0.62	-0.46	0.69	26
201709080449A	-94.66	15.38	45	8.2	-1.09	0.36	0.73	1.75	-1.89	-0.65	28
201709191814A	-98.63	18.59	51	7.1	-6.56	5.32	1.24	-0.42	-0.48	-2.36	26
201709231253A	-95.11	16.72	13	6.0	-1.23	1.30	-0.07	0.08	-0.31	0.69	25
201801191617A	-111.06	26.78	17	6.3	-0.20	-3.04	3.24	-0.10	-0.46	-0.61	25
201802162339A	-97.88	16.53	20	7.2	3.19	-2.53	-0.66	5.46	-3.03	1.11	26
201802170036A	-97.8	16.27	17	6.0	0.61	-0.56	-0.06	0.89	-0.08	0.05	25
201810282223A	-90.76	12.71	12	6.2	1.12	-0.79	-0.33	1.11	-0.86	0.39	25
201902011614A	-92.46	14.86	46	6.7	-0.08	-0.10	0.18	0.92	-0.76	-0.09	26
201905300903A	-89.55	13.07	46	6.6	-0.54	0.70	-0.16	0.47	-0.53	-0.25	26
201911200427A	-93.51	14.06	22	6.3	3.20	-2.86	-0.34	1.58	-0.26	1.02	25
202001050440A	-94.53	16.50	86	6.0	-0.76	-0.15	0.91	0.49	-0.24	-0.53	25

Table 13. Catalogue of the strongest seismic events ($\geq M_w 6.0$) in Mexico from 1980-2020. Data from Global CMT Project.

7.1.2 Data

SSN Seismic Station Network		
Station	Lat	Long
	Broadband	
PPIG	19.06705	-98.62815
PZIG	19.32900	-99.17800
	Mexico Valley and Delegation	
AMVM	19.13189	-98.78587
AOVM	19.26757	-99.32190
APVM	19.48802	-99.20865
AZVM	19.58483	-99.28293
BJVM	19.37499	-99.17069
CHVM	19.08837	-99.14748
CIVM	19.10355	-98.98812
CJVM	19.36165	-99.28509
COVM	19.35110	-99.15616
CTVM	19.44303	-99.16550
GMVM	19.49304	-99.11103
ICVM	19.38448	-99.09895
INVM	19.29123	-99.38274
IPVM	19.34610	-99.09147
MCVM	19.32063	-99.25532
MHVM	19.40798	-99.20908
MPVM	19.20101	-99.01144
MZVM	19.18918	-99.22932
PBVM	19.44073	-99.08323
PTVM	19.59128	-99.11250
THVM	19.31101	-98.97320
TLVM	19.20939	-99.15373
TXVM	19.43369	-98.91786
VRVM	19.41785	-99.11440
XCVM	19.25273	-99.11685
	Excluded from view	
ATVM	19.76185	-99.84105
MAVM	18.95721	-99.49409
TOVM	19.28284	-99.67769
VTVM	19.77010	-98.77451
ZUVM	19.82646	-99.07754

Table 14. Seismic stations (32) from the National Seismological Service (SSN) networks in the Basin of Mexico. Stations ‘excluded from view’ are part of the Mexico Valley network referenced in Figure 1.

7.1.3 Methodology

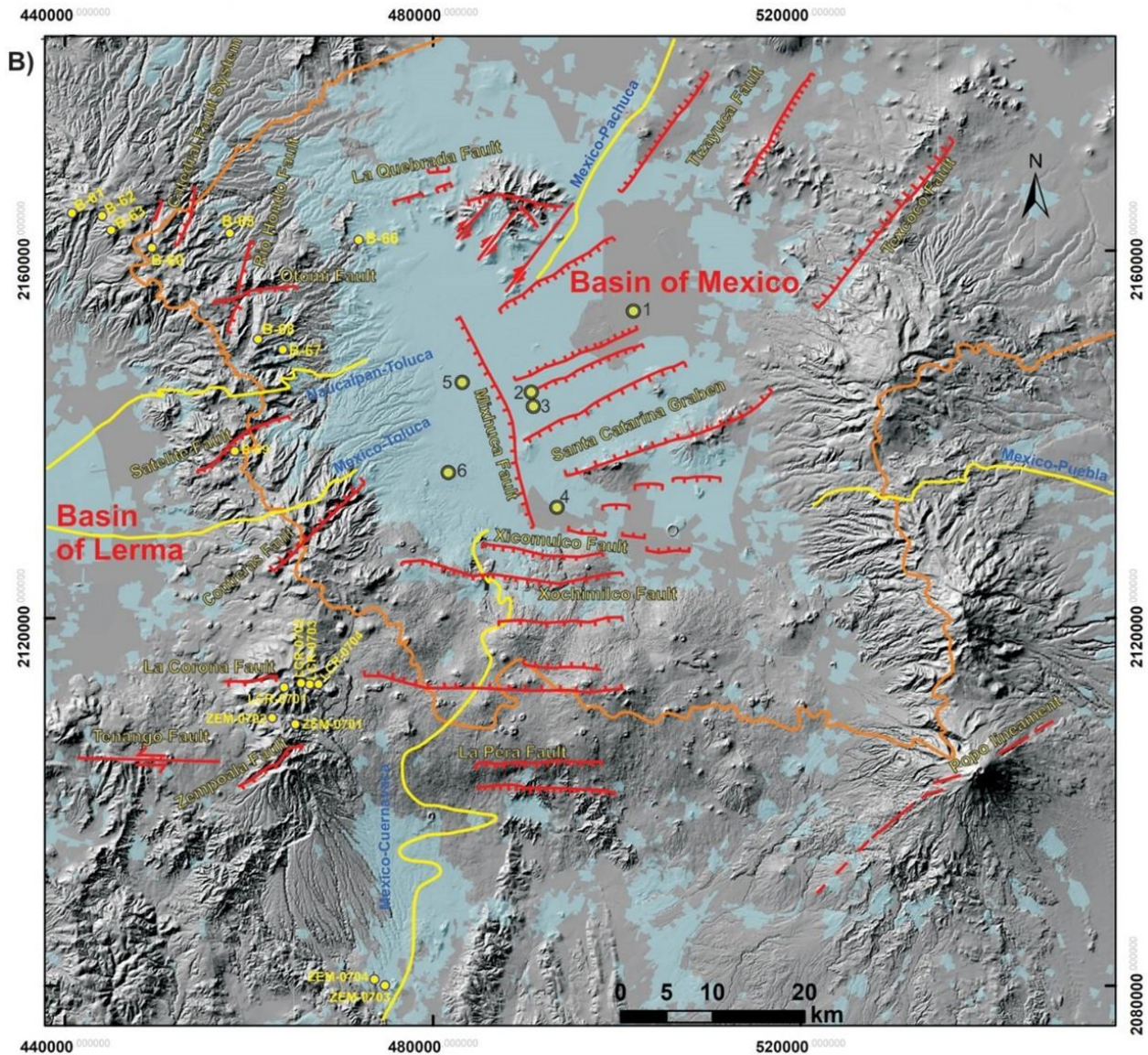


Figure 26. Digital Elevation Model describing the tectonic systems in the Mexican Basin and surrounding areas, including the Sierra Nevada (East), Sierra de las Cruces (West) and the Chichinautzin Monogenic Field (South). Yellow markers correspond to deep well sites with smaller yellow points highlighting the location of dated samples by Arce *et al.*, 2019 (DEM modified from Arce *et al.*, 2019).

7.1.4 Results

7.1.4.1 Depth Analysis

Data records from the SSN for seismic events in the Basin of Mexico 1974-2020.

Event	Date	Magnitude (M)	Latitude	Longitude	Depth (km)
1	07/06/1976	1	19.25	-99.21	-4
2	05/01/1977	1	19.23	-99.24	-16
3	29/07/1979	1	19.25	-99.22	-5
4	15/02/1980	1	19.28	-99.14	-33
5	19/02/1980	1	19.24	-99.15	-5
6	21/05/1981	1	19.27	-99.14	-9
7	22/10/1981	1	19.28	-99.09	-18
8	29/11/1983	1	19.19	-99.2	-5
9	27/11/1984	1	19.29	-99.05	-5
10	17/10/1985	1	19.23	-99.17	-4
11	12/03/1987	1	19.31	-99.07	-5
12	20/09/1997	3	19.27	-99.17	-7
13	26/10/2009	3	19.24	-99.18	-9
14	11/02/2010	2	19.28	-99.16	-12
15	25/08/2013	2	19.3197	-99.097	-4
16	25/08/2013	2	19.3115	-99.1022	-1
17	23/08/2015	2	19.241	-99.1818	-3
18	28/10/2017	2	19.2183	-99.2253	-2

Table 15. Seismic events in the Mexican Basin (1974-2020) ≤ 2.5 km from the SC fault. Data from SSN Mexico.

Event	Date	Magnitude	Latitude	Longitude	Depth (km)
19	07/06/1976	1	19.3	-99.03	-4
20	05/12/1976	1	19.31	-99.14	-33
21	26/01/1977	1	19.3	-99.18	-1
22	23/06/1980	1	19.2	-99.2	-3
23	24/10/1981	2	19.2	-99.2	-2
24	29/11/1983	1	19.25	-99.22	-5
25	04/12/1983	1	19.26	-99.22	-4
26	10/07/1984	1	19.36	-99.05	-1
27	05/01/1986	2	19.3	-99.15	-1
28	17/03/1990	3	19.22	-99.18	-5
29	15/12/1999	2	19.28	-99.2	-20
30	15/12/1999	2	19.27	-99.21	-9
31	16/10/2005	3	19.31	-99.14	-14
32	16/06/2013	2	19.2992	-99.173	-4
33	24/08/2014	2	19.2528	-99.1095	-3
34	10/11/2016	2	19.3345	-99.0115	-6
35	09/09/2017	2	19.2965	-99.1813	-8
36	20/09/2017	1	19.276	-99.2058	-4
37	20/09/2017	1	19.266	-99.2108	-2
38	01/09/2019	1	19.323	-99.132	-1

Table 16. Seismic events in the Mexican Basin (1974-2020) between 2.5km and 5km from the SC fault. Data from SSN Mexico.

Event	Date	Magnitude (M)	Latitude	Longitude	Depth (km)
39	13/07/1974	1	19.340	-99.140	-5
40	07/06/1976	1	19.250	-99.040	-4
41	09/04/1977	1	19.360	-99.080	-5
42	04/03/1979	1	19.360	-99.000	-4
43	19/08/1980	1	19.160	-99.240	-37
44	15/08/1981	1	19.160	-99.270	-5
45	26/12/1981	1	19.300	-99.200	-5
46	26/06/1982	1	19.300	-99.200	-5
47	07/12/1983	1	19.210	-99.110	-4
48	30/10/1985	1	19.210	-99.150	-4
49	04/08/1993	3	19.270	-99.020	-12
50	16/10/2005	3	19.350	-99.090	-5
51	16/10/2005	3	19.300	-99.200	-14
52	28/02/2006	3	19.350	-99.020	-2
53	11/07/2009	2	19.340	-99.150	-8
54	16/06/2013	2	19.347	-99.132	-1
55	17/06/2013	2	19.370	-99.087	-1
56	25/08/2013	2	19.353	-99.121	-5
57	04/09/2013	3	19.362	-99.029	-5
58	06/10/2014	2	19.225	-99.097	-3
59	06/10/2014	2	19.230	-99.089	-3
60	21/06/2015	1	19.329	-99.155	-4
61	01/03/2017	2	19.338	-99.146	-5
62	01/03/2017	2	19.342	-99.135	-2
63	01/03/2017	1	19.339	-99.145	-5
64	02/03/2017	1	19.339	-99.145	-5
65	16/10/2017	1	19.329	-99.166	-2
66	17/10/2017	1	19.318	-99.168	-3
67	09/11/2017	1	19.326	-99.179	-7
68	15/11/2017	1	19.272	-99.273	-14
69	27/09/2018	2	19.320	-99.163	-1
70	26/05/2019	1	19.230	-99.309	-3
71	01/09/2019	2	19.330	-99.162	-3

Table 17. Seismic events in the Mexican Basin (1974-2020) between 5km and 7.5km from the SC fault. Data from SSN Mexico.

Event	Date	Magnitude (M)	Latitude	Longitude	Depth (km)
72	12/07/1974	1	19.380	-99.080	-5
73	21/04/1976	1	19.250	-99.340	-4
74	23/06/1978	1	19.220	-99.050	-33
75	04/03/1979	1	19.330	-98.970	-4
76	06/04/1979	1	19.380	-99.000	-4
77	07/07/1979	1	19.350	-99.150	-5
78	31/03/1980	1	19.200	-99.100	-5
79	07/02/1981	1	19.240	-99.340	-2
80	08/03/1981	1	19.360	-99.160	-3
81	23/12/1983	1	19.300	-99.260	-4
82	15/10/1985	1	19.180	-99.160	-4
83	17/10/1985	1	19.160	-99.160	-4
84	19/10/1985	1	19.280	-99.290	-4
85	10/05/1988	3	19.220	-99.050	-33
86	25/09/1998	2	19.400	-99.060	-13
87	06/04/1999	2	19.380	-99.090	-13
88	28/05/1999	2	19.280	-98.980	-3
89	15/12/1999	3	19.270	-99.140	-36
90	25/01/2007	3	19.180	-99.160	-30
91	18/01/2013	2	19.353	-99.169	-10
92	10/05/2013	1	19.293	-99.294	-1
93	16/06/2013	2	19.392	-99.099	-1
94	17/06/2013	2	19.356	-99.126	-1
95	17/06/2013	2	19.371	-99.120	-1
96	18/06/2013	2	19.364	-99.119	-5
97	25/08/2013	2	19.373	-99.100	-9
98	02/12/2013	2	19.339	-99.195	-1
99	09/04/2015	2	19.402	-99.073	-7
100	28/02/2017	2	19.349	-99.140	-4
101	28/02/2017	2	19.350	-99.149	-5
102	20/09/2017	1	19.337	-99.204	-4
103	16/10/2017	1	19.329	-99.178	-2
104	09/11/2017	1	19.346	-99.152	-7
105	15/06/2018	2	19.333	-99.174	-3
106	14/09/2018	2	19.375	-99.135	-1

Table 18. Seismic events in the Mexican Basin (1974-2020) between 7.5km and 10km from the SC fault. Data from SSN Mexico.

Mexican Basin Seismic Event	Total Annual Seismic Events $M_w > 5$ in the Republic of Mexico	National Seismic Events $M_w > 5$ with corresponding dates to the events in the Basin of Mexico	
		Magnitude (M_w)	Date
12/07/1974	11	6.3	31/05/1974
13/07/1974			
26/01/1977	7	5.2	04/01/1977
04/12/1983	17	5.3	25/11/1983
23/12/1983			
06/04/1999	11	n/a	
15/12/1999		5.6	21/11/1999
15/12/1999			
21/04/2002	25	6.5; 6.0; 5.5; 5.3	18/04/2002
		5.0	21/04/2002
16/04/2005	12	5.6	27/02/2005
16/06/2013	19	5.8	16/06/2013
16/06/2013			
17/06/2013			
17/06/2013			
18/06/2013		5.0; 6.0	21/08/2013
25/08/2013			
25/08/2013			
04/09/2013			
09/04/2015	20	6.2	22/02/2015
		5.4	20/03/2015
21/06/2015		5.6	28/04/2015
28/02/2017	19	5	13/02/2017
28/02/2017			
01/03/2017			
01/03/2017			
01/03/2017		8.2	08/09/2017
02/03/2017			
09/09/2017			
20/09/2017			
20/09/2017	7.1	19/09/2017	
27/09/2018	20	5.2; 5.0	24/09/2018
03/07/2020	16	6.1	22/05/2020.
		5.2	02/07/2020

Table 19. National seismic events (1974-2020) of $M_w > 5$ that have occurred ≤ 60 days prior to seismic events in the Basin of Mexico within 10km of the SC fault (Table 1). Events highlighted in red correspond to the 23.5km linear distribution identified to estimate the depth of the SC fault. Data from SSN and Global CMT project.

7.1.4.2 1D Amplification Factor Model

Cross Section (100m Resolution)			
x	Basement (m)	Soil Layer 2 (m)	Soil Layer 1 (m)
0	2341	2341	2341
0.1	2337	2337	2337
0.2	2330	2330	2330
0.3	2323	2323	2323
0.4	2321	2321	2321
0.5	2307	2307	2307
0.6	2284	2284	2284
0.7	2283	2283	2283
0.8	2284	2284	2284
0.9	2276	2276	2276
1	2271	2271	2271
1.1	2268	2268	2268
1.2	2269	2269	2269
1.3	2270	2270	2270
1.4	2270	2270	2270
1.5	2283	2283	2283
1.6	2282	2282	2282
1.7	2275	2275	2275
1.8	2257	2257	2257
1.9	2258	2258	2258
2	2255	2255	2255
2.1	2253	2253	2253
2.2	2254	2254	2254
2.3	2255	2255	2255
2.4	2253	2253	2253
2.5	2251	2251	2251
2.6	2248	2248	2248
2.7	2249	2249	2249
2.8	2247	2247	2247
2.9	2247	2247	2247
3	2244	2244	2246
3.1	2214	2214	2244
3.2	2213	2213	2243
3.3	2211	2211	2241
3.4	2212	2212	2242
3.5	2213	2213	2243
3.6	2209	2209	2239
3.7	2213	2213	2243

Cross Section (100m Resolution)			
x	Basement (m)	Soil Layer 2 (m)	Soil Layer 1 (m)
3.8	2213	2213	2243
3.9	2194	2214	2244
4	2191	2211	2241
4.1	2192	2212	2242
4.2	2193	2213	2243
4.3	2191	2211	2241
4.4	2190	2210	2240
4.5	2188	2208	2238
4.6	2189	2209	2239
4.7	2190	2210	2240
4.8	2190	2210	2240
4.9	2189	2209	2239
5	2188	2208	2238
5.1	2190	2210	2240
5.2	2188	2208	2238
5.3	2188	2208	2238
5.4	2190	2210	2240
5.5	2186	2206	2236
5.6	2189	2209	2239
5.7	2190	2210	2240
5.8	2187	2207	2237
5.9	2189	2209	2239
6	2185	2205	2235
6.1	2186	2206	2236
6.2	2186	2206	2236
6.3	2187	2207	2237
6.4	2185	2205	2235
6.5	2187	2207	2237
6.6	2190	2210	2240
6.7	2190	2210	2240
6.8	2189	2209	2239
6.9	2190	2210	2240
7	2190	2210	2240
7.1	2190	2210	2240
7.2	2191	2211	2241
7.3	2191	2211	2241
7.4	2191	2211	2241
7.5	2194	2214	2244
7.6	2190	2210	2240
7.7	2190	2210	2240
7.8	2189	2209	2239
7.9	2210	2210	2240

Cross Section (100m Resolution)			
x	Basement (m)	Soil Layer 2 (m)	Soil Layer 1 (m)
8	2210	2210	2240
8.1	2212	2212	2242
8.2	2212	2212	2242
8.3	2211	2211	2241
8.4	2212	2212	2242
8.5	2212	2212	2242
8.6	2213	2213	2243
8.7	2213	2213	2243
8.8	2213	2213	2243
8.9	2215	2215	2245
9	2216	2216	2246
9.1	2218	2218	2248
9.2	2221	2221	2251
9.3	2256	2256	2256
9.4	2260	2260	2260
9.5	2268	2268	2268
9.6	2276	2276	2276
9.7	2285	2285	2285
9.8	2293	2293	2293
9.9	2300	2300	2300
10	2306	2306	2306
10.1	2312	2312	2312
10.2	2315	2315	2315
10.3	2322	2322	2322
10.4	2330	2330	2330
10.5	2336	2336	2336
10.6	2343	2343	2343
10.7	2350	2350	2350
10.8	2358	2358	2358
10.9	2365	2365	2365
11	2371	2371	2371

Table 20. Elevation data for the 1D Amplification factor model.

a) Single layer

$$T = \frac{4 \sum H_i}{V_s}$$

b) Multiple layers

$$T = \frac{4 \sum H_i}{\frac{\sum_{i=1}^n V_i H_i}{\sum H_i}}$$

(3) Soil Layers One - Three

$$T = \frac{4(\sum 30_1 + 20_2 + 250_3)}{\frac{\sum_{i=1}^n (50_1 \times 30_1) + (100_2 \times 20_2) + (400_3 \times 250_3)}{\sum_i 75}}$$

$$T = \frac{1200}{\frac{103,500}{300}}$$

$$T = 3.47s$$

(4) Soil Layers One - Four

$$T = \frac{4(\sum 30_1 + 20_2 + 250_3 + 250_4)}{\frac{\sum_{i=1}^n (50_1 \times 30_1) + (100_2 \times 20_2) + (400_3 \times 250_3) + (800_4 \times 250_4)}{\sum_i 550}}$$

$$T = \frac{2200}{\frac{303,500}{550}}$$

$$T = 3.99s$$

(5) Soil Layers One - Five

$$T = \frac{4(\sum 30_1 + 20_2 + 250_3 + 250_4 + 1420_5)}{\sum_{i=1}^n (50_1 \times 30_1) + (100_2 \times 20_2) + (400_3 \times 250_3) + (800_4 \times 250_4) + (1420_5 \times 1560_5)} \times 1970$$

$$T = \frac{7880}{2,518,700} \times 1970$$

$$T = 6.16s$$

Seismic Micro-Zone	H (m)	Vp (m/s)	Vs (m/s)	Accumulated Time Period (s)
<i>C</i>	250	2000	400	3.47
<i>D</i>	250	2500	800	3.99
<i>E</i>	1420	2700	1560	6.16

Table 21. Velocity structure for seismic micro-zones in the Mexican Basin. Zones C – E were not intersected by the San Pedro Martir - Camino Cerro de la Estrella cross-section (edited from Cruz et al, 2016).

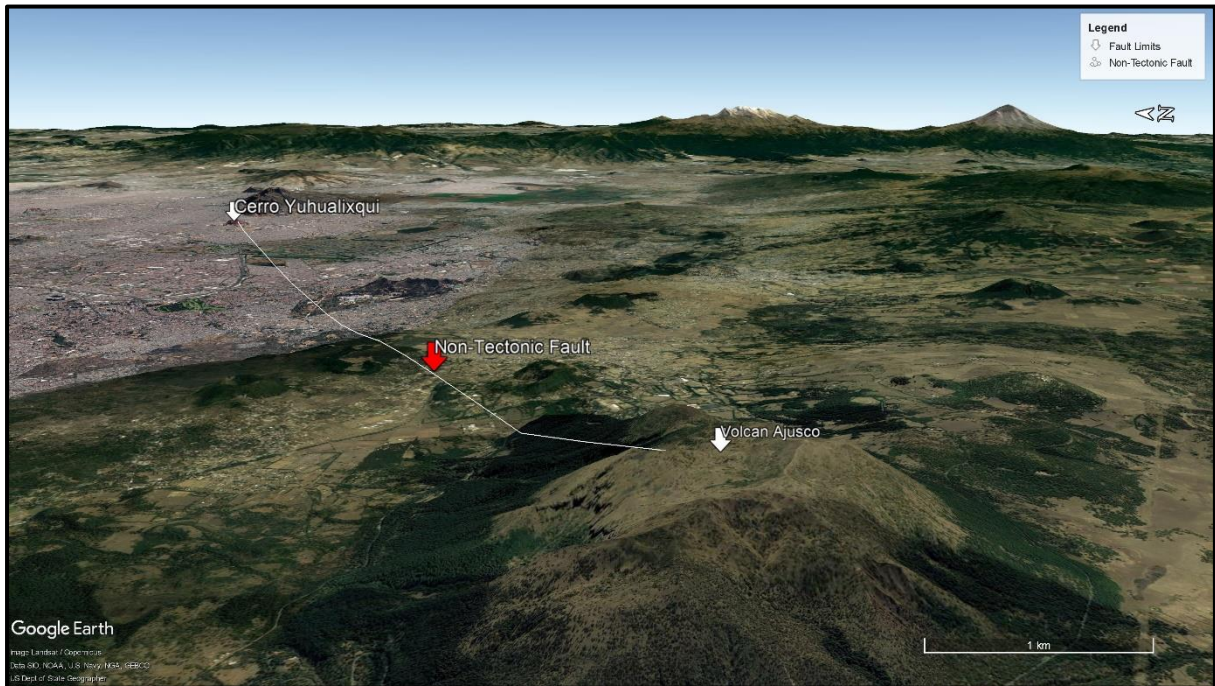


Figure 27. 3D surface elevation of the SC fault. Created with Google Earth Pro.



Figure 28. 3D surface elevation of the 1D amplification model cross-section. Created with Google Earth Pro.

7.1.4.3 Visual Observations

Additional observations made on the 19/02/20 in the southern region of the Basin of Mexico and lacustrine deposits observed in the Northern region of the basement on 11/01/20.





Figure 29. Cobbled walkway and load bearing columns delineating the Zacapa Canal, Xochimilco.





Figure 30. Lacustrine deposits from an archaeological site in Tultepec, northern region of the Basin of Mexico.

7.1.4.4 Demographic Analysis

Municipality	Total Population	Population Density (/km ²)	State	Maximum distance from the nearest fault section (km)	Potential Warning Time (s) dependent on location within municipality
Álvaro Obregón	759,137	7,891	Mexico City	≤16.46	≤2.6
Azcapotzalco	432,205	12,863	Mexico City	≤26.95	≤4.3
Benito Juárez	434,153	16,200	Mexico City	≤10.10	≤1.6
Coyoacán	614,447	11,379	Mexico City	≤10.18	≤1.6
Cuajimalpa de Morelos	217,686	3,036	Mexico City	≤18.81	≤3.0
Cuauhtémoc	545,884	16,745	Mexico City	≤19.70	≤3.1
Gustavo A. Madero	1,173,351	13,303	Mexico City	≤31.60	≤5.0
Iztacalco	404,695	17,444	Mexico City	≤12.74	≤2.0
Iztapalapa	1,835,486	16,101	Mexico City	≤10.96 (Intersected)	≤1.7
La Magdalena Contreras	247,622	3,893	Mexico City	≤11.03	≤1.8
Miguel Hidalgo	414,470	8,913	Mexico City	≤22.92	≤3.6
Milpa Alta	152,685	511	Mexico City	≤27.13	≤4.3
Tláhuac	392,313	4,556	Mexico City	≤16.06	≤2.5
Tlalpan	699,928	2,215	Mexico City	≤17.67 (Intersected)	≤2.8
Venustiano Carranza	443,704	13,050	Mexico City	≤17.74	≤2.8
Xochimilco	442,178	3,879	Mexico City	≤12.13 (Intersected)	≤1.9

Table 22. Demographic analysis per municipality in Mexico City State. Population data from the latest INEGI (2020) census records. Colour scale represents the range in population density and total population. Maximum distance from fault (km) determined using Google Earth Pro. Potential warning time (s) calculated using seismic alert records for the 2017 Puebla/Morelos earthquake from SASMEX.

Municipality	Total Population	Population Density (/km ²)	State	Maximum distance from the nearest fault section (km)	Potential Warning Time (s) dependent on location within municipality
Acolman	171,507	1,967	Mexico	≤43.71	≤6.9
Atenco	75,489	859	Mexico	≤33.23	≤5.3
Atizapán de Zaragoza	490,000	5,263	Mexico	≤29.5	≤4.7
Chalco	400,057	1,770	Mexico	≤39.25	≤6.2
Chicoloapan	200,750	4,849	Mexico	≤28.51	≤4.5
Chimalhuacán	602,000	11,026	Mexico	≤11.35	≤1.8
Coacalco de Berriozábal	293,444	8,360	Mexico	≤38.88	≤6.2
Cuautitlán Izcalli	533,000	4,845	Mexico	≤33.27	≤5.3
Ecatepec de Morelos	1,806,226	11,505	Mexico	≤19.02	≤3.0
Huixquilucan	284,965	2,021	Mexico	≤26.99	≤4.3
Ixtapaluca	467,000	1,437	Mexico	≤10.55	≤1.7
Juchitepec	27,116	204	Mexico	≤37.86	≤6.0
La Paz	304,088	8,109	Mexico	≤17.59	≤2.8
Naucalpan de Juárez	833,000	5,272	Mexico	≤18.76	≤3.0
Nezahualcóyotl	1,100,000	17,323	Mexico	≤8.24	≤1.3
Nicolás Romero	430,601	1,848	Mexico	≤55.89	≤8.8
Tecámac	547,503	3,487	Mexico	≤55.16	≤8.7
Texcoco	277,562	645	Mexico	≤45.47	≤7.2
Tlalnepantla de Baz	664,000	7,954	Mexico	≤23.47	≤3.7
Tultitlán	516,341	7,649	Mexico	≤41.46	≤6.6
Valle de Chalco Solidaridad	391,731	8,388	Mexico	≤15.60	≤2.5

Table 23. Demographic analysis for Mexico State municipalities in the Basin of Mexico. Colour scale represents the range in population density and total population.